DTU Library

Developing High Performance Aluminium Alloy Tubes for Heat Exchange Applications

Zaffaroni, Giorgio Giovanni Battista

Publication date:
2020

Document Version
Publisher's PDF, also known as Version of record

DTU Mechanical Engineering
Department of Mechanical Engineering

Developing High Performance Aluminium Alloy Tubes for Heat Exchange Applications

Giorgio Giovanni Battista Zaffaroni

PhD Thesis

Ph.D. Thesis

DTU Mechanical Engineering
Department of Mechanical Engineering

Developing High Performance Aluminium Alloy Tubes for Heat Exchange Applications

A dissertation by
Giorgio Giovanni Battista Zaffaroni

Supervisors:
Prof. Rajan Ambat
Dr. Marco Pasqualon

Kgs. Lyngby 2020

DTU Mechanical Engineering
Department of Mechanical Engineering
Technical University of Denmark

Nils Koppels Allé
Building 404
2800 Kongens Lyngby, Denmark
Phone (+45) 45 25 19 60
http://www.mek.dtu.dk/

"I have never met a man so ignorant that I couldn't learn something from him."

-

Galileo Galilei

Developing High Performance Aluminium Alloy Tubes for Heat Exchange Applications

A dissertation by

Giorgio Giovanni Battista Zaffaroni

E-mail: giogbz@mek.dtu.dk
Technical University of Denmark
Department of Mechanical Engineering
Produktionstorvet
Building 425, room 125
DK-2800 Kgs. Lyngby

Academic Supervisor
Professor Rajan Ambat
E-mail: ram@mek.dtu.dk
Technical University of Denmark
Dept. of Mechanical Engineering
Produktionstorvet
Building 425, room 114
DK-2800 Kgs. Lyngby, Denmark

Industrial Supervisor
Doctor Marco Pasqualon
E-mail: Marco.Pasqualon@hydro.com
Hydro Aluminium
Innovation & Technology
Precision Tubing
Kortemarkstraat 52
BE-8810 Lichtervelde, Belgium

Published by: Department of Mechanical Engineering, Section for Materials and Surface Engineering, Produktionstorvet, Building 425, DK-2800 Kgs. Lyngby.

Preface

This dissertation is submitted in partial fulfilment of the requirements for obtaining the degree of Ph.D. at the Technical University of Denmark (DTU). The project was funded by Innovation Fund Denmark, grant number 5189-00144B and carried out at the Technical University of Denmark (DTU), Department of Mechanical Engineering, Section of Materials and Surface Engineering (MTU), in collaboration with Hydro Precision Tubing Tønder A/S, during the period from February 1st 2017 until April 30th 2020. Prof. Rajan Ambat, Technical University of Denmark, Department of Mechanical Engineering and Dr. Marco Pasqualon, Innovation & Technology - Precision Tubing, Hydro Aluminium, supervised the project.

Kgs. Lyngby, April 30, 2020

Abstract

This dissertation presents the research work aimed at developing high performance aluminium alloy tubes for heat exchange applications. The work, in particular, focused on the manufacturing technique development and optimization, together with characterization studies of produced prototypes. The research committed to the understanding of the close relationship occurring between final properties and manufacturing route, together with finished products' corrosion performances. The products, centre of this entire work, were high frequency welded aluminium tubes, comprising of different embossed inner grooved pattern designs and manufactured by using precursor bi-alloy strips, designed to provide both corrosion and heat transfer performances enhancement. Such technology is of particular interest for the application in round mechanically expanded tube-fin coupled heat exchangers. Key advantages are yielded by the employment of an all-aluminium exchanger solution. Performance improvements in terms of corrosion resistance and heat transfer, in both condensation and evaporation regimes, are given respectively by the novel material choice and advanced inner surface patterning. The industrial PhD project work thus comprised of process development work, including process parameter studies (involving i.e. on-the-field testing and finite elements simulations); tooling design, manufacturing and testing; design, manufacturing and installation of novel devices/inventions aimed at process stability and control improvement. In parallel, research work supported the previously mentioned activities for deeper understanding of product properties to process relationship, and structure-property correlation of materials. Therefore, two parts of this PhD project were:

- The development work carried out for achieving a stable manufacturing process, able to deliver desired finished tubes, within narrow window requirements in terms of final geometry, mechanical properties, inner contamination, corrosion performance;
- The research carried out on the structure-property correlation of produced tubes in terms of morphology, material flow behaviour, and microstructure to manufacturing technique and characterizing corrosion performance, in different environments and of tubes' both inner and outer surfaces.

The wide range of analysis and tests performed varied, for example light optical microscopy of samples treated with different preparation techniques (i.e. standard mechanical polishing, surface electropolishing, anodizing, etching) and with/without application of different light filters (i.e. lambda light filter), inspection modes (i.e. differential interference contrast). More advanced inspection techniques such as scanning electron microscopy (SEM) and transmission electron microscopy (TEM) were also employed. Focused ion beam (FIB) was a technique used for the preparation of both SEM and TEM samples. Elemental characterization of different samples was carried out by energy dispersive X-ray spectroscopy (EDS). Electron back scatter diffraction (EBSD) allowed grain structure analysis. Both acidified synthetic sea water testing (SWAAT) and customized special setups were used for corrosion testing of tubes, in different laboratory simulated environmental conditions. X-ray micro computed tomography was extensively used for three-dimensional, high resolution, non-destructive characterization of specimens. Additionally, detailed electrochemical measurements were performed (i.e. potentiodynamic anodic polarization, zero resistance ammetry) on different materials and in different electrolytes.
Overall, the project yielded major key innovations, both in terms of manufacturing technology upgrade and of process - materials - performances relationship understanding. Key achievements of the research and development work were:

- Definition of embossing tooling design and manufacturing guidelines, able to optimally handle and ensure best behaviour of materials along the process stages, delivering final optimal tube/pattern geometry and ensuring optimal welding;

- Increased understanding of the high frequency welding process dynamics and development of a new methodology (novel tooling), able to reduce inner contamination at no welding quality expense;
- Design, manufacturing and installation of engineering solutions able to critically increase and/or stabilize quality of products and manufacturing process;
- Increased understanding of materials behaviour, in terms of general morphology, mechanical modifications and microstructural transformations along different stages of the manufacturing route;
- In depth characterization of both outer and inner surface of tubes, in terms of corrosion behaviour, highlighting key issues and interesting practical implications, respectively for resistance of tubes in contact with highly alkaline substances, compared to standard neutral/acid environmental attacks, and for what regards corrosion behaviour of the embossed inner tube surface.

An overview of the development activities carried out in this industrial PhD project is provided in chapter 5. The core research work contained in this thesis is divided into 3 main chapters (6, 7 and 8) that present the scientific results of analysis on inner grooved high frequency welded aluminium tubes. Chapter 9 illustrates the outcome of the PhD, in terms of both scientific findings and correlated industrial development achievements.

Resumé

Denne afhandling præsenterer har som formål at udvikle højtydende aluminiumslegeringsrør til varmeudvekslingsapplikationer. Arbejdet fokuserede især på udvikling og optimering af fremstillingsteknikker sammen med karakteriseringsundersøgelser af producerede prototyper. Forståelsen af det nære forhold, der opstår mellem de endelige egenskaber og fremstillingsvej, sammen med færdige produkters korrosionspræstation er en af de mål af denne forskning. Produkterne, der er centrum for dette hele arbejde, var højfrekvente svejsede aluminiumsrør, omfattende forskellige prægede indre rillede mønsterkonstruktioner og fremstillet ved anvendelse af forløber bi-legeringsstrimler, designet til at give både korrosion og varmeoverførelsespræstation forbedring. En sådan teknologi er af særlig interesse til anvendelsen i runde mekanisk ekspanderede rør-fin-koblede varmevekslere. De vigtigste fordele opnås ved anvendelsen af en aluminiumsbytterløsning. Ydelsesforbedringer med hensyn til korrosionsbestandighed og varmeoverførsel, både i kondensations- og fordampningsregimer, gives henholdsvis ved det nye materialevalg og avanceret mønster inden for overflade. Det industrielle ph.d.-projektarbejde bestod således af procesudviklingsarbejde, herunder procesparameterundersøgelser (involverende dvs. on-the-field-test og finite element simuleringer); værktøjsdesign, fremstilling og testning; design, fremstilling og installation af nye enheder / opfindelser med fokus på processtabilitet og forbedring af kontrol. Parallelt med forskningsarbejde, der understøtter de tidligere nævnte aktiviteter til dybere forståelse af produktegenskaber til behandling og strukturering af egenskabskorrelation af materialer. Derfor var to dele af dette ph.d.-projekt:

- Udviklingsarbejdet, der udføres for at opnå en stabil fremstillings-

proces, der er i stand til at levere ønskede færdige rør inden for snævre vindueskrav med hensyn til endelig geometri, mekaniske egenskaber, indre forurening, korrosionsydelse;

- Forskningen udført på struktur-egenskabskorrelation af producerede rør med hensyn til morfologi, materialestrømningsadfærd og mikrostruktur til fremstillingsteknik og karakterisering af korrosionsydelse, i forskellige miljøer og af rør 'både indre og ydre overflader.

Det brede udvalg af analyser og test, der blev udført, varierede, for eksempel lysoptisk mikroskopi af prøver behandlet med forskellige forberedelsesteknikker (dvs. standard mekanisk polering, overfladevalgolvering, anodisering, ætsning) og med / uden anvendelse af forskellige lysfiltre (dvs. lambda-lysfilter) , inspektionstilstande (dvs. differentiel interferenskontrast). Mere avancerede inspektionsmetoder, såsom scanning elektronmikroskopi (SEM) og transmissionselektronmikroskopi (TEM) blev også anvendt. Fokuseret ionstråle (FIB) var en teknik, der blev anvendt til fremstilling af både SEM- og TEM-prøver. Elementær karakterisering af forskellige prøver blev udført ved energispredende røntgenspektroskopi (EDS). Elektron tilbage spredningsdiffraktion (EBSD) muliggjorde analyse af kornstruktur. Både havvandforsurede tests (SWAAT) og tilpassede specielle opsætninger blev anvendt til korrosionsafprøvning af rør i forskellige laboratoriesimulerede miljøforhold. Røntgenmikrokomputeret tomografi blev i vid udstrækning anvendt til tredimensionel, høj opløsning, ikke-destruktiv karakterisering af prøver. Derudover blev der udført detaljerede elektrokemiske målinger (dvs. potentiodynamisk anodisk polarisering, nulmodstandsammetri) på forskellige materialer og i forskellige elektrolytter.
Samlet set gav projektet store nøgleinnovationer, både med hensyn til opgradering af fremstillingsteknologi og forståelse af process-materialerydeevne. De vigtigste resultater af forsknings- og udviklingsarbejdet var:

- Definition af prægning af værktøjsdesign og produktionsretningslinjer, der er i stand til optimalt at håndtere og sikre bedste opførsel af materialer langs processtadierne, levere endelig optimal rør / mønstergeometri og sikre optimal svejsning;

- Øget forståelse af højfrekvente svejseprocesdynamik og udvikling af en ny metode (ny værktøj), der er i stand til at reducere indre forurening uden omkostninger til svejsekvalitet;
- Design, fremstilling og installation af ingeniørløsninger, der er i stand til kritisk at øge og / eller stabilisere produktkvaliteten og fremstillingsprocessen;
- Øget forståelse af materialernes adfærd med hensyn til generel morfologi, mekaniske ændringer og mikrostrukturelle transformationer i forskellige faser af fremstillingsvejen;
- I dybdekarakterisering af både indre og ydre overflade af rør, hvad angår korrosionsopførsel, fremhæver nøgleproblemer og interessante praktiske implikationer, henholdsvis for modstand af rør i kontakt med stærkt alkaliske stoffer sammenlignet med almindelige neutrale / sure miljøangreb, og for hvad angår korrosionsopførsel af den prægede indre røroverflade.

En oversigt over udviklingsaktiviteterne, der gennemføres i dette industrielle ph.d.-projekt, findes i kapitel 5. Det centrale forskningsarbejde indeholdt i denne afhandling er opdelt i 3 hovedkapitler (6, 7 og 8), der præsenterer de videnskabelige resultater af analysen om indre riller højfrekvente svejste aluminiumsrør. Kapitel 9 illustrerer udfaldet af ph.d., både med hensyn til videnskabelige fund og korrelerede industrielle udviklingsresultater.

Acknowledgements

I would like to express my deepest thanks and gratitude to my supervisor Professor Rajan Ambat, for his precious guidance and help, not only in these last three years of PhD studies, but starting back from the days of my Master. Professor Ambat is exceptional not only as a Scientist, but also as a person. He has been a great mentor, always present to indicate the right direction, at the right moment, protecting his students form stress and constantly inspiring with brilliant inputs. I also like to acknowledge and thank Senior Scientist Dr.-Eng. Marco Pasqualon for his huge help and support throughout these last three years of Industrial PhD work. Dr. Pasqualon is not only a skilled Scientist, but also a very sensible Manager, always able to read and understand others' attitude and pro-actively create the conditions for them to express their maximum potential. Working with him I've been learning a lot, from the technical knowledge to the project management aspects, and I have just begun.

I also would like to thank Visweswara Chakravarthy Gudla for productive scientific discussion, great collaboration and true friendship. Thanks to all my colleagues of Material and Surface Engineering for assistance, specifically, Peter, Steffen, Marianne, Niklas, from DTU MEK, Carsten and Sina from DTU Physics and Zoltan from Center for Electron Nanoscopy (DTU CEN) are all acknowledged. A special thanks to Morten, Hélène, Riccardo, Simone, Abhijeet, Vadimas, Kamila, Shivangi, Feng, Oleg and Umberto for being both great colleagues and friends.
Many thanks also to Bård and rest of the Innovation & Technology

team at Hydro, for welcoming me warmly from the first moment, as part of an extraordinary group.
Within Hydro, I am sincerely grateful to a lot of people that supported both mine and the project's development in these years. For that, I would like to thank John, Andrej, Thierry, Kevin, Mark, Kjeld, David, Jeff and the entire team in Rockledge.

I want to thank my family for the constant presence and support. For their selfless love and encouragement that sustained me through my efforts and the though times.
Thanks to Marco and Mike, for being family.

Last but far from least, I want to thank my incredible girlfriend Beatrice, for fighting every single challenge (sometimes, unfortunately, I was the challenge) and enjoying all the achievements of these long years of distance by my side.
But now:

"There ain't no mountain high enough
Ain't no valley low enough
Ain't no river wide enough
To keep me from getting to you."

List of articles and dissemination

Appended papers (to be submitted to Scientific Journals)

1. Zaffaroni G.G.B., Mishin O.V., Ciucani U.M., Gundlach C., Nordlien J.H., Ambat R., Characterization of High Frequency Welded Aluminium Microfin Tube for Heat Exchangers.

2. Zaffaroni G.G.B., Gudla V.C., Lagana S., Gundlach C., Olsson B., Nordlien J.H., Ambat R., Corrosion of Herringbone Grooved Embossed Aluminium Strips for Heat Exchanger Tubes.

3. Zaffaroni G.G.B., Gudla V.C., Rizzo R., Nordlien J.H., Ambat R., Corrosion Behaviour of High Frequency Welded Aluminium Micro-fin Tubes for Heat Exchangers.

Other publications (not appended)

1. Zaffaroni G. G. B., Gudla V. C., Ud Din R., Ambat R., Characterization of blisters on powder coated aluminium AA5006 architectural profiles. Engineering Failure Analysis, 103 (2019) 347-360. https://doi.org/10.1016/j.engfailanal.2019.04.039

2. Microstructural and Corrosion Issues of Embossed and Welded Aluminium Heat Exchanger Tubes.
   Date: Sep 7, 2017
   Description: Proceedings of the European Congress of Corrosion 2017, Prague, Czech Republic

3. Microstructural and Corrosion Issues of High Frequency Welded Aluminium Tubes.
   Date: May 24, 2018;
   Description: Proceedings of The 17th Nordic Corrosion Congress, Kgs. Lyngby, Denmark

4. Inner Corrosion of Herringbone Inner Grooved Embossed Aluminium Tubes.
   Date: May 31, 2018;
   Description: Proceedings of The 8th Aluminium Surface Science Technology Symposium, Helsingør, Denmark

5. Microstructural and Corrosion Issues of High Frequency Welded Aluminium Tubes.
   Date: Sep 11, 2018;
   Description: Proceedings of European Congress of Corrosion 2018, Krakow, Poland

6. Corrosion Behaviour of Embossed Aluminium Surfaces in Inner Grooved tubes.
   Date: Sep 07, 2019;
   Description: Proceedings of European Congress of Corrosion 2019, Seville, Spain

List of abbreviations and symbols

λ	Flowing charge
AC	Air Conditioning
B	Magnetic field
BSE	Back Scattered Electron
CRU	Commodity Research Unit
dl	Differential length
dq	Differential charge
dv	Differential volume
E	Electric field
$EBSD$	Electron Back Scattered Diffraction
EDS	Energy Dispersive x-ray Spectroscopy
$ESEM$	Environmental Scanning Electron Microscopy
F	Force
FDK	Feldkamp, Davis, Kress
FE	Finite Elements

FEG Field Emission Gun

FEM Finite Elements Modelling

FIB Focused Ion Beam

$HAADF$ High Angle Annular Dark Field

HAZ Heat Affected Zone

HF High Frequency

HFW High Frequency Welding

HTC Heat Transfer Coefficient

$HVAC\&R$ Heat Ventilation Air Conditioning and Refrigeration

HX Heat Exchanger

I Current

ID Inner Diameter

IG Inter Granular

IGC Inter Granular Corrosion

IPR Intellectual Property Rights

j Current density

L Length

LAB Low Angle Boundary

$LMIS$ Liquid Metal Ion Source

ND Normal Direction

OCP Open Circuit Potential

OD Outer Diameter

P Pressure

q Particle charge

RD Rolling Direction

$RTPF$ Round Tube Plate Fin

SE Secondary Electron

SEM Scanning Electron Microscopy

$STEM$ Scanning Transmission Electron Microscopy

$SWAAT$ Sea Water Acidified Test

T Thickness

TD Transverse Direction

TEM Transmission Electron Microscopy

v Speed

W Width

WE Working Electrode

ZRA Zero Resistance Ammetry

List of Figures

List of Tables

Contents

1 Introduction

Rare and expensive one century ago, aluminium has since been identified as the most common metal on earth, constituting about eight percent of the earth's crust (abundant, compared, for example, with the familiar iron at 5.06% [1]).Despite its raw availability, the reason why we are familiar with the bronze and iron ages while aluminium was so late in appearing on the scene, is connected to the real technical challenge constituted by the extraction of the pure metal from its ore Bauxite [1]. However, the introduction of the Hall-Héroult process in 1886 and the following technological advances sent the price of aluminium tumbling from 18 $ to 4.50 $ per kg, the first step in a downward course which has today stablished the selling price below two dollars per kg [2].
In 2020, the production of primary aluminium remains highly energy intensive. Roughly 12 -14 kWh are required to produce one kg of pure aluminium using the electrolytic reduction process [3]. On the other hand, a major driver for aluminium application is recyclability. In fact, aluminium is one of the most environment-friendly metals in use today, which is why it is often referred to as the "green metal". One of the major advantages of aluminium is that it is infinitely recyclable: 75% of the aluminium which has ever been produced is still in use. A significant benefit of recycling aluminium is that it requires only 5% of the energy used to produce primary aluminium, together with only about 4% as much CO_2, therefore significantly reducing environmental impact [4]. Additionally, an all-aluminium solution yields dramatic simplification of the handling of materials and separation process connected to recycling industrial practices, thus giving major costs reduction.

Due to its favourable strength to weight ratio, ease of formability, economical recyclability, inherent passivating and corrosion resistant nature, along with the ability to be surface engineered and treated to suit various functional application needs, aluminium alloys are today widely used in aerospace, automotive, construction, consumer electronics, marine, and food packaging industries [5][6][7][8]. Aluminium ranks number two in the consumption volumes among all the metals, surpassed only by steel. Recent developments in the motor industry, the rapid growth of cities, new potential uses of aluminium as a substitute to copper in the power industry – these and many other trends mean that this metal is well placed to strengthen its dominant position as a key structural material of the 21st century [4]. Nowadays, the high rates of aluminium consumption in terms of kilogram per capita are regarded by economists as one of the clear indicators of a robust and well-developed economy [4].
One of the industrial fields where aluminium consumption is rapidly increasing and expected to dominate in the future is the Heat Ventilation Air Conditioning and Refrigeration (HVAC&R) market. The HVAC&R systems market per se is a rapidly increasing business sector, due to the recent climate changes, pushing for increased energy efficiency together with the increased demand for cooling systems in the summer and heating in the winter. Such heating and cooling applications today incur a significant cost, together with contributing to the overall global warming, as most buildings directly use fossil fuels (heating oil, natural gas, and coal) for obtaining space heating and ozone-depleting refrigerant fluids in cooling systems. Therefore, the need for energy-efficient devices has led to the adoption of HVAC&R systems [9]. In particular, the market for heat pumps is growing, owing to their evolving capabilities such as performing both space cooling and heating functions along with the ability to heat water, and is expected to hold the largest share of HVAC&R system market [9].
Within the above-described scenario, Norsk Hydro decided to intercept the market needs investing into the development of new technologies for manufacturing of energy-efficient aluminium HVAC&R systems. The company is a world leading organization in the aluminium field, global provider of alumina, aluminium, aluminium finished products and solutions, leading businesses along the entire value chain (i.e. raw materials,

energy, primary metal, rolled products, extruded solutions and recycling). Central in this scenario is the manufacturing of mechanically assembled heat exchangers of the round tube plate fin (RTPF) design, typically consisting of extruded and sometimes drawn aluminium alloy tubes and fins stamped from rolled aluminium material.
Latest technological developments, driven by the above-mentioned requirements for increased efficiency, brought into the spotlight the usage of aluminium microfin tubes in these systems. A microfin tube is a round tube presenting inner surface enhancements (like the ones showed in fig. 1.1) able to nearly triplicate its heat transfer coefficient, in respect to standard smooth solutions [10][11][12].

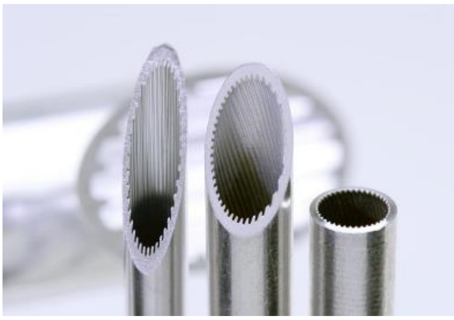

Figure 1.1: Example of aluminium microfin tubes.

Inner surface enhanced tubes can be produced by extrusion processes if the inner patterns are axial symmetric. However, such patterns do not provide the highest gains in heat transfer capabilities. More complex surface pattern geometries such as herringbone patterns can further enhance the heat transfer properties. However, these require unconventional manufacturing processes other than extrusion to introduce the complex pattern to the interior surface of the tube [13]. Therefore, these products are manufactured by aluminium strip embossing, for obtaining surface pattern enhancement, followed by stages of tube forming and high frequency welding to provide the final inner surface embossed heat exchanger tubes [13][14]. Figure 1.2 schematically illustrates the mentioned sequence of manufacturing stages.

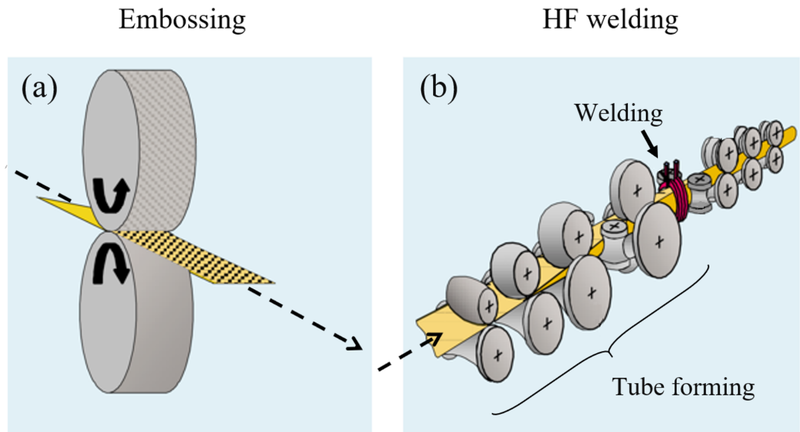

Figure 1.2: Schematic representation of manufacturing sequence for inner grooved welded tubes production, comprising of (a) embossing and (b) high frequency welding manufacturing stages.

The focus of this industrial PhD was to develop the mentioned manufacturing process, for production of inner grooved aluminium tubes, together with studying the corrosion performances and material modifications on finished products, yielded by the application of the introduced novel techniques.
Present project faced and solved all the manufacturing challenges historically stopping this technology from taking root, together with testing and studying process-related microstructural issues, materials behaviour and corrosion performances of finished products, in different environments and scenarios, resembling those of forecasted operative life. This work, resulted in a synthesis of process/product development and research, closely intertwined and providing both the introduction of novel engineering solutions and a deeper understanding of the process – materials – performances relationships.

1.1 Project organization

This PhD project "Developing High Performance Aluminium Alloy Tubes for Heat Exchange Applications" is part of the "Industrial PhD programme" under Innovation Fund Denmark (grant number: 5189-00144B)

and conducted in collaboration between Technical University of Denmark and Hydro Aluminium, Denmark. As an industrial PhD programme, research facilities and expertise at Hydro Aluminium and Technical University of Denmark were available for this project.

1.2 Outline of the dissertation

The dissertation is structured in 10 individual chapters. Figure 3 shows the bird view diagram of the thesis and their logical connection. Overall, work presented in the PhD thesis can be divided into three parts: (i) background information on the materials, technology, and technical target of the project (ii) the development activities related to embossing and high frequency welding process, supported and intertwined with the research work, and (iii) research activities connected to the detailed characterization of embossed and welded tube materials in terms of microstructure and corrosion issues. The core research-related part of the thesis (Chapters 6, 7, and 8) is presented in the form of manuscripts intended for publication in scientific journals.

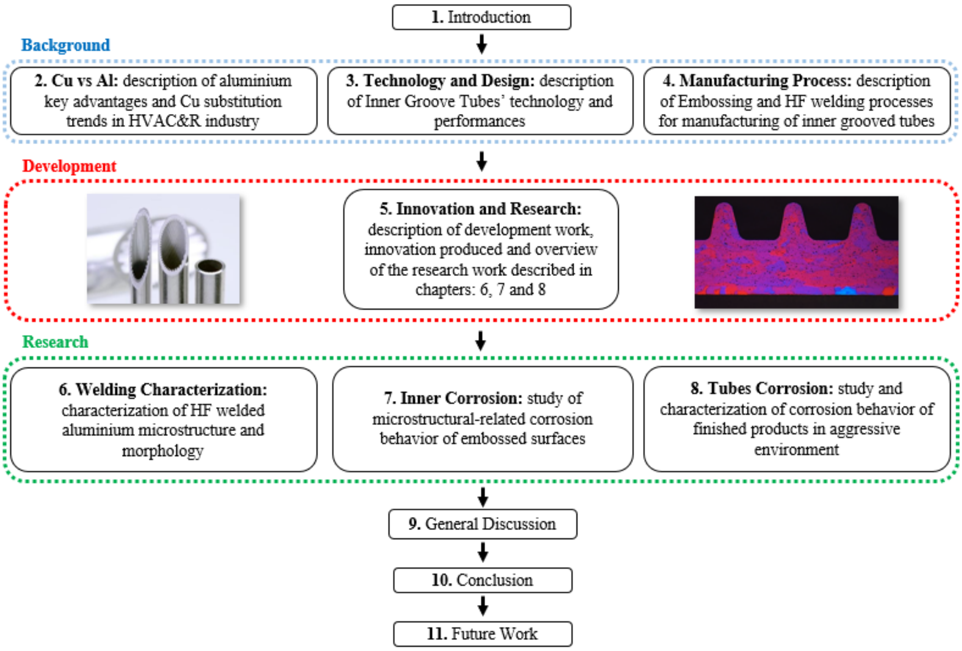

Figure 1.3: Process-chart of the dissertation.

Chapter 1 introduces the project and provides a formulation of the overall research objective. Chapter 2 reviews the key advantages connected to aluminium usage in heat exchange applications, with focus on the advantages with respect to common copper usage and the Cu substitution trends in todays market. Chapter 3 provides a review of the pre-existing knowledge on heat transfer performances of inner enhanced tubes for heat exchange applications. In addition, provides background information on the target products design and materials, base for the entire research and development work carried out in the project. Chapter 4 describes the manufacturing stages involved in the production of inner grooved welded aluminium tubes, with focus on the key principles of embossing and High Frequency welding. Chapter 5 illustrates the development and the research activities of the project. The chapter provides a high-level description of the development work, focused on the tubes' prototypes manufacturing and production process optimization. The entire manufacturing process and technological upgrades developed in this project are introduced. Because of confidentiality requirements

and ongoing Intellectual Property Rights (IPR) procedures, a consistent part of the PhD project work consisting of inventions, novel manufacturing techniques developed and the directly connected research results could not be included in the thesis. In chapter 5 a description of the overall structure and rational behind the research work described in following chapters is given.
Chapters 6, 7 and 8 present the research work carried out on the previously mentioned prototypes. These three chapters present the research contribution from the project. Chapter 9 provides an overall discussion including description of the industrial relevance of the work. Chapter 10 lists the major conclusions and chapter 11 suggestions for future work.

2 Aluminium vs. Copper

Aluminium is nowadays extensively used in the manufacturing of heat exchangers and gradually substituting other traditionally employed metals, such as copper. In particular, tubes are gradually reducing their still considerable percentage of copper usage. The development is converging to the manufacturing of all-aluminium heat exchangers (HXs) [5][6][7][8], driven by:

- Outstanding strength-to-weight ratio yielding dramatic gain in terms of total weight of products;
- Excellent corrosion resistance and improved galvanic balance of finished all-aluminium systems (no galvanic corrosion issues);
- More cost-effective products and better recyclability.

Aluminium tubes are 35% lighter than copper (weight per meter), for equivalent burst pressure values. This is a big achievement, both in terms of easier handling, lower shipping costs and better performances, in the case for example of automotive applications. However, it needs to be considered that, in the case of same burst pressure and lower weight, a bigger volume will be required in the case of aluminium. This increased volume implies more material necessary per ideal tube length, together with a higher tube wall thickness, influencing the heat transfer performances. However, thanks to the lower price of material and the heat transfer dynamics of the heat exchanger, aluminium still proves to be a winning choice.

Even if aluminium has half the thermal conductivity of copper, compared to the overall thermal resistance of a heat exchanger the portion

connected to the tube material itself has a negligible influence. For reference, implementing an Al fin-Al tube solution would mean a loss of only 0.23% in heat transfer coefficient of the heat exchanger, in respect to a solution with copper tubes. This negligible loss comes together with major advantages, first of which is the mentioned dramatic weight reduction.
Table 2.1 compares the physical properties of both aluminium and copper:

Table 2.1: Al and Cu physical properties.

Physical properties	**Aluminium**	**Copper**
Density (20 °C)	2.73 g/cm^3	8.96 g/cm^3
Modulus of elasticity (20 °C)	67000 N/mm^2	110000 N/mm^2
Thermal expansion coefficient (0-100 °C)	$23.2 \cdot 10^{-6} K^{-1}$	$16.5 \cdot 10^{-6} K^{-1}$
Thermal conductivity (20 °C)	200 W/mK	401 W/mK
Specific Thermal capacity (20 °C)	893 J/kgK	38 J/kgK
Electrical conductiity (20 °C)	23 to 29 m/Ωmm^2	60 m/Ωmm^2
Electrical specific resistance (20 °C)	0.042 Ωmm^2/m	0.0168 Ωmm^2/m
Melting temperature range	643 to 654 °C	1085 °C

If we consider the HX's tube-fin configuration and model it, focusing on the thermodynamics of the operative heat exchanging device, as is presented below (see fig. 2.1), it is possible to estimate the differences and relative impact of a shift from copper to aluminium, on the overall heat transfer resistance of the system.

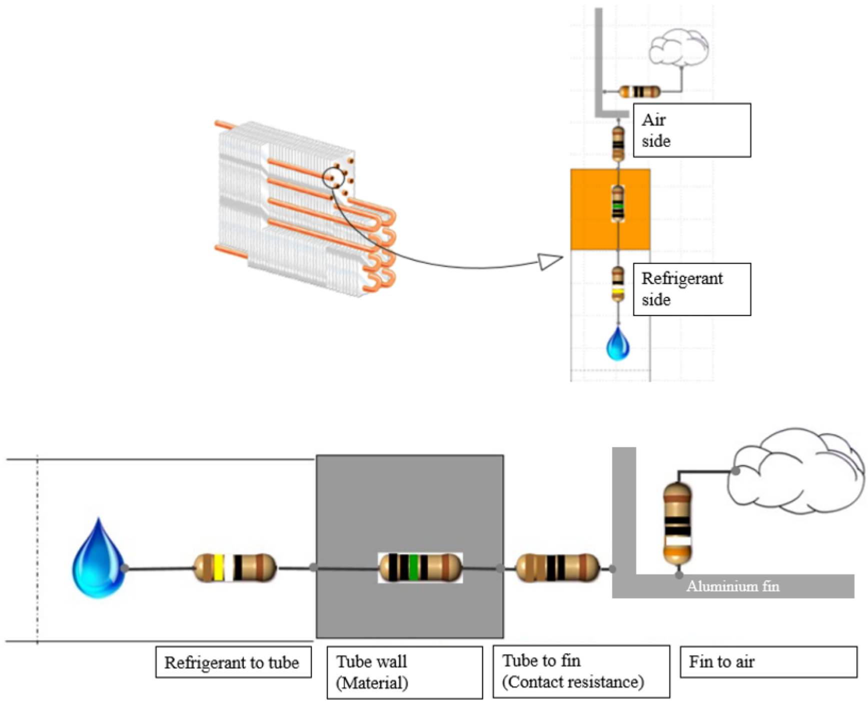

Figure 2.1: Thermodynamic modelling of the heat exchanging system's main components.

The overall heat transfer resistance of the system can be split into four main elements:

- Refrigerant to tube heat transfer resistance;
- Through the wall transfer resistance;
- From tube to fin transfer resistance;
- From fin to air transfer resistance.

These elements involve different exchange phenomena and dynamics, whose description is out of the scope of this thesis. However, it is possible to provide indicative values to compare the heat transfer resistance of the Cu-Al and Al-Al cases. Comparison is summarized in the following schematic representation (fig. 2.2).

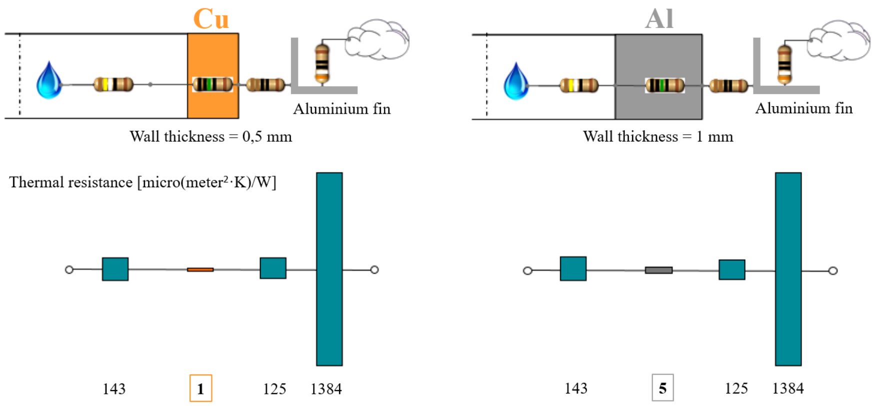

Figure 2.2: Comparison of values of thermal resistance for Cu-Al and Al-Al solutions.

It should be noticed that, together with the clear material difference, hence different physical properties, for the case of aluminium a thicker tube wall was considered for calculations. This was done because of tubes' minimum burst pressure requirements, implying, in the case of an operative aluminium tube, a necessary thicker wall in order to withstand same pressure-generated loads of the copper case. However, the above displayed numbers indicate that the fin-to-air heat transfer resistance is the one that, above all, more markedly influence the effective performance of the device (five times higher than the sum of all others contributes). For this reason, shifting from copper to aluminium, even if aluminium would require thicker tube walls, and even if aluminium is characterized by half the thermal conductivity of copper, would imply a definitely negligible loss in terms of total heat transfer efficiency.
Moreover, while aluminium remarkably outperforms copper in terms of corrosion resistance, thanks to its well-known passivating properties [5], major issues and cause for premature on-the-field failures nowadays are connected to their coupling. In fact, having coupled copper and aluminium, exposed to corrosive environments, is usually cause for premature and dramatic corrosion attack [5][6]. Thus, an all-aluminium solution guarantees not only superior corrosion resistance given by the better material properties per se, but also eliminates design-connected corrosion issues constituting a major concern in today's products.

Below, figure 2.3 shows evident differences in corrosion resistance occurring between a copper tube - aluminium fin heat exchanger and an all-aluminium one, after 500 hours of salt spray testing.

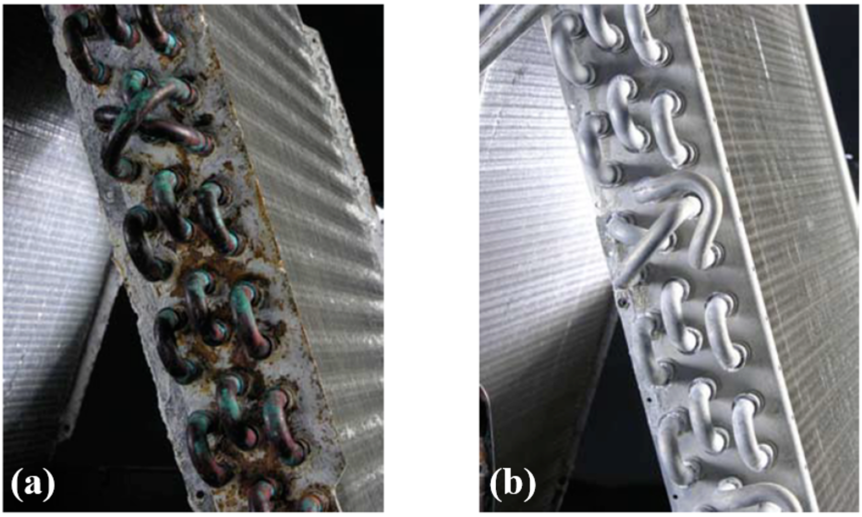

Figure 2.3: Cu tubes (a) vs. Al tubes (b), after 500 hours of salt spray testing.

For all-aluminium heat exchangers outdoor units, dedicated special zinc coatings of the tubes, providing extra protection against possible corrosion attacks from aggressive environments, are an available solution.

Another key aspect boosting the copper substitution by aluminium appears evident when comparing their price oscillations over the last 20 years. At the beginning of this century, prices for copper and aluminium were relatively similar and each metal had a dominant area of application: copper could be found in cables and wires (now approximately 60%) and aluminium in construction and transport (51%). However, in 2005, aluminium started to replace copper more intensively, and by 2007, price differences between the two metals became significant: rising from 1.2 in 2002 to 3.5 by end of 2007. For the period between 2005 and 2009, the total amount of copper substituted reached 1.86 million tons. It seems that the price differential (Cu vs. Al) triggered the mass substitution of copper with aluminium. In 2007,

the copper price averaged 7,126 US \$/ton, compared to the average price of aluminium, at 2,639 US \$/ton. The prices continued to grow from 2010 onwards, reaching a 4.5 copper vs. aluminium price ratio in 2014. According to estimates by the International Copper Association and Deutsche Bank, between 2004 and 2011, approximately 3 million tons of annual copper demand shifted to substitutes, including plastics, fibre optic and aluminium. In early 2015, when the price differential was still near record highs, London based CRU estimated that copper was losing about 2% demand a year, or approximately 500,000 tons. About half of this loss is due to substitution for aluminium, with the light metal gaining ground in thermal conductivity applications [15].
Finally, aluminium recycling is important for resource preservation. There is no need to separate different materials in an all-aluminium heat exchanger, thus making recycling both much easier and achieving consistent gain in terms of carbon footprint reduction.

3 Technology and Design

Since the 1970s, global requirements for energy efficiency in air conditioning systems becoming more stringent and raw material costs have driven to a continuous research for more efficient heat transfer systems. This has led to the development of many types of inner grooved tubes along the years, optimizing performances, reducing unit footprint and costs related to raw materials [11].

3.1 Product and process evolution

Historically speaking, inner-grooved tubes design has evolved, since the latter half of the 1970s, following development stages similar to those experienced by the fins: evolving from plain to wavy, louver and finally convex-louver fins [11]. For the tubes, this has meant a transition from original employment of smooth tubes, to the first inner surface enhanced tubes, presenting grooves consisting of a large fin apex angle of 90 degrees, parallel in respect to the axial direction of the tube. Later, between 1980s and 1990s, designs evolved to helical patterns, with helix angles ranging from 18 to 35 degrees and apex angles of 53 down to 15 degrees. These grooves were produced thanks to a grooved mandrel inserted inside the tube and connected by a tie rod to a floating plug. The floating plug was fixed by a drawing die, reducing the diameter of the tube, whose inner surface was then grooved by the rotating mandrel. The tube was then reduced to final diameter by a finishing die (figure 3.1) [11].

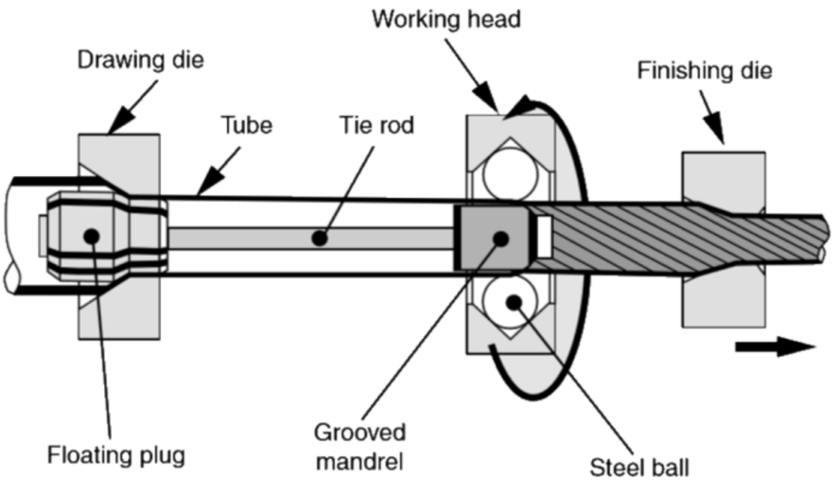

Figure 3.1: Traditional method for production of an inner grooved helical tube [11].

In 2000s, energy saving laws and issues with Freon regulations introduced to the market refrigerant fluids characterized by reduced heat transfer coefficients (HTC). This has pushed for further research and designs optimization, introducing cross grooved tubes, fine structure secondary grooved tubes and herringbone tubes (figure 3.2) [11].

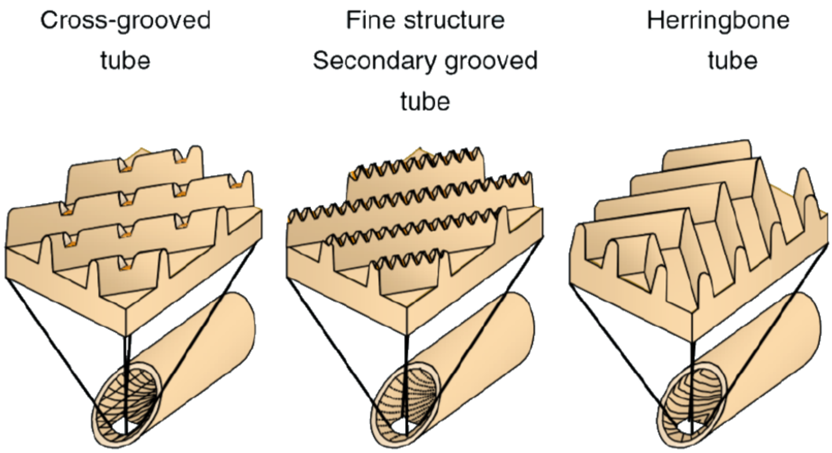

Figure 3.2: Inner-grooved tubes, pattern design examples for enhanced heat transfer performances [11].

Tubes with fine structure secondary grooves and those with herringbone grooves need to be welded tubes. In fact, non-axial symmetric pattern designs cannot be obtained with the above-mentioned classic manufacturing techniques (involving use of a drawing die combined with a rotating mandrel). The process for production of these special internal-enhanced welded tubes is divided into 2 main stages: 1) Embossing and 2) Tube high frequency (HF) welding [13][16][17]:

1. Embossing stage: consists in thread cold rolling of a strip, on the surface later corresponding to the inside of the finished tube [14].

2. HF welding of the as-embossed strip: the tube is obtained by longitudinally forming the as-embossed flat strip into a tube geometry and then welding the two strip edges together. To achieve this, the strip is fed into a forming mill that shapes the strip by different consecutive forming steps performed by several forming rolls. As the strip approaches the end of the forming line, it passes through an induction coil, which induces electrical current, mostly concentrated at the strip edges to be joined. The edges are resistance-heated to high temperature, reaching the melting point. The superficially-molten edges are forged together by side

squeeze rolls. When passing through the weld rolls, the oxidized and molten material are extruded out of the joint and the clean underlying material is bonded [13].

The process, in all the stages, will be presented in detail in following chapters of the thesis, with direct reference to the exact process involved in the sample production for the present experimental research and development work.

3.2 Performances enhancement

Microfin tubes (inner surface enhanced tubes), in general, have outstanding performance in enhancing heat transfer for both evaporation and condensation, without introducing excessive penalization in the pressure drop [18]. The two most diffused types of patterns, on which today HVAC&R industry is focusing, are the more classic helical microfin tubes and the herringbone ones. Condensation and evaporation heat transfer characteristics in helical tubes have been elucidated in various studies [19][20][21]. Evaporation and condensation heat transfer characteristics of herringbone tubes were also experimentally studied [22][23][24][25][26][27][28]. In Herringbone tubes, additionally, fin-diverging and fin-converging parts, can be arranged differently at different orientations. Structure orientations affect liquid film distribution and thus the heat transfer coefficients, as described in Refs. [24][25][26] [29]. Literature results highlight major advantages in terms of HTC increase, in respect to smooth tubes, of both pattern designs, due to different flow regime characteristics given by the specific type of surface enhancements.

Concerning helical tubes, Colombo et al. studied the heat transfer coefficient and pressure drop showing that this type of microfin tubes (HVA and VA in figure 3.3, which differ essentially in the fin number) are characterized by larger heat transfer coefficient and pressure drop than the smooth tubes, but their behavior differs whether they are used for evaporation or condensation. During evaporation, at low mass fluxes, microfin tubes are particularly effective in increasing heat transfer. Moreover, in the finned configuration, the dry-out takes place at larger qualities than in the smooth tube. The performance of the microfin tubes is similar and it does not seem dependent on the fin number. On the contrary, during condensation, the tube with the largest number of fins shows worse performance [18]. Figure 3.3 shows heat transfer coefficient measurements, represented as function of mass flux, of smooth and enhanced helical microfin tubes, from the work of Colombo et al.

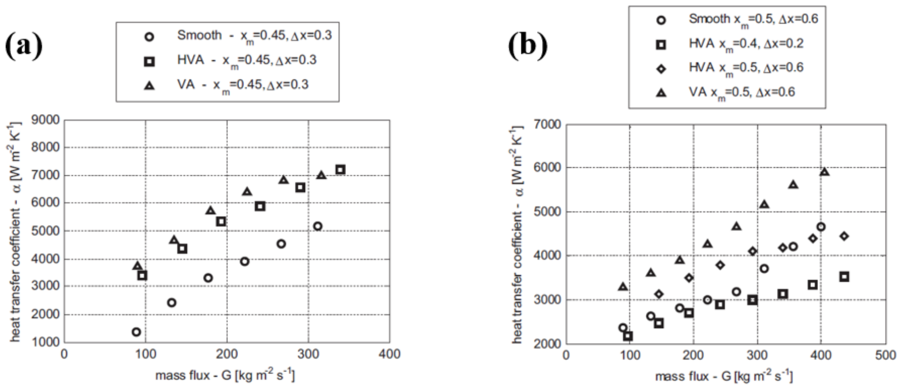

Figure 3.3: Heat transfer coefficient measurements, represented as function of mass flux, of smooth and enhanced helical microfin tubes [18].

From a qualitative point of view, the herringbone microfins if properly arranged, compared to smooth tubes, can extend the annular flow pattern to relatively low vapour qualities and mass fluxes. This is because the herringbone microfins redistribute the liquid layer around the circumference of the tube due to centrifugal forces and surface tension [30].

Figure 3.4, from the work of Guo et al., presents the relationship between the condensation heat transfer coefficient and mass flux for smooth, herringbone and EHT (hybrid surface with a surface area increase and flow separation produced by primary dimple/protrusion enhancement) tubes using refrigerant R410A. The herringbone tube presents the highest heat transfer coefficient under condensation, while the smooth tube produces the lowest heat transfer coefficient for all tested mass fluxes. The heat transfer coefficient of the herringbone tube is around 2– 3 times that of the smooth tube for condensation.

Since the heat transfer enhancement ratio (2–3) is larger than the inner surface heat-transfer area ratio (1.57), heat transfer enhancement from mechanisms other than surface area increase must come into play [30].

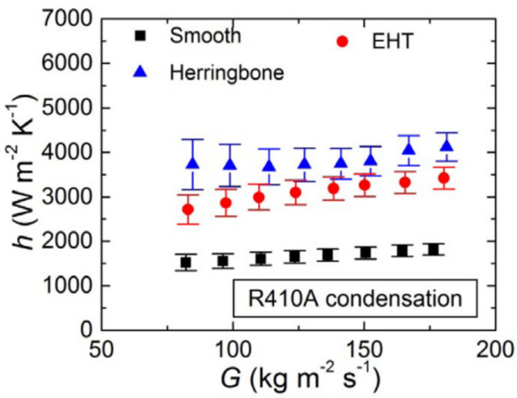

Figure 3.4: Comparison of the condensation results for smooth, herringbone and enhanced surface EHT tubes for the following conditions: saturated temperature, inlet vapor quality and outlet vapor quality are 47.0 ± 0.5 °C, 0.80 ± 0.01, 0.20 ± 0.01 [30].

The diverging fins at the bottom push the liquid up to the top (i.e., redistribute the liquid film more evenly), thus enhancing the heat transfer. In addition, the liquid converging at the top induce liquid mixing and turbulence, and this plays an important role in the heat transfer enhancement. The centrifugal force produced by the herringbone microfins spreads the liquid to the upper portion of the tube, and surface tension pulls the condensate from the fin tips into the drainage channel at the base of the fins, forming a very thin liquid layer on the surface of the microfins that greatly enhances the heat transfer [30].
Work of Guo et al. also demonstrated how different refrigerants would yield different heat transfer coefficient values and change their trend in respect to mass flux variations (different fluid viscosity), however, that will not change the ranking of tube performance [30].
In evaporation, despite a large increase in the inner surface area, the herringbone tube does not present an obvious heat transfer enhancement. As in figure 3.5, the evaporation heat transfer coefficient of the herringbone tube is only slightly larger than that of the smooth tube. Heat

transfer enhancement ratios in the herringbone tube are far less than the surface area ratio (1.57) for all mass fluxes. That means that not all the inner surface area contributes in heat transfer enhancement [30]. Part of the fin surface is exposed to the vapour, and therefore is inefficient for heat transfer. Liquid film dry-out might occur for evaporation (this is especially true at high vapour qualities), since the saturation temperature is much lower than that for condensation and the vapour density is much lower. The strong vapour shear due to the low vapour density in evaporation may entrain liquid droplets. Droplets may also be entrained into the vapour due to the strong interfacial turbulence induced by the herringbone microfins [30]. In addition, the large latent heat of vaporization and the large vapour density tend to form thin liquid films. All these factors result in a low evaporative heat transfer enhancement for the herringbone tube [30].

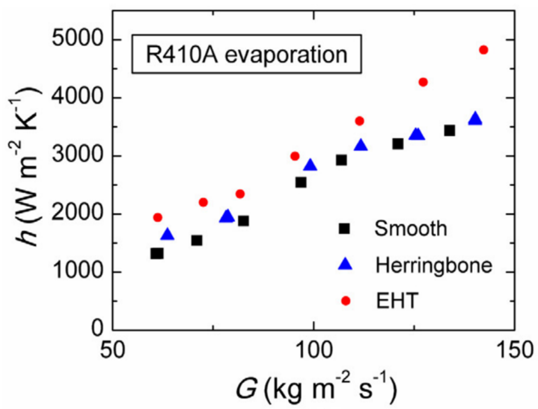

Figure 3.5: Comparison of the evaporation results for smooth, herringbone and enhanced surface EHT tubes for the following conditions: saturated temperature, inlet vapor quality and outlet vapor quality are 6.0 ± 0.2 °C, 0.10 ± 0.02, 0.90 ± 0.02 [30].

In line with the overview presented above, current trends see high demand for herringbone inner grooved tubes for condensation applications, i.e. installation in AC units, while helical inner grooved tubes are preferred for evaporation applications, i.e. for heat pumps.

3.3 Project target for products and performances

Many different pattern specifications exist today on the market, varying in fins number, fin height, fin apex angle, fin base width, fin-to-fin width, and helix angle. Additionally, demand differentiate in many alternative diameters and bottom wall thickness of the tubes. Optimization of the mentioned design parameters was however out of the scope of this work, as well as the study of heat transfer related phenomena, as the ones presented in this chapter in order to provide context reference.

Efforts of this project were aimed at development of both types of previously mentioned internally enhanced aluminium microfin tubes (helical and herringbone), with focus on the manufacturing process development and optimization, investigation of corrosion performance and process-related effects on material properties. The exact designs of both the herringbone and helical tubes developed in present project cannot be shared because of confidentiality requirements. However, additional information on development work carried out in this project is provided in chapter 5.

HF welded Al microfin tubes were manufactured using aluminium strips comprising of a main core 3xxx alloy, with one sided 10% clad of 7xxx alloy (corresponding to the outer surface of final tubes). The latter having at least 30 millivolts of corrosion potential difference in respect to core alloy, allowing a sacrificial corrosion protection function [31][32] (see figure 3.6 for schematic representation of materials functions and tables 1, 2 for chemical composition guidelines). Such material combination was chosen in line with recommendations and claims of United States Patent US 9,964,364 B2 [31].

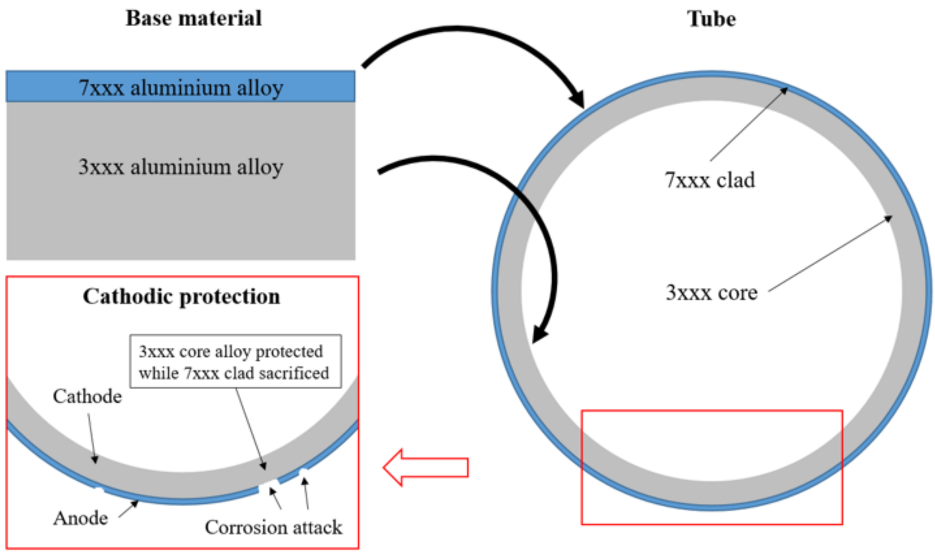

Figure 3.6: Schematic representation of materials combination in both strip and tube forms, with sacrificial protection function of the clad synthetically presented.

In particular, aluminium strips used in present experimental work were constituted of a 3xxx-series alloy core with a 7xxx-series alloy sacrificial clad, provided in 'O' temper condition, composition mentioned respectively in table 3.1 and 3.2. The strips were obtained with patterns embossed on the AA3xxx side, corresponding to the inner side of the tube once formed and welded. Manufacturing of the cladded strips involved the core and clad alloy being joined together through a hot rolling process, such that the two sheets are metallurgically bonded together, prior to strips' slitting to desired dimensions [34].

Table 3.1: Chemical composition (in wt. %) of AA3xxx aluminum alloy (core) selected for present work.

Mass %	Si	Fe	Cu	Mn	Mg	Zn	Ti	Others		Al
								Each	Total	
Min.	-	-	0,5	1,0	-	-	0,10	-	-	Rest
Max.	0,25	0,4	0,6	1,3	0,05	0,10	0,20	0,05	0,15	Rest

Table 3.2: Chemical composition (in wt. %) of AA7xxx aluminum alloy (clad) selected for present work.

Mass %	**Si + Fe**	**Cu**	**Mn**	**Mg**	**Zn**	**Ti**	**Others**		**Al**
							Each	Total	
Min.	-	-	.	-	0,8	-	-	-	Rest
Max.	0,7	0,10	0,10	0,10	1,3	-	0,05	0,15	Rest

The exact chemical composition of core and clad aluminium alloys is not provided because of confidentiality requirements.

4 Manufacturing Process

Production of Inner grooved aluminium tubes for heat exchange applications calls for optimal implementation of a complex two-stage process. The two-stage process involves: i) Embossing and ii) High frequency (HF) welding into the tube shape [13][16][17].
In particular, the strip is handled through two distinct lines, in the form of coils, hence provided as blank strip coil to the embosser, giving an embossed strip coil as output. The latter, afterwards, goes into a high frequency welding mill, providing final coiled inner grooved tubes. Figure 4.1 shows the overview of these processes.

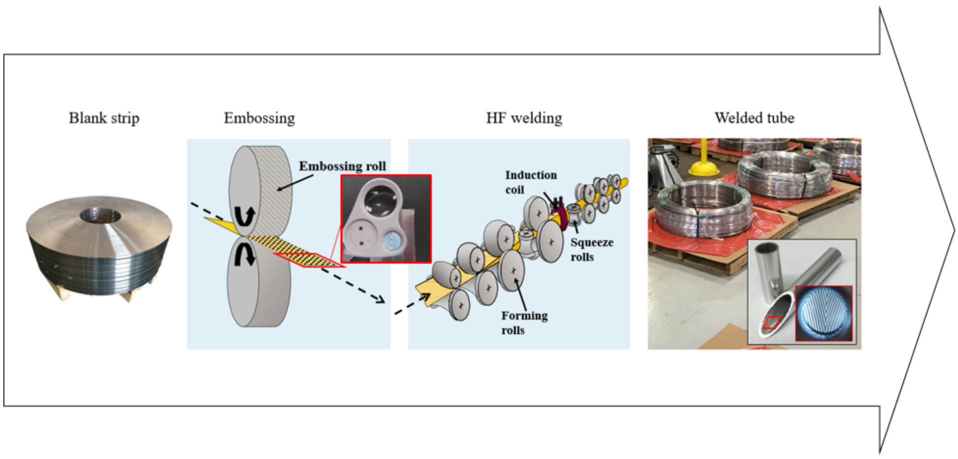

Figure 4.1: Manufacturing path overview: from blank strip to coiled welded tube.

4.1 Embossing

The embossing stage represents first key step in the production chain for obtaining the strip with pattern geometry, later appearing on the inner surface of finished tube. The embossing procedure consists of a cold deformation process performed on aluminium strips, for instance on their non-cladded side, with the aim of obtaining the characteristic and previously introduced surface patterns (Chapter 3). The surface pattern as described previously increase performance in both evaporation (Helical) and condensation applications (Herringbone).
The cold forming of the pattern involves applying the desired pattern onto the strip surface by a cold roll-forming process, where the blank strip is fed between rolls applying the needed forming pressure and rotating at constant even speeds. The upper embossing roll, presenting negative of the desired strip pattern, is pressed onto the strip, which is sustained by a lower anvil roll. The strip is de-coiled at controlled speed, fed into the central embossing station and afterwards automatically re-coiled thanks to a torque-controlled automatic system as shown in a schematic overview in figure 4.2.

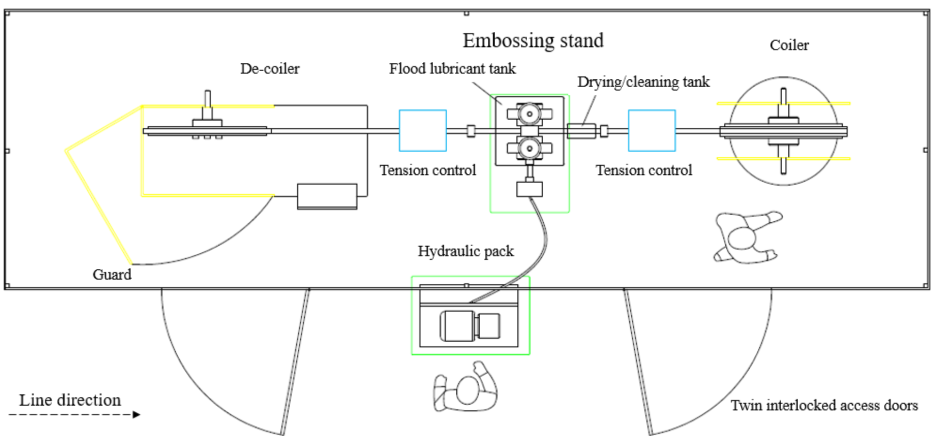

Figure 4.2: Embossing station: layout topographic representation.

Tension at both inlet and outlet sections of the embossing station (respectively between de-coiler and embossing station and embossing station and re-coiler) is controlled by idler rolls, mounted on swivelling arms, with pull rolls before and after, used to keep the tension within the strip, while the idler (so-called dancer) roll is pressing on it with defined power as shown in figure 4.3.

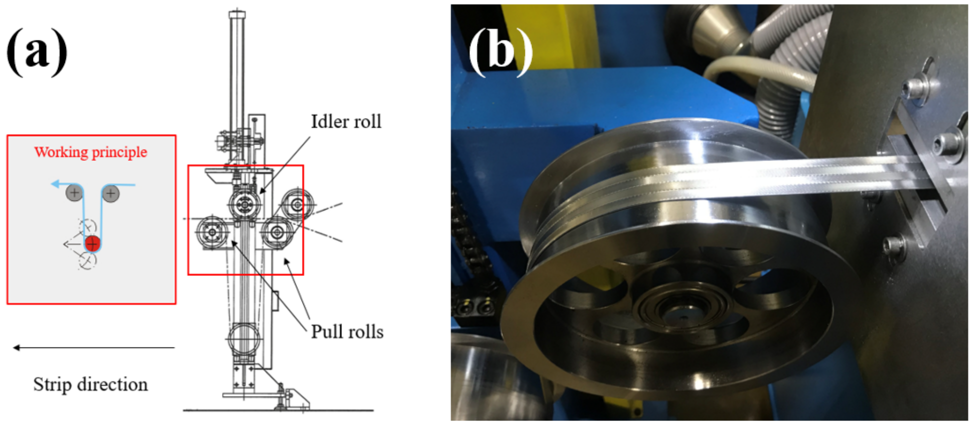

Figure 4.3: Tensioning system with dancer roll (a) and picture of herringbone embossed strip between embossing and post-embossing tensioner (b).

As a result, the embossing process takes place when strip passes, at controlled speed, trough the two forming rolls, with constant applied front and back tensions. The two rolls rotate at constant equal speeds. They have same outer diameters and are regulated in position thanks to screws that control vertical movement of two carriages hinged to the upper roll's rotating shaft extremities (see figure 4.4). Therefore, while the lower anvil roll is fixed in horizontal position, the upper embossing roll has the freedom to be adjusted in vertical direction, varying the gap between rolls, thus allowing to tailor and optimally distribute forming pressure on the strip.

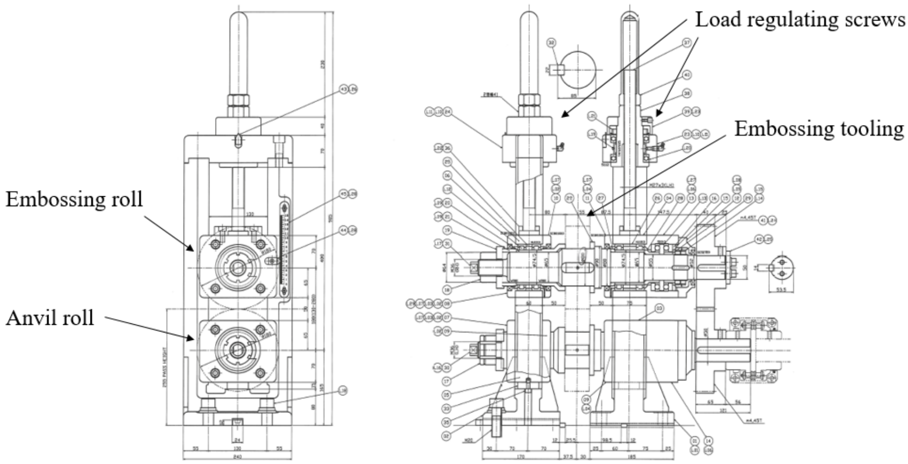

Figure 4.4: Technical representation of embossing mechanical system with main functional components highlighted.

A correct embossing process is that one giving as output a strip with correct bottom wall thickness, together with complete formation of the surface pattern. It is also important that the formed strip should not present any critical defects at the edges (possibly produced by uncontrolled lateral material displacement during cold deformation), no camber or undesired twisting behaviour. In the process, the material is not pressed in the plane orthogonal to the strip horizontal movement thus deforming just vertically and laterally, but instead undergoes a three-dimensional deformation with the strip being stretched during the process. Such stretching was found to be a key element of the embossing process, and results in an optimal balance between applied embossing load (position of upper embossing roll regulated down to appropriate level in respect to anvil roll surface), line speed and front/back tensions. The system was operated wet, having both upper and lower rolls flooded with a water-oil emulsion (Water-oil ratio of 4.0), for cooling and lubrication purposes.
The described process was object of several tests and engineering upgrades, throughout this project, first with the aim of better understanding the dynamics of the process and key control parameters, second to improve process control and outcome in terms of quality/consistency, and third to adjust the process in order to provide best final products.

4.2 High Frequency welding

Similar to many other non-ferrous metals, Aluminium can be successfully welded by High Frequency Welding (HFW) [13]. However, the process of HFW for aluminium is still very little understood. Main reason for this is to be addressed to the characteristic forgiveness of this process, which currently allows daily production of several tons of tubes, produced by manufacturers with very little knowledge on the principle behind the process and implications [33]. Although the tube HFW is commonly indicated as a forge welding process, it is difficult to find an appropriate definition for its outcome, in scientific terms, in technical literature. The term comes from a combination of procedures historically performed by metal workers, using a forge as main tool, heating metal parts up to temperatures close to their melting point and then hammering them together to generate a bond, therefore it is called a "forge weld". In other words, it is a hot diffusion bonding process [33]. A diffusion bond is the very highest quality metal to metal joint. Key parameters of this process are force (or pressure, as will be later explained), temperature and time. Typically, very high pressures are required while time required is dependent on the temperature reached [33]. Therefore, when we refer to high frequency tube welding, it implies extremely high pressures applied, for very short times and right at the melting point. At this temperatures, diffusion rates in the solid state are very high, allowing the development of high quality bonds in very short time. Confusion about the definition and relative nature of the process arises from the definition of welding, since, in order to weld, one metal has to melt. Indeed, in HF Welding, melting must occur. However, in theory, the melt is squeezed out of the joint, leaving no melted or cast metal behind. This phenomenon is connected to the very high forces to which the joint is exposed, while still at elevated temperatures [33] (it will be later explained exactly how).

4.2.1 HF linear welding of tubes

High frequency welding process can be effectively used for making tube from metal strips by linear welding process as shown in figure 4.5. Such tubes are manufactured by longitudinally forming flat metal strips into a nearly complete tube and then welding the two edges together. To achieve this result, the aluminium strip is fed into a forming mill that shapes the strip through different consecutive forming steps performed using a sequence of forming rolls.

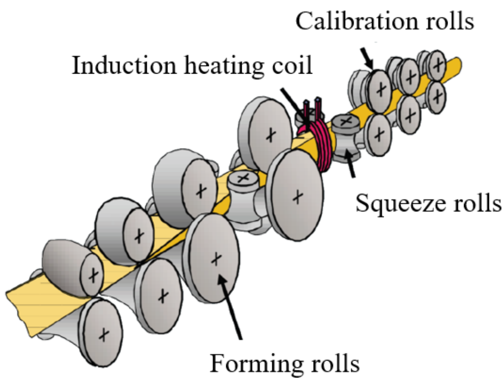

Figure 4.5: Schematic representation of high frequency welding of tubes with forming rolls showing formation of tube shape.

As the strip passes through the working coil (an induction heating coil), an induced current flows through the strip, mostly concentrated at the edges to be joined. The metals resistance to the electricity flow generates the necessary heat development at the edges, where the temperature can reach to the melting point. When the edges are still in molten state, they are forged together applying force on the strips thanks to the interaction with side squeeze rolls. When passing through the weld rolls, the oxidized molten metal is extruded out of the joint and the clean underlying metal is bonded [13]. Following this, the sizing rolls complete the process, giving desired final geometry to the tube. Figure 4.6 shows a schematic representation of the high frequency welding stages and an example of partially molten edges before the welding point (so called “vee”).

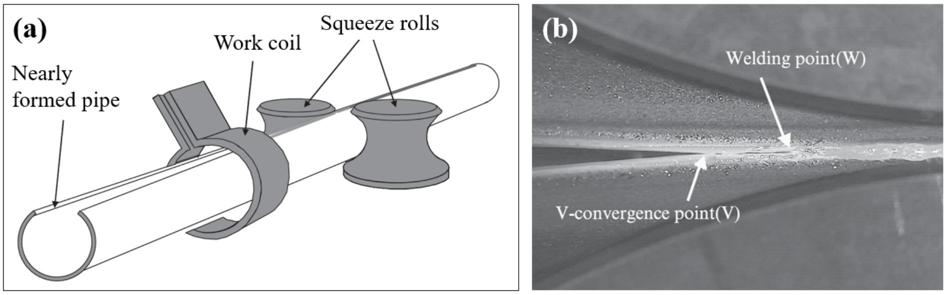

Figure 4.6: Schematic representation of high frequency welding setup (a) and picture of so-called ”vee” and welding point at weld rolls (b).

In relation to the HF current flow and the joining process itself, everything originates from current flowing in the work coil producing a magnetic field, which intersects with the nearly-formed open tube. In this scenario, employing high frequency alternating current allows the exploiting of two key physical phenomena, indicated as “skin effect” and “proximity effect”, typical of alternating current flowing through conductors and involving uneven distributions of current density [34]. First one, the “skin effect”, describes the tendency of current flow to be typically confined in a very shallow skin on a metal surface. The higher the frequency, the shallower the current skin penetration will be (hence, higher skin effect), as represented in figure 4.7.

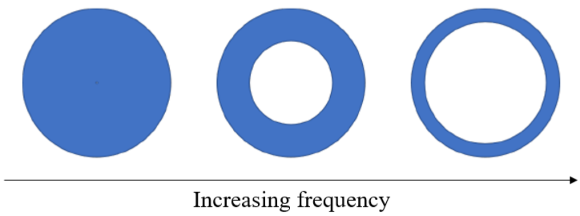

Figure 4.7: Schematic example of charges distribution on round conductor, with increasing induction alternated current frequency.

Second key phenomena is called ”proximity effect” and describes how two opposite high frequency induced currents, flowing near each other, will lead to current concentration on the adjacent edges of the conductor [13], as schematically represented in figure 4.8.

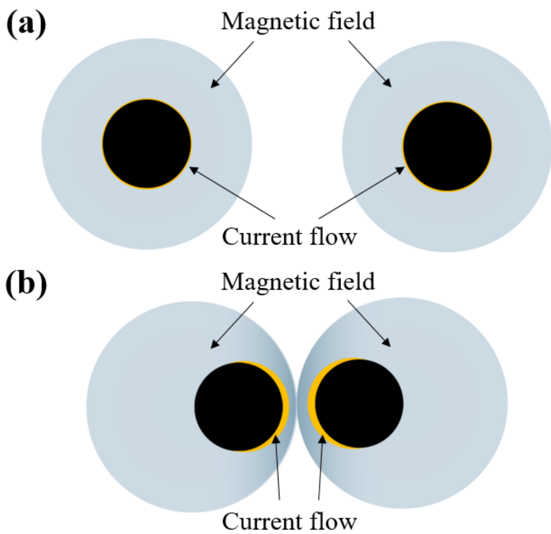

Figure 4.8: Schematic representation of proximity effect, example of round conductors in current-inducing magnetic fields: (a) distant conductors, (b) conductors approaching and influencing each other.

The combination of these two effects, in the specific case of tube welding, will lead to the confinement of most of the HF current in the shallow skin on the two inside edges of the ”vee” (formed by the nearly-tube-formed strip) resulting in heat generation. How the interaction of these two effects influences the distribution of heat into the strip is schematically represented in figure 4.9.

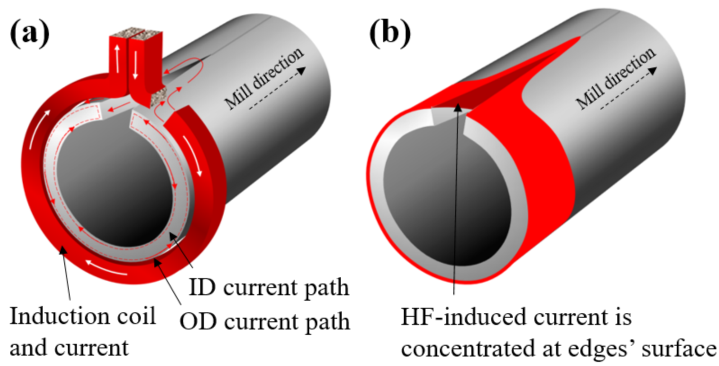

Figure 4.9: Representation of weld coil working principle (a) and HF-induced current distribution on strip edges at welding (b).

The proximity effect will be higher depending on the closeness of the two edges. This means that a narrower "vee" will result in higher heat production. The vee apex angle is therefore considered a crucial parameter, since, in general, to a narrower vee corresponds a more power efficient system. However, narrower vee also can lead to higher risk of developing weld defects [13]. It follows how edges' geometry and presentation are key parameters, influencing current density distribution, thus the heat generation [33][34][35][36]. Figure 4.10 shows a schematic example of the influence of different orientations on the current density distribution in adjacent conductors, which resembles to the situation of strip edges meeting each other at the welding stage.

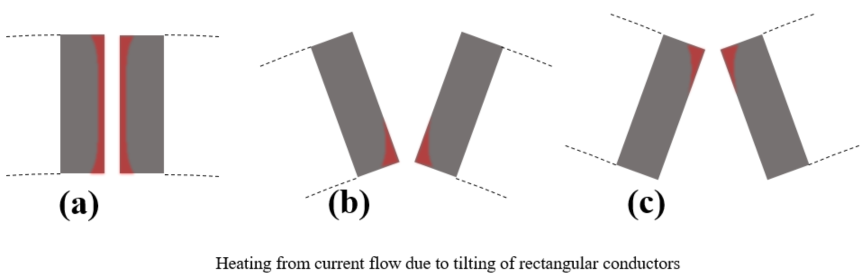

Figure 4.10: Schematic example of presentation/orientation influence on current flow at strip edges, in function of proximity and skin effect combined: example of parallel adjacent conductors (a) and tilted adjacent conductors (b) (c).

4.2.2 Spume

In the HF welding process, an extremely high density of current is induced on edge surfaces facing each other, in an opposite direction because of the skin effect and the proximity effect of a high frequency current [36]. It is well known that currents flowing in opposite directions repulse each other. The repulsive force (Lorentz force) acts as pressure ("P" in figure 4.11) on the edges' surface, high enough to remove molten metal immediately upon formation form the edge surface. This situation is schematically shown in figure 4.11 [36]. Displacement of the molten metal due to this effect and the applied forging pressure is a critical issue, which directly influence the finished product quality in terms of: (i) Inner weld bead height and (ii) tubes' inner contamination level.

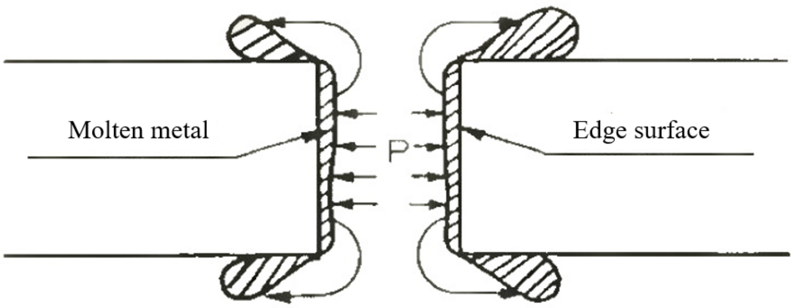

Figure 4.11: Schematic illustrating the removal of molten metal formed on the edge surfaces by electromagnetic pressure (P) [36].

In fact, upon joining, part of the molten material that is extruded out of the weld will re-solidify and form both outer and inner weld beads ("inner" and "outer" defined in respect to welded tube's geometry). While outer weld bead formation does not create any critical problem (which is removed normally by in-line scarfing process of the outer surface), same cannot be done on the inner tube surface. Small diameter tubes such as the ≈ 7 mm OD tubes developed in this work has insufficient inner diameter for scarfing tools. Therefore, it is important to reduce/avoid inner bead formation using innovative methods, which were developed as part of this project. In this project, techniques have

been developed in order to take care of this critical aspect (chapter 5). Reduction of contamination inside the tube is an even tougher technical challenge involving understanding and tailoring of complex process dynamics.
Examining what exactly occurs at the so-called “vee”, it can be helpful highlighting three consecutive process periods:

1. From the edges, liquid metal starts to generate and build up in the vee, where the current density, hence heat, is higher;

2. The molten metal from the two edges meets and forms a pool, covering portion of the vee;

3. When the surface tension of the liquid cannot sustain the melt meniscus volume anymore, this breaks and is ejected out of the vee, both to the outside and the inside of the tube, generating contamination (so called “spume”).

There are two forces playing a critical role in the above-described sequence of events, which are Laplace forces and capillarity forces. Laplace force derives from Lorentz force, which in electromagnetism is the force exerted on a charged particle q moving with velocity v through an electric E and magnetic field B [37]. The entire electromagnetic force F on the charged particle is called the Lorentz force (after the Dutch physicist Hendrik A. Lorentz) and is given by:

$$F = qE + qv \times B \tag{4.1}$$

The first term represents the electric field contribution, while the second is the magnetic force and has a direction perpendicular to both the velocity and the magnetic field. When Lorentz force is experienced on a wire carrying an electric current, it is called Laplace force, which is varying with the intensity of the Inducted current [38][39](see figure 4.12).

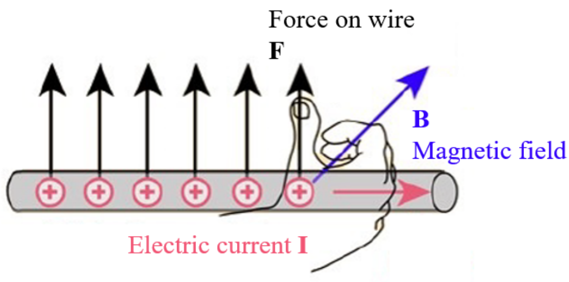

Figure 4.12: Graphical representation of Lorentz force acting on wire, with flowing current I, induced by magnetic field B.

Since a current consists of a stream of freely moving charges, a magnetic field will exert a force upon any flowing current. Considering a current I that flows through a wire, it consists of freely flowing charges, λ, moving with speed $\vec{v}$ (where the wire defines the direction of the charge movement. They are constrained by the geometry of the wire to flow in a specific direction).
We assume that in the wire of length L, dl is the infinitesimal segment of the wire. The amount of charge contained in this differential length is $dq = \lambda l$. The differential of force exerted on this piece of the wire is then:

$$dF = \lambda dl \times \vec{v} \times B \tag{4.2}$$

Because the current is effectively a vector by virtue of the speed of its constituent charges, it can be written as:

$$\vec{I} = \lambda \vec{v} \tag{4.3}$$

And find:

$$d\vec{F} = \vec{I} \times dl \times B \tag{4.4}$$

It can also be written:

$$d\vec{F} = \vec{J} dv \times B \tag{4.5}$$

Where $\vec{J}$ is the current density, dv the differential volume, and B is the magnetic field.
This scenario has direct connection to the welding process in the present project where induced current will flow thorough the previously mentioned molten metal meniscus formed at the vee, within the magnetic field generated by the work coil. In this condition, every elementary volume of molten metal dv, will be subject to a force, having a direction alternatingly pointing outward or inward, in respect to the closed geometry of the tube as a function of the alternated induction current and its frequency (see schematic representation in figure 4.13).

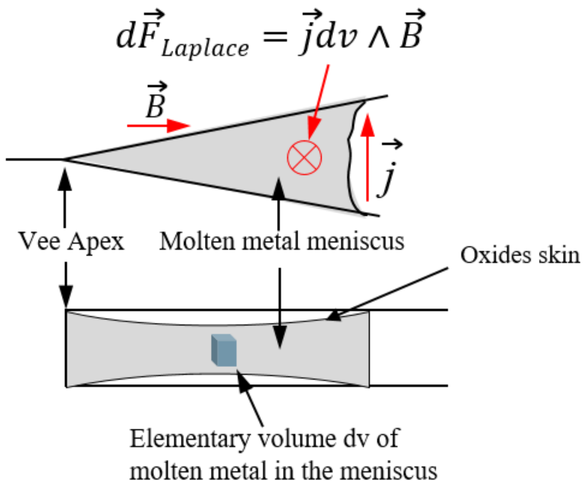

Figure 4.13: Schematic illustrating Laplace force acting on molten metal meniscus at welding Vee.

At same time, the molten metal meniscus will be subject to capillarity forces, result of a combination of adhesion force (to the still solid underlying metal) and surface tension of the liquid. These forces contribute to the formation and growth of the meniscus, having the adhesive force maintaining the liquid adherent to the edges of the vee, while surface is hold intact thanks to the surface tension. When capillarity force cannot withstand Laplace force (increasing with meniscus size), metal is ejected out of the vee, and results as spume ejection, both in and out of the tube (see example in figure 4.14). The spume mainly consists of spherical particles of 0.15 – 0.3 mm and up to 1 mm long needles resulting from the molten material being sputtered and solidified against a surface (tube inner walls) (figure 4.15).

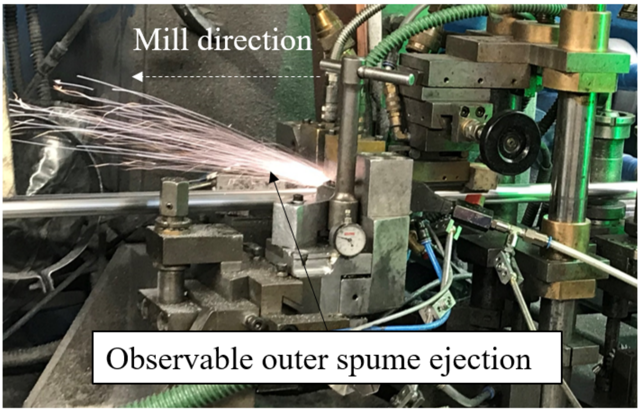

Figure 4.14: Picture taken during HF welding operations displaying spume generation.

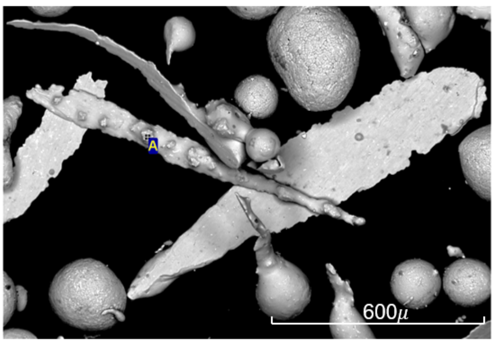

Figure 4.15: SEM picture of spume particles collected inside finished tubes.

4.2.3 Additional stages

The previously described issues govern most important part of the welding process and critical stages. However, additional steps that are important for producing a good linear welded tube, as defined in the present project, are the ones which take care of the state of the materials and shape of the strip edges. After the key embossing stage, tube forming takes place at the welding mill. The forming section of the welding line is supposed to take care of two main aspects: (i) Correct forming of strip into round tube shape and (ii) Proper shaping of strip edges.

Concerning first point, depending on the specific kind of product and welding mill manufacturer, a variable number of strands may be employed. These stands are each comprising coupled rolls, having a specifically designed nominal clearance in between them. This will allow accurate bending of the strip to a desired shape, when the strip passes through them. The stands are normally alternating in vertical and horizontal types, enabling mill operators to exert control on the rolls position (gaps) respectively in z and x directions (considering mill direction as y). Figure 4.16a presents a technical representation of a standard vertical stand with details of upper and lower rolls coupled together at nominal gap and picture in figure 4.16b shows an example of both vertical and horizontal stands' rolls. The entire forming line is thus composed of a variable sequence of vertical and horizontal paired forming rolls, like the example displayed in figure 4.17.

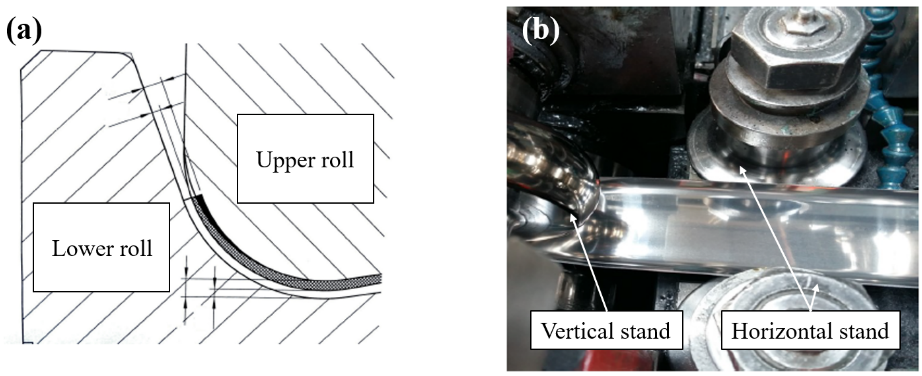

Figure 4.16: (a) Technical drawing of vertical stand rolls, assembled, in cross section and (b) picture of both horizontal and vertical stands' rolls, taken on the line.

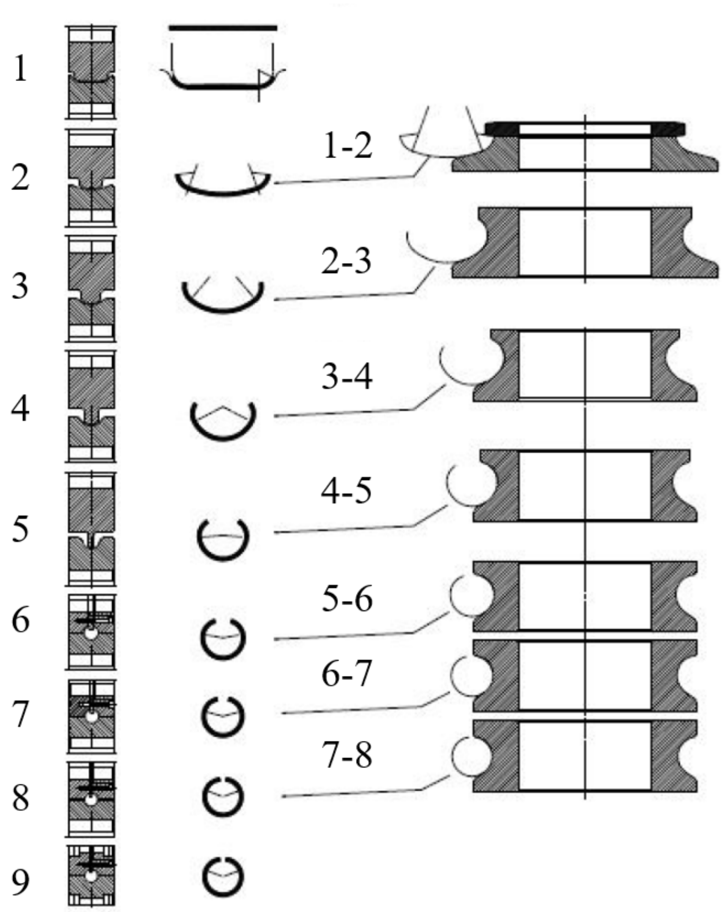

Figure 4.17: Representation of sequence of vertical (numbered 1 to 9) and horizontal stands (located in-between vertical stands, thus numbered 1-2, 2-3, etc.), with exemplified related strip bending stages.

As it is shown in figure 4.17, vertical stands number 6, 7, 8 and 9 have a different design, compared to previous ones. In particular, they present a central disk in the upper roll, so called "fin pass ring", having the role of properly shaping the strip edge upon sliding contact. The fin pass ring takes care of the proper shaping of strip edges. The exact design of a typical fin pass ring can be seen in the example picture in figure 4.18.

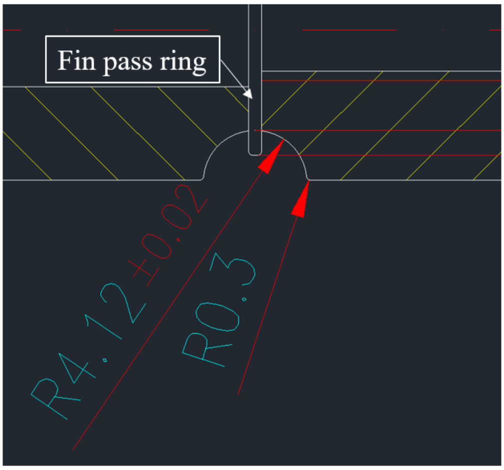

Figure 4.18: Extrapolated of station 9 upper roll's technical drawing, highlighting presence of so-called "fin pass ring".

The job of the entire forming section of the tube welding mill can be described by the so-called "flower pattern". The flower pattern is a diagram capturing all the different shape transformations undergone by the strip along the line, from first station up to the welding point. In following figure 4.19, example of a classic flower pattern for an ≈ 7 mm OD round tube is displayed.

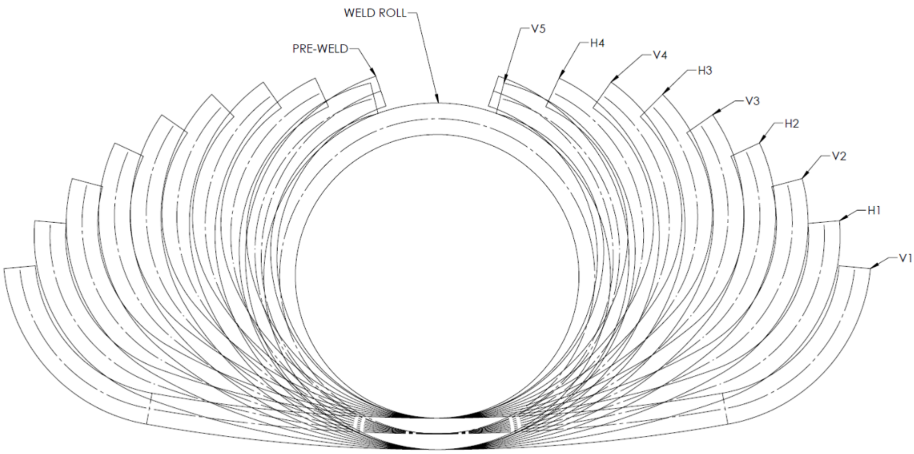

Figure 4.19: Flower pattern diagram for a round ≈ 7 mm OD tube, representing all the forming stages undergone by the strip along the line, up to the welding stage.

In addition to the above described sequence of forming rolls, a "pre-weld" stage exists (see figure 4.19), in between the end of the forming section and right before the welding. At this location, just millimetres before the induction coil, a ceramic tip is kept in sliding contact with the nearly closed strip edges. This ceramic tip, having the shape of a knife ensures optimal orientation of the edges and gives the freedom to regulate the V angle, by moving the tip up and down, as represented in figure 4.20. In order to ensure full and steady contact with the ceramic tip, so-called "pre-weld rolls" are exerting some light pressure on the formed sides of the strip.

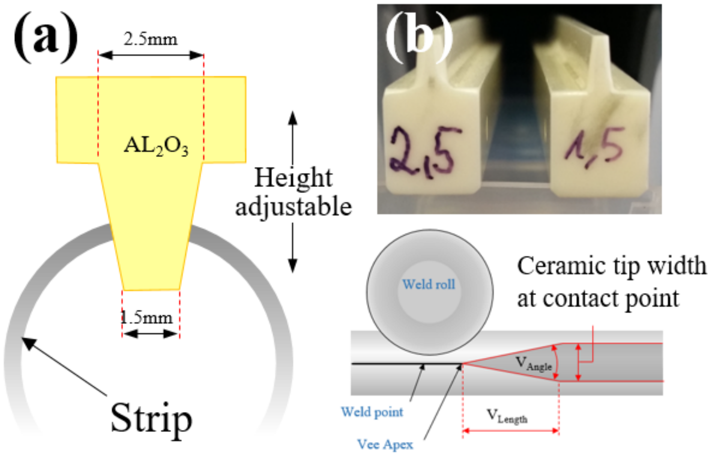

Figure 4.20: Schematic representation of the ceramic tip function and design (a) and digital picture of ceramic tips example.

Concerning post-welding stages completing the process, right after welding, the tube goes through a scarfing stage. This is done by cutting tools installed in-line and removing the weld bead formed at the outer surface of the tube. After the scarfing, the tube is sized to final dimensions thanks to a calibration section comprising of both horizontal and vertical rolls stands.

5 Innovation and Research

As an Industrial PhD, the project had two goals as pointed out earlier: (i) Industrial development of manufacturing solutions able to meet the demanding market requirements for process and product quality and (ii) in-depth research conducted on the materials and products (inner-grooved aluminium tubes) produced using the process optimized under this PhD programme.

The developmental part of the thesis, due to the strategic industrial relevance of the engineering solutions and know-how produced, could not be described in detail due to confidentiality, therefore broadly discussed in the following chapter to provide an overview. The research part of thesis is appended as three journal manuscripts intended for publication in a journal.

5.1 Process development work in this PhD

Consistent part of the Industrial PhD project work was spent in the design, development, testing and optimization of several technical inventions, focused at the improvement of: (i) process stability, (ii) process capability and (iii) final products quality.
These inventions comprised: different add-on systems that were engineered, manufactured and installed on the welding line; modification of the classic manufacturing approach, by the re-design of the welding line tooling; inclusion of additional process stages, in respect to a standard manufacturing line for cut-to-length HFW tubes.
The scope of the mentioned upgrades and introduced additional process stages was to meet ultimate market requirements for optimal inner pattern geometry of tubes, mechanical properties, key quality specifications including inner contamination level and inner weld bead height, final products form (i.e. coiled instead of standard cut to length).
The inventions were divided into three main groups:

1. Embossing technology;
2. Welding technology;
3. Post-welding technology.

5.1.1 Embossing technology development

The optimal embossed strip pattern geometry is that one which yields desired inner surface pattern of final tubes, after undergoing the modifications yielded by all the following tube forming, welding, sizing and coiling process stages. The embossing technology development work in this PhD involved critical upgrading to the standard way of manufacturing embossed aluminium strips for inner grooved welded tubes, through the introduction of some design modifications of the embossing tooling. Some of these modifications were design details of the tooling that allowed an increased material displacement control. This has led to major quality improvements in the strip condition after embossing. Such tooling features introduced special material deformation modes that corrected issues of the original standard process in terms of both surface finish and strip edge geometry accuracy. The final design solution was developed based on a number of iterations involving testing of progressively improved tooling versions, combined with microstructural characterization of embossed strips. Directly connected and supporting this work package was the development of a Finite Elements model (see chapter 7). The model, built and adjusted through the mentioned sequence of iterations, allowed simulation of the embossing process dynamics and forecasting potential effects of critical tooling design modifications. The modelling activity also allowed to find an optimal combination of process parameters that provided the optimal final strip pattern geometry (not only function of the tool pattern, but also i.e. tension, speed and pressure) and best original blank strip dimensions. As described in the chapter illustrating the research work that was more closely related to this part of the industrial development (chapter 7), the model was tailored to precisely match the mechanical properties of the materials used, which were experimentally measured. Tool materials and specially dedicated coatings were also studied, tested and implemented. The tool material was selected with the objective of providing best possible mechanical resistance to the loads applied during embossing (about 20 KN) together with optimal pattern geometry stability. Different coatings were developed and applied to different components of the tooling assembly, with the scope of minimizing friction, wear and so called "galling" of aluminium into the tool grooves. Extensive work was spent in the characterization and experimental measurement of wear and friction properties of the different PVD coatings tested. Not least was the effort spent in studying and optimizing also the tool manufacturing method, in collaboration with the suppliers, to obtain the best possible pattern geometry consistency (high precision required, with tolerances in the order of 0.01 mm), together with ensuring to match the best-available-technology constraints of the manufacturer. Moreover, the ultimate tool design included novel features able to modify the geometry of embossed strip in a way that yielded major advantages at the following welding stage.

5.1.2 Welding technology development

The welding technology development work in this PhD project was focused on stabilization of incoming strip material condition, yielding stabilized welding process and consequently stabilizing also the levels of inner contamination of tubes. Those improvements were obtained by the design, manufacturing and installation of mechanical systems able to provide in-line processing of the strip material, while running on the welding mill. This development work not only required in-depth understanding of the HF welding dynamics (part of these studies is presented in chapter 6) to find how to functionally modify the strip prior to the joining, but also required an accurate stage-by-stage characterization of the strip morphology and microstructural changes along the manufacturing line.

Additionally, the biggest achievements obtained by the modification of the welding line were: (i) the critical reduction of inner tube contamination from solid particles in final tubes with the obtainment of "spume-free" final coils (level of contamination indicatively reduced by 98%) and (ii) elimination of inner weld bead (reduced by 80%). The first of these results was obtained thanks to the invention of a new manufacturing methodology, involving the upgrade of the welding mill with the design and in-line installation of additional mechanical and hydraulic systems. Controlling and reducing the level of inner contamination of tubes proved to be the toughest of the challenges and finally led to the obtainment of two different technical solutions, exploiting same principle, but different in the setup, respectively suited for cut-to-length tubes and coiled tubes. The second was the one used for the tubes manufactured in this project. Inner contamination (spume) reduction involved not only the study of joining dynamics, but also characterization of the microstructure and composition of contamination particles, as a function of variable process parameters.

Elimination of inner weld bead was another critical aspect, which was required to meet the final products desired quality and reach the heat transfer performances enhancement closely dependent on the geometry of the inner surface of the tubes. This was obtained in combination with some of the work on spume reduction and additional re-design of the pre-forming section. This work required a thorough characterization of the deformation steps undergone by the strip during tube forming and the understanding of how these influenced the HF welding dynamics in terms of molten material displacement and “squeeze-out” during joining. Microstructural analysis (similar to the ones presented in chapters 6 and 7) supported the design, manufacturing and testing of different tooling versions that included the modification and substitution of all tooling elements of the line, from the first tube forming stage up to the weld rolls. Results were also addressed through bench performance tests of the tubes, measuring heat transfer coefficients in condensation and evaporation.

5.1.3 Post-welding technology development

One of the biggest process modifications undergone by the welding line, in respect to standard practices of HFW industry, was the shift from cut-to-length manufacturing to coiled tubes. Such modification not only requires production run without defects along the manufacturing of an entire coil (obtained thanks to the above-mentioned welding process stabilization), but also the introduction of additional critical process stages into the line. These stages were in particular an in-line annealing stage taking place after the sizing, where the tube is heated up by induction and following in-line water quenched, and a final coiling stage. The in-line annealing is a key process step in the production of coiled inner grooved tubes to provide the final products with required properties in terms of elongation, yield and tensile strength. This is required to suit following cold deformation stages (i.e. tube expansion) in the manufacturing process of mechanically assembled heat exchangers. The in-line annealing process showed to be a mandatory step, able to homogenize the final tubes’ microstructure and avoid dangerous localized gradients in terms of mechanical properties. The mentioned gradients were found to be a direct consequence of critical transformations occurring during cold deformation stages such as embossing, tube forming and the additional melting and forging of the edges (analysis presented in chapter 6 and 7). Moreover, In-line annealing both avoids the high costs of batch annealing in furnaces and gives the optimal flexibility to the tubes for the final coiling stage.
Extensive EBSD and light optical microscopy (similarly to the work

presented in chapters 6 and 7) were employed in the analysis of the in-line annealing effects on the microstructure of materials, for finding optimal annealing parameters (time, temperature). Microhardness measurements (like the ones presented in chapter 6) and tensile tests were also repeatedly used to address the effects of different annealing conditions on the materials and related mechanical performances of final products.
Figure 5.1 shows a schematic overview of the entire welding line comprising of in-line annealing, quenching and coiling.

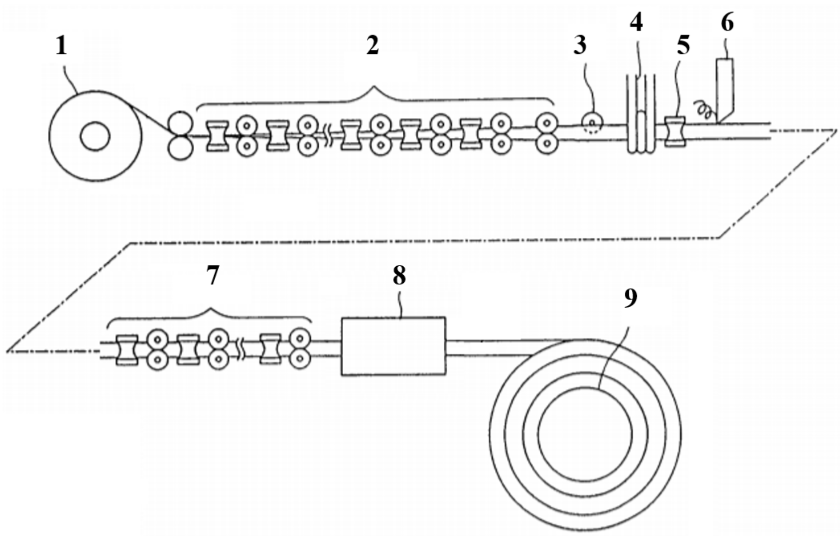

Figure 5.1: Schematic overview of the welding line stages: 1) decoiling of embossed strip; 2) tube forming stage; 3) pre-weld; 4) induction heating; 5) welding; 6) scarfing; 7) sizing; 8) in-line annealing and quenching; 9) coiling.

All the inventions and novel manufacturing approaches above illustrated cannot be described in more detail or results presented because of confidentiality requirements and ongoing IPR procedures.

Research work in this PhD

The research work constituting the core of present project was carried out on materials and products, along the different stages of the process development. This research focused on the analysis of materials behavior and product performances in terms of microstructural and corrosion issues. Microstructural transformations and corrosion behaviors of materials were studied with the scope of addressing the effects of the manufacturing process on the aluminium alloys, the morphology and performances final products. The main goal of the work was to obtain a deeper understanding of the novel process and products, from a materials and manufacturing engineering perspective, able to steer the development of innovative solutions and forecast potential corrosion issues of future on-field product life.
Present work led to different results that have been divided into three main research topics, figuratively corresponding to three main areas of the final inner grooved high frequency welded tube: (i) the weld; (ii) the tube inner grooved surface; (iii) the tube outer surface (see schematic representation in figure 5.2 below).

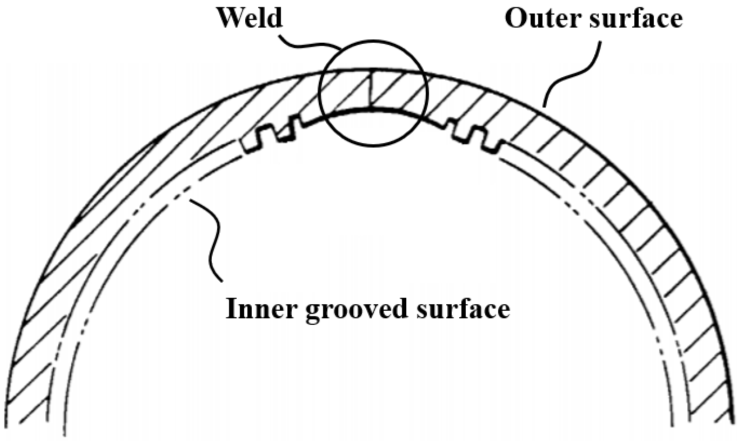

Figure 5.2: Schematic representation of the three main focus areas of the tube analysis.

The weld represents the work carried out with the scope of characterizing the microstructure of the base aluminium alloys in strip form and following the microstructure and morphology of the same materials upon welding, with the scope of establishing the relationship between HFW process and aluminium transformations at the joint.
The inner grooved surface of the tube represents a part of the work that analyzed firstly the materials deformation behavior upon embossing, with additional support from FEM simulations of such cold forming stage, and secondly the direct implications of such process on the corrosion behavior of the embossed core alloy. This alloy in operative life would be in contact with glycol based refrigerant fluids.
The outer surface of the tube represents instead the work carried out to address the corrosion performances of the finished HFW aluminium tubes in different aggressive environments, challenging the final products resistance in variable potential operative life scenarios.
The presentation of the research work was thus framed into the three following chapters (6, 7 and 8), structured in the form of separate scientific papers, illustrating the main analysis and findings of present project.

6 Welding Characterization

Full title:

Characterization of High Frequency Welded Aluminium Tube for Heat Exchangers

Authors:

G.G.B. Zaffaroni[1], O.V. Mishin[1], U.M. Ciucani[1], C. Gundlach[2], J.H. Nordlien[3], R. Ambat[1]

[1] Section of Materials and Surface Engineering, Department of Mechanical Engineering, Technical University of Denmark, DK 2800 Kgs. Lyngby, Denmark;
[2] Section of Applied Matemathics and Computer Science, Department of Physics, Technical University of Denmark, DK 2800 Kgs. Lyngby, Denmark;
[3] Innovation & Technology - Precision Tubing, Hydro Aluminium, Extruded Solutions, Hydrovegen 160 4265, Håvik, Norway

Abstract

High frequency welded microfin tubes made of embossed strips consisting of a core 3xxx-series aluminium alloy, having a thin outer layer of 7xxx-series aluminium alloy, have been investigated in this work. Characterization techniques such as scanning electron microscopy, energy dispersive X-ray spectroscopy, electron backscatter diffraction, optical microscopy, and X-ray tomography have been utilized for detailed analysis of the microstructure both in the as-received strips and final tubes. It is found that the core of the strip is heavily deformed, with a characteristic flow pattern observed near embossed regions. Welding creates a high quality joint without any observable flaws along the weld. Microstructural examinations of the weld region shows that the material is deformed by compression within 150–250 µm along the weld. Adjacent to this weld region, there are two 250–300 µm wide and partially recrystallized heat-affected zones. The deformed microstructure of the as-embossed strip is preserved at a distance greater than 0.4 mm from the joint. The microhardness of the welded tube varies in accordance with the microstructural variations with higher values in the vicinity of the joint and in the deformed regions, while lower in the partially recrystallized heat-affected zones. Correlations between the observed microstructural characteristics and the manufacturing process are discussed.

6.1 Introduction

Today there are major efforts in the Heat, Ventilation, Air Conditioning and Refrigeration (HVAC&R) industry for finding ways to increase performance, energy efficiency, durability and recyclability of the HVAC&R equipment in a sustainable way. A special focus is on replacing copper tubes and other copper components in industrial conditioning systems with aluminium products. Thanks to its attractive strength to weight ratio, good formability, efficient recyclability, inherent corrosion resistance, and possibility of surface engineering [1][2], aluminium has found a wide range of applications in the aerospace, automotive, construction, electronics, marine and food packaging industries [3][4]. Additionally, more stringent global requirements for energy efficiency in air conditioning systems and raw material costs are driving a continuous search for more efficient heat transfer systems. This has led to recent developments of aluminium tubes with enhanced inner surfaces for optimizing performances, reducing unit footprint and raw material related costs [5]. As a result of this innovating process, aluminium tube manufacturers are increasingly interested in the production of so-called microfin tubes with a variety of inner surface patterns [5]. Such microfin tubes demonstrate outstanding performances in enhancing heat transfer for both evaporation and condensation purposes without excessive pressure drop. For this reason, these tubes are widely used for air conditioning and refrigeration, where the benefit of an improved performance compensate the drawback of a major manufacturing cost [6].

In recent years, increasingly complex design patterns have been developed for optimizing the heat transfer requirements for both condensation and evaporation applications [7][8][9]. As a result, demand for tubes with non-axial symmetric patterns for the inner surface has increased (i.e. herringbone and helical cross-grooved patterns), and therefore the need for manufacturing processes different from the classic manufacturing of helically patterned tubes produced by extrusion.

The traditional extrusion of Al microfin tubes is conducted using a rotating groove mandrel inserted inside the tube and connected by a tie rod to a floating plug [5]. The latest generation of the Al microfin tubes with non-axial symmetric patterns are produced through a manufacturing cycle divided into 2 main stages namely: (i) embossing and (ii) tube high frequency (HF) welding [10][11][12]. The embossing stage consists of thread cold rolling of a strip on the surface later corresponding to the inside of the finished tube [13]. Subsequent process is the HF welding of the embossed strip. The HF welding process include longitudinally forming the embossed flat strip into a tube geometry and then welding the two strip edges together. To achieve this, the strip is fed into a forming mill that shapes the strip by different consecutive forming steps performed by several forming rolls. As the strip approaches the end of the forming line, it passes through an inductor coil, which induces electrical current, mostly concentrated at the strip edges to be joined. The edges are resistance-heated, therefore rapidly reaching the melting point. The molten edges are forged together by side squeeze rolls. When passing through the weld rolls, the oxidized and molten material are extruded out of the joint and the clean underlying material is bonded [10]. The process is completed by an in-line surface scarfing stage, aimed at removing the obtained weld bead on the outer diameter of the tube followed by sizing rolls to give the desired final geometry to the tube.

An additional advantage of HF welding for aluminium tubes is the possibility of obtaining bi-material products. In fact, the above process allows using aluminium alloy strips with cladded surfaces (hot rolled aluminium alloy liner on top of a core alloy) as precursor material. In particular, this approach can be used for manufacturing round tubes with an outer surface coated with a protecting liner of a different chemical composition than that of the core alloy. The outer surface liner usually accounts for 5 to 20% of the wall thickness [14]. Such tubes provide higher corrosion performance due to the sacrificial function of the outer layer (e.g. a 7xxx series alloy outer clad on a 3xxx core alloy) [14][15]. Manufacturing of such tubes with embossed inner patterns and cladded outer surface is impossible to produce by direct extrusion process.

The HF welding process itself relies on two main physical effects, namely skin effect and proximity effect. The skin effect is the tendency of current to be typically confined in a very shallow skin on the metal surface. As the frequency increases, the depth of the current skin penetration decreases. The proximity effect describes two opposite HF induced currents flowing near each other, leading to the current concentration on adjacent edges of the conductors [10][11]. The combination of these two effects in tube welding results in an operating condition, where most of the current (and thus induced heat) is concentrated in a shallow skin on the two opposite edges of the "vee" formed by the nearly-tube-formed strip extremities [13]. It is expected that this multistage high speed joining process can result in complex variations of the microstructure and mechanical properties along the tube.

The purpose of this work is to investigate changes in the microstructure taking place due to the HF welding in a cladded Al tube with inner surface patterns. The heterogeneity of the microstructure and hardness induced by the HF welding is analyzed using scanning electron microscopy (SEM) and energy dispersive X-ray spectroscopy (EDS). The weld region is additionally characterized by 3D X-ray tomography, electron backscatter diffraction (EBSD), and microhardness measurements.

6.2 Materials and methods

6.2.1 Materials

Aluminium strips with a thickness of 0.65 mm were used in the present work. The strips comprised a 3xxx-series commercially available Al alloy (core – 90% of the strip thickness) and a 7xxx-series Al alloy (clad – 10% of the strip thickness) added for better corrosion protection owing to the sacrificial behavior of the clad (anodic to the core [14][15]). The chemical composition of the core and clad materials is presented in Table 6.1.

Table 6.1: Main alloying elements (in wt.%) of the core and clad aluminium alloys.

Alloy	**Si**	**Fe**	**Cu**	**Mn**	**Mg**	**Zn**	**Ti**	Al
AA3xxx	$\leq$0.25	$\leq$0.4	0.5-0.6	1.0-1.3	$\leq$0.05	$\leq$0.1	0.1-0.2	Balance
AA7xxx	$\leq$0.7	$\leq$0.7	0-0.1	0-0.1	$\leq$0.1	0.8-1.3	-	Balance

Manufacturing of the strips involved joining of the core and clad alloys through hot rolling, such that the two sheets were bonded together [14]. After hot-rolling, fins were embossed on one surface, and a tube was afterwards formed and welded [10].

6.2.2 Optical microscopy

To prepare the cross-section of the tubes for optical microscopy, specimens were placed in a Struers SpeciFix-20$^{\mathrm{TM}}$ epoxy and cured at room temperature. The molded samples were then subjected to mechanical grinding using silicon carbide papers finishing with 4000 grit. Fine polishing of the specimen surface was performed sequentially using 3 µm, 1 µm, and $\frac{1}{4}$ µm diamond suspensions with intermediate ethanol rinsing. The specimen surface was then anodized using a Struers LectroPol-5 device to reveal grain structures [16]. The electrolyte and parameters used for the specimen preparation are given in Table 6.2.

Table 6.2: Details of electropolishing of specimens for optical microscopy.

Electrolyte mix	40 ml HBF_4, 760 ml H_2O
Voltage	25 V
Time	70 s
Temperature	22 °C

The back side of the molded samples was perforated until reaching the specimen surface inside and the holes were filled with an aluminium foil to establish the electrical contact necessary for anodizing. This anodizing technique described by Hone and Pearson [16] enables revealing of grain structure on the anodized surface under polarized light. Optical micrographs were taken using differential interference contrast in a Zeiss Axio Vert A1 microscope equipped with Zeiss Lambda filter, which allowed observation of the different grains being characterized by different colors.

6.2.3 SEM and EDS

SEM inspection and EDS analysis of the mechanically polished cross sections were performed using a field emission gun scanning electron microscope FEI Quanta 200^{TM} equipped with a 80mm^2 2X-Max^{TM} EDS detector from Oxford Instruments. An Aztec^{TM} SEM-EDS software was used for the analysis of the chemical composition.

6.2.4 EBSD analysis

For EBSD analysis, the specimen surface was mechanically ground and polished following the same procedure as for the specimens prepared for optical microscopy. These specimens were finally electropolished in a Struers LectroPol-5 device using an electrolyte and parameters specified in Table 6.3.

Table 6.3: Details of electropolishing of specimens for EBSD analysis.

Electrolyte mix	90 ml H_2O, 730 ml C_2H_2OH, 100 ml $C_6H_{14}O_2$, 78 ml $HClO_4$
Voltage	48 V
Time	35 s
Temperature	22 °C

The FEI Quanta 200^{TM} SEM was employed to characterize fine details of the microstructure in the backscattered electron (BSE) mode. A Channel 5 EBSD system was used to measure local orientations using a Zeiss Supra 35^{TM} FEGSEM operated at 15 kV. A step size of 0.8 µm was used for orientation mapping.

6.2.5 X-ray tomography

A 2 cm long welded tube sample was cut in half along its longitudinal axis. The half containing the weld was analyzed by X-ray tomography to obtain a three-dimensional representation of the welded area. Experiments were carried out using a "Zeiss XRadia 410 Versa" device. The instrument was operated at 50 kV and 10 W using a LE2 filter and a 10x objective. 3201 projections with an exposure time of 60 s per projection were acquired, resulting in a total acquisition time of $\sim$56 min and a pixel size of 1.52 µm was obtained using 2×2 binning. Image reconstruction was performed with an inbuilt acquisition and reconstruction software package provided by Zeiss, which is based on a Feldkamp, Davis and Kress algorithm with filtered back-projection [17]. An "Avizo 9.7.0" software from FEI was used for further analysis and visualization.

6.2.6 Microhardness measurements

Vickers microhardness measurements were carried out across the weld on the tube cross-section. Prior to the measurements, the surface was ground and polished following the procedure described in subsection 6.2.4. A Struers DuraScan 70 G5 hardness tester was used for hardness measurements with an applied load of 25 g over a rectangular area on the weld with a step size of 70 µm.

6.3 Results

6.3.1 As-received material

Figure 6.1 is an optical micrograph of the as-received strip showing grain structures in the core and clad material. In particular, it is seen that the as-received strip core material contains relatively large grains flattened along the normal direction (ND) and elongated along the rolling direction (RD). The grain length ranges from 60 µm to 120 µm along the RD and the average thickness of the grains is 25 µm. In contrast, the clad layer 7xxx alloy appears to be fully recrystallized and contains equiaxed grains of approximately 60 µm. The average Vickers hardness in the core is 58±2 HV, while the hardness of the clad is 34±2 HV.

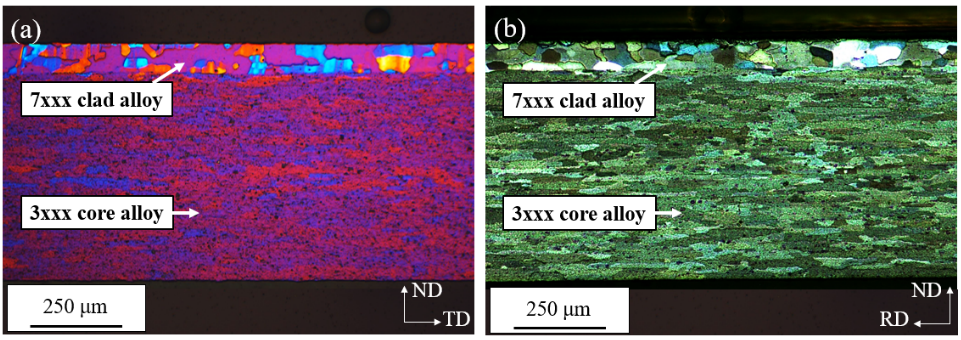

Figure 6.1: Optical micrographs from different sections of the as-received strip: (a) section containing the normal direction (ND) and the transverse direction (TD); (b) section containing the ND and the rolling direction (RD).

Figure 6.2 shows more details of the strip microstructure in BSE images. The micrograph in fig. 6.2a shows a clear difference in the level of intermetallic particles between the core and clad materials. The EDS analysis indicates that all particles in the core alloy can be described as $Al_6(Fe,Mn,Cu)$ type with different Fe/Mn content ratios. Three groups of intermetallics can be distinguished based on the particle size, shape and the Fe/Mn ratio: Group A - big (1.5–3.5 µm) and mostly equiaxed particles with a large Fe/Mn ratio (0.8), Group B - fine (0.1–1 µm) equiaxed particles having a smaller Fe/Mn ratio (0.2), and Group C - plate-like particles having lengths between 2 µm and 7 µm with a high aspect ratio and the smallest Fe/Mn ratio (0.1) (shown in fig. 6.2b).

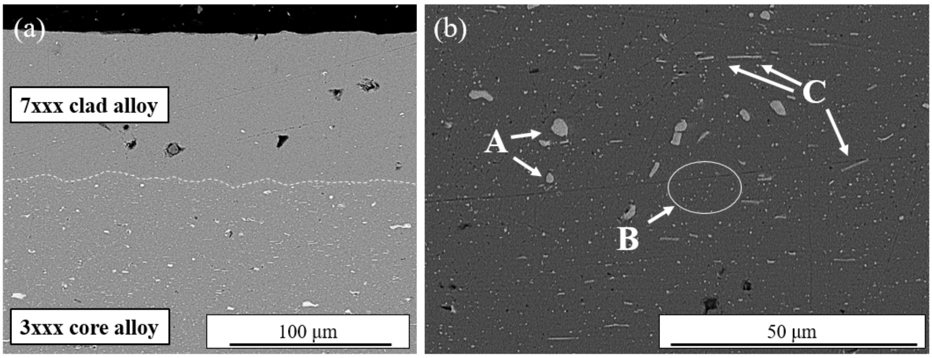

Figure 6.2: Back Scattered Electron (BSE) images of the as-received strip: (a) a low magnification image showing the interface (dashed line) between the core and clad materials and (b) intermetallic particles of different morphologies in the core.

Table 6.4 provides the chemical composition averaged over 12 particles in each group. Only a few intermetallic particles are observed in the clad layer.

Table 6.4: Results of EDS analysis (in wt.%) of intermetallic particles sorted into groups A, B and C in the core (see fig. 6.2b).

Element	**A**	**B**	**C**
O	1.9 ± 0.2	3.8 ± 0.4	2.2 ± 0.2
Al	85.1 ± 0.2	89.8 ± 0.2	92.5 ± 0.5
Mn	6.9 ± 0.1	4.9 ± 0.3	4.7 ± 0.3
Fe	5.3 ± 0.1	0.9 ± 0.1	0.3 ± 0.1
Cu	0.8 ± 0.1	0.5 ± 0.1	0.3 ± 0.1
Fe/Mn ratio	0.8	0.2	0.1

6.3.2 General characteristics of the weld

Representative images of a 3D reconstruction of the X-ray tomography analysis are shown in fig. 6.3. Weld region shows complete bonding without observable flaws, while the oxidized and molten metal was extruded out of the joint and later solidified, forming the characteristic weld bead on the tube inner surface.
Due to the need for minimizing the height of the internal weld bead (see fig. 6.3b), and to obtain stable welding, consistent condition of the edges is required. Therefore, during the embossing process, outer portions of the strip surface are typically not formed, so that no embossed material is effectively involved in the welding. A heavily deformed strip edge presenting embossed fins, hence with irregular geometry, would deteriorate the process stability, thus the joint strength. No weld bead is seen on the outer surface of the tube because it was removed by scarfing. Figure 6.3b also shows that the clad is not uniformly present across the sample surface, and locally it is removed during the welding process close to the weld region.

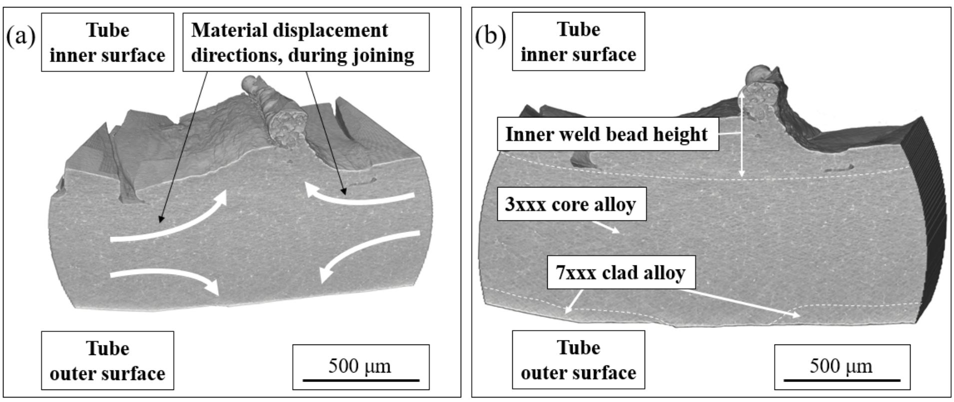

Figure 6.3: Reconstructed X-ray tomography images of the HF weld: (a) weld overview image, where arrows show directions of the molten material flow during joining; and (b) weld overview image showing core-clad interface and internal (in respect to tube) weld bead.

For complete overview of the material flow behavior during welding, a weld sample taken prior to scarfing was inspected by optical microscopy. Figure 6.4 shows the optical micrograph of the as-welded tube focusing on the outer tube surface condition. The red dotted line in this figure indicates the position, where the material would be removed by scarfing, while the white dotted line shows the joint. The micrograph shows that the clad layer remains essentially intact after the welding process, even if extruded out of the joint. Picture shows why the clad layer absent across the weld due to the scarfing process along the red dotted line. Removal of the clad layer will result in exposure of core material to outer environment. Width of this zone was approximately 182 – 200 μm wide, and is referred in this paper as "devoid-of-clad" area.

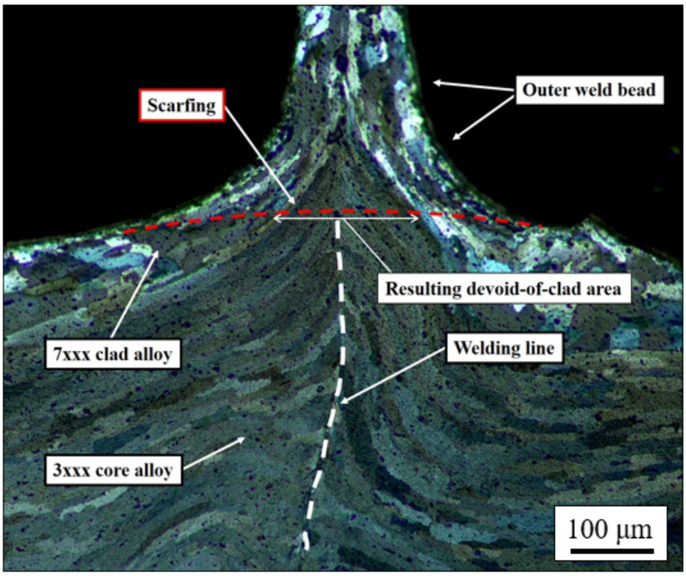

Figure 6.4: Optical micrograph of the tube cross section showing the outer weld bead.

6.3.3 Microstructure of the welded tube

As mentioned in section 6.3.1, the core and clad materials can be clearly distinguished in the BSE images due to the higher number of intermetallic particles in the core and difference in grain structure. Figure

6.5 shows a detailed SEM image of the weld tube cross-section. No appreciable change in the spatial and size distributions of particles along the weld is observed as compared to other regions away from the weld. Similar to the observation from X-ray tomography and light optical microscopy, Figure 6.5a shows the tube surface with the characteristic devoid-of-clad area (see the red dotted lines in figure 6.5a). The EDS maps in fig. 6.5b, 6.5c show the distributions of Mn and Zn in the weld area. As expected, the devoid-of-clad area presents a higher Mn content and lower Zn content with respect to the adjacent near-surface regions again showing the absence of Zn-rich clad material.

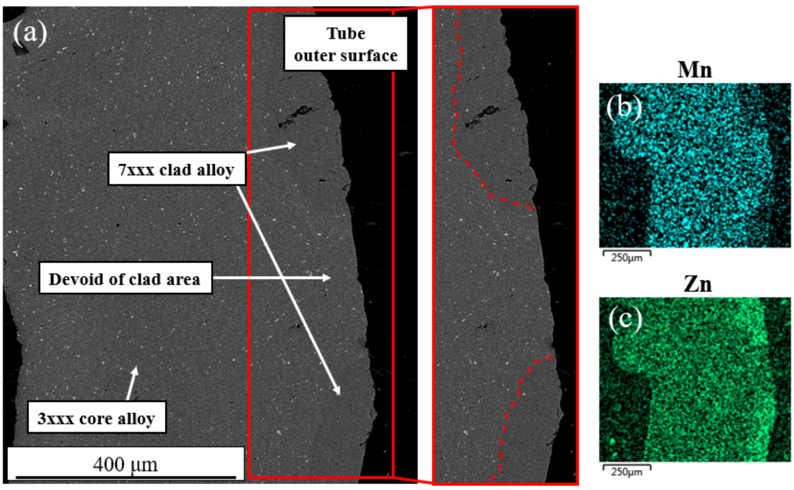

Figure 6.5: SEM analysis of the weld cross-section: (a) Overview BSE image, where the area without clad is marked by an arrow and separately shown the upper part of the cross-section with the red dotted line to indicate the area without clad; (b) and (c) are EDS maps for Mn and Zn, respectively.

Results of the EBSD analysis of the weld region are shown in fig. 6.6. Several regions can be distinguished in this figure, namely: (i) an approximately 200 µm wide weld region containing fine subgrains and plenty of low angle boundaries (LABs), (ii) two 250–300 µm wide partially recrystallized heat affected zones (HAZs), and (iii) the deformed microstructure which appears unaffected by HF welding (base material).

The average size of recrystallized grains in the HAZs is approximately 15 µm. Interestingly, the bead at the weld is also recrystallized (see fig. 6.6b) except for the outermost part which is re-solidified with a very small grain size, 5–6 µm. The upper part of the fig. 6.6 shows the deformed microstructure similar to that in the as-received strip (see fig. 6.1). This microstructure is characterized by a high aspect ratio of the deformed grains and a high frequency of LABs. The width of the flattened grains in this microstructure is 7 µm. Close to the embossed fins, the microstructure is somewhat different, with a characteristic flow pattern as a result of cold deformation during embossing.

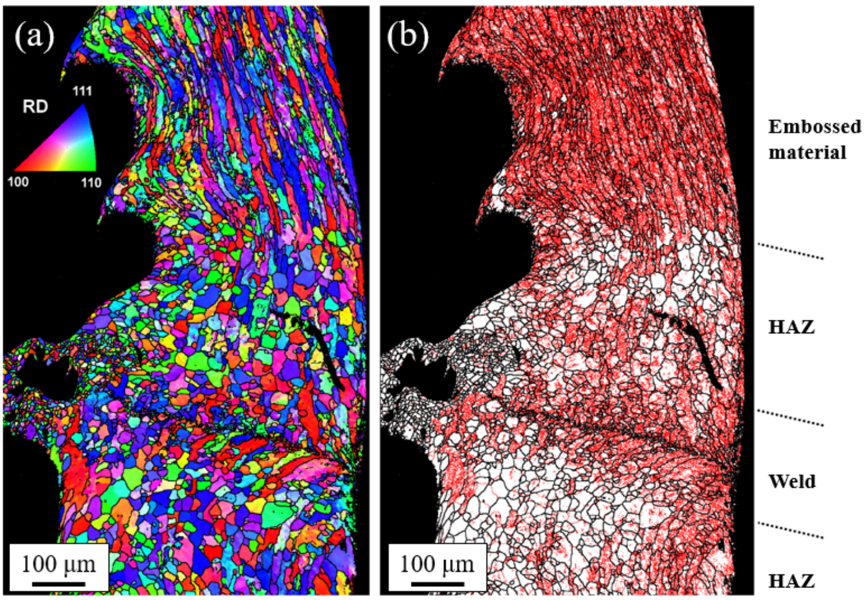

Figure 6.6: EBSD analysis of the weld region: (a) orientation map colored according to the crystallographic plane, (b) misorientation map displaying low angle boundaries (2–15°) in red and high angle boundaries (>15°) in black. A curved black region close to the outer surface is a scratch introduced during specimen handling, where no indexing of EBSD patterns was possible.

6.3.4 Microhardness

Results from the microhardness measurements are shown in fig. 6.7. The Vickers hardness ranges from a minimum of ~55 HV in the HAZ region to a maximum of ~68 HV in the weld region. The hardness map encompasses the microstructural description provided by the EBSD analysis, as displayed in fig. 6.6b. The lowest hardness corresponds to the nearly fully recrystallized HAZ region characterized by equiaxed grains and the lowest content of LABs, while the higher hardness regions correspond to the deformed microstructure in the weld and in the embossed regions. The average hardness of the embossed material (core alloy) is approximately 66±3 HV.

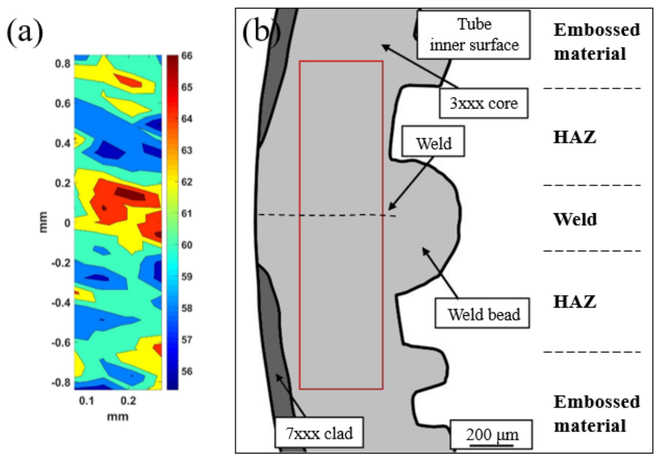

Figure 6.7: Vickers hardness map (a) and schematic representation of the cross-section of the tube surface (b) with the red frame showing the region where HV values were measured.

6.4 Discussion

The X-ray tomography data obtained for the HF weld of the Al tube investigated in the present work clearly demonstrate that all molten material formed at strip edges was effectively extruded out of the weld, leaving no traces of the molten and re-solidified material in the weld structure. In addition to outward displacement of the melt material, due to applied horizontal pressure from the two edges being forged together, electromagnetic pressure also contributes to the flow [18]. The edges melt before they meet each other and molten metal is continuously removed from the beginning of the melt to the end of welding due to the electromagnetic pressure derived from current induced on opposing edge surfaces, which is reciprocally repulsing [18]. Some evidence of the re-solidified material is observed only in the innermost portion of the tube weld bead (fig. 6.6), however, the weld did not show any oxide inclusions. The melting point of aluminium oxide is approximately 2327 K [19], however the melting point can be lowered [20] for a thin oxide layer on the aluminium surface (typically of 3-5 nm [21][22] to a level of approximately 1800 K [20]). At the same time, HF welding process temperatures reach values that are just slightly above the melting temperature of aluminium (933 K) [10]. Therefore, the temperature is locally high enough to melt the strip edges, but never enough to melt the thin oxide layer which is pushed out during the welding. These dynamics avoid the inclusion of aluminium oxides present on precursor strip surface in the weld. At the same time, while melt material is extruded out of the joint, direct contact between the underlying non-molten edges and air is avoided, thus preventing any further oxidation of the forged joint.

The microstructural characterization carried out in this work shows that the joining process does not result in any appreciable change in the spatial and size distributions of particles along the weld. In contrast, there are significant changes in the grain structure as a result of welding. A very fine and heavily distorted grain structure is formed along and near the weld line. This structure results from a significant compression strain at the joining interface and is characterized by a high frequency of LABs. The adjacent HAZ regions on both sides correspond to the material affected by the local heating caused by induction. The microstructural characterization shows the presence of fine deformed subgrains combined with larger strain-free recrystallized grains, which suggests that the heating was sufficient to cause partial recrystallization. In the embossed fins along the joint, recrystallized grains are also present. As is evident from Fig.6, the heat was confined to approximately 0.4 mm on each side across the joint, therefore beyond this distance, the deformed microstructure of the as-embossed

strip is preserved with flattened grains along the ND of the initial strip and showing characteristic flow patterns close to the embossed surface (see fig. 6.6). Such narrowly confined heat penetration is obtained by optimally exploiting both the so-called skin and proximity effects due to the remarkably high induction frequencies employed in the manufacturing of the tubes (i.e. 600 – 700 kHz) [10][11][12].
The microstructural heterogeneity observed across the weld causes variations in microhardness. The material is hard both in the vicinity of the joint where the microstructure is deformed by compression and in the base material (see fig. 6.7). As expected, the partially recrystallized microstructure in the HAZs is much softer than the microstructure in the deformed regions. Thus, the hardness map is consistent with the microstructural analysis provided by EBSD. The change in hardness in the weld region is an important aspect in connection with the application of the tube and performance. The hardness map highlights critical gradients in mechanical properties of the core material. This condition would determine the presence of a singularity, hence a weak site, in the finished tubes, that may yield premature failure. It is expected that a localized hardness gradient across the tube wall can considerably reduce their maximum bearable pressure and also negatively affect their performance under cold forming steps involved in the heat exchanger assembling (inconsistent behavior during mechanical expansion and bending).
The results obtained suggest that a post-welding heat treatment of the tubes may be employed for reducing the heterogeneity of the microstructure and hardness across the joint. Finally, the results presented highlight an important aspect of the required post-weld scarfing, i.e. that the scarfing process removes locally the clad layer, therefore directly exposing the core material to outer environment, with potential effects on its corrosion resistance [23][24]. Therefore, in order to avoid the removal of the clad, a process or strips design modification may be required. Otherwise, implications of such singular surface condition on the corrosion performance of the final products might be an important aspect to be verified and tested.

6.5 Conclusions

The microstructure and microhardness have been investigated in high frequency welded microfin tubes made of embossed strips consisting of a core 3xxx-series aluminium alloy with a thin outer layer of a 7xxx-series aluminium alloy. Based on this investigation, the following conclusions are obtained.

1. A complete and pore-free joint is created by compression of induction heated edges with no evidence of oxide presence found along the weld. The manufacturing process involves scarfing of the outer surface of the weld, which results in a small "devoid-of-clad" area along the longitudinal direction of the tube.

2. It is found that within 150–250 µm along the weld, the compressed microstructure contains fine subgrains separated by mostly LABs. Adjacent to this weld region, there are two 250–300 µm wide HAZs. The HAZs are partially recrystallized with an average recrystallized grain size of 15 µm. The as-embossed microstructure characterized by high frequency of LABs preserved at a distance greater than 0.4 mm from the joint, and a characteristic flow pattern is observed near the embossed fins.

3. The microhardness in the welded tube varies in response to the microstructural variations. The Vickers hardness ranges from $\sim$55 HV in the partially recrystallized HAZ region to $\sim$68 HV in the weld region which presents the compressed microstructure. The average microhardness was also high, 66$\pm$3 HV, in the embossed core alloy beyond the HAZs.

Aknowledgements

The authors would like to thank Norsk Hydro and Innovation Fund Denmark (grant 5189-00144B) for their technical and financial support of the project. We also thank Mr. A. Mangelsdorf, Dr. M. Pasqualon and Mr. T. Guillaume from Norsk Hydro for their support. The 3D Imaging Centre at the Technical University of Denmark is gratefully acknowledged. Dr. C. Gundlach is grateful for financial support from Innovation Fund Denmark via grant 5152-00005B.

Bibliography

[1] M. Leary, Materials selection and substitution using aluminum alloys. In: Roger Lumley (Ed.). Fundamentals of Aluminum Metallurgy: Production, Processing and Applications, Cambridge UK: Woodhead Publishing Limited (2011) 784–827.

[2] C. Vargel, M. Jacques, M.P. Schmidt, Chapter A.1 - the advantages of aluminum. In: C.V.J.P.B.T.-C. of A. Schmidt. Elsevier. Amsterdam (2004) 9–16.

[3] T. Dursun, C. Soutis, Recent developments in advanced aircraft aluminum alloys, Mater. Des. 56 (2014) 862–871.

[4] W.S. Miller, L. Zhuang, J. Bottema, A.J. Wittebrood, P. De Smet, A. Haszler, A. Vieregge, Recent development in aluminum alloys for the automotive industry, Mater. Sci. Eng. A 280 (2000) 37–49.

[5] M. Hofuku, Development trends in inner-grooved tubes in Japan, Hitachi Cable Review. 26 (2007) 1–3.

[6] L.P.M. Colombo, A. Lucchini, A. Muzzio, Flow patterns, heat transfer and pressure drop for evaporation and condensation of R134A in microfin tubes, Int. J. Refrig. 35 (2012) 2150–2165.

[7] R. Kaji, S. Yoshioka, H. Fujino, The effect of inner grooved tubes on the heat transfer performance of air-cooled heat exchangers for CO_2 heat pump system. International Refrigeration and Air Conditioning Conference; Purdue, July 16-19 2012.

[8] Z. Wu, B. Sundén, Vishwas V. Wadekar, W. Li, Heat transfer correlations for single-phase flow, condensation and boiling in microfin tubes, Heat Transfer Eng. 36 (2015) 582–595.

[9] J.A. Olivier, L. Liebenberg, J.R. Thome, Heat transfer, pressure drop, and flow pattern recognition during condensation inside smooth, helical micro-fin, and herringbone tubes, Int. J. Refrig. 30 (2007) 609–623.

[10] R.K. Nichols, PE, H.N. Udall, High frequency welding of aluminum. A Thermatool Corp. Publication, T.P. n. 111, Rev. 2. March 1999.

[11] J. Wright, Optimizing efficiency in HF tube welding processes. in: Tube & Pipe Technol. November/December 1999.

[12] K. Hyun-Jung, Y. Sung-Kie, Three dimensional analysis of high frequency induction welding phenomena, Trans Korean Soch Mech Eng A, 30 (2006) 865–972.

[13] D. Zhou, X. Chengdong, J. Lv, L. Li, inventors; Yinbang Clad Material Co., LTD, assignee. Aluminum alloy composite strip for internal threaded heat exchange tube and manufacturing therefor. World Intellectual Property Organization Patent WO 2018049585 A1. Mar 22 2018.

[14] B. Ren, inventor; Arconic Inc., assignee. Multi-layer aluminum alloy sheet product for tubes for heat exchangers. United States Patent US 9964364 B2. Mar 08 2018.

[15] E. Bardal, Corrosion Protection by Coatings. In: Corrosion and protection, Springer-Verlag London Limited, UK, (2004) 282-291.

[16] A. Hone, E.C. Pearson, Metal Progr. 53 (1948) 363–366.

[17] L.A. Feldkamp, L.C. Davis, J.W. Kress, Practical cone beam algorithm, J. Opt. Soc. Am. A 1 (1984) 612–619.

[18] H. Haga, K. Aoki, T. Sato, Welding phenomena and welding mechanisms in high frequency electric resistance welding-first report, Weld. J. 59 (1980) 208–216.

[19] M.W. Chase, J. Phys. Chem. Ref. Data, Monograph, 9 (1998) p. 1.

[20] E.L. Dreizin, D.J. Allen, N.G. Glumac, Depression of melting point for protective aluminum oxide films, Chem. Phys. Lett. 618 (2015) 63–65.

[21] V.Y. Gertsman, Q.S.M. Kwok, Microsc. Microanal. 11 (2005) 410–420.

[22] F. Reichel, L.P.H. Jeurgens, G. Richter, E.J. Mittemeijer, J. Appl. Phys., 103 (2008) 093-515.

[23] M. Edo, S. Kuroda, A. Watanabe, K. Tohma, Localized corrosion of aluminum clad sheets in alkaline solution, 53 (2003) 55–60.

[24] T. Fukui, H. Irie, S. Kimura, Z. Tanabe, A study on application of sacrificial anode Al-Zn alloy to aluminum heat exchangers, J. Japan Inst. Light Metals, 29 (1979) 410–417.

7 Inner Corrosion

Full title:

Corrosion of Herringbone Grooved Embossed Aluminium Strips for Heat Exchanger Tubes

Authors:

G.G.B. Zaffaroni[1], V. C. Gudla[2], S. Laganá[1], C. Gundlach[3], B. Olsson[4], J.H. Nordlien[4], R. Ambat[1]

[1] Department of Mechanical Engineering, Technical University of Denmark, DK 2800 Kgs. Lyngby, Denmark;
[2] Henry Moseley X-ray Imaging Facility, Department of Materials, University of Manchester, M13 9PL Manchester, United Kingdom;
[3] Section of Applied Matemathics and Computer Science, Department of Physics, Technical University of Denmark, DK 2800 Kgs. Lyngby, Denmark;
[4] Innovation & Technology - Precision Tubing, Hydro Aluminium, Extruded Solutions, Hydrovegen 160 4265, Håvik, Norway

Abstract

This paper investigated the effect of embossing on a AA3xxx Al alloy sheet on the microstructure and corrosion behaviour. The microstructure of the embossed aluminium sheets was studied by differential interference contrast microscopy, scanning electron microscopy (SEM), Transmission Electron Microscopy (TEM), Energy Dispersive X-ray Spectroscopy (EDS), Focused Ion Beam microscopy (FIB), and X-Ray Computational Tomography. Finite Elements Modelling (FEM) of the embossing process supported the experimental analysis. The corrosion behaviour of the embossed sheets was assessed using potentiodynamic anodic polarization tests followed by corrosion surface morphology analysis using SEM. Results showed a modification of the microstructure of the alloy during embossing, which is dependent on the embossed pattern geometry and the roll forming direction. Non-symmetrical displacement of material, in respect to the pattern geometry, was caused by the anisotropic forming pressure applied on the strip during roll forming. Such phenomenon yielded formation of more corrosion-susceptible sites on the embossed aluminium surfaces, in correspondence to specific geometrical features.

7.1 Introduction

In industrial applications such as Heat, Ventilation, Air Conditioning, and Refrigeration (HVAC&R) have given paramount importance to the heat transfer performance of the used materials. In heat exchangers (HXs), those mainly constituted of tube-fin batteries, special attention is paid to optimization of the materials and system design to improve the heat exchanger efficiency [1][2][3][4]. This focus is translated into the research for improved design of both fins and tubes together with attention to environmental issues [1]. As a result, development of all-aluminium solutions for heat exchanger units is under progress, which allows recycling of complete devices without issues pertaining to disassembly. Use of aluminium also provide substantial corrosion resistance for the heat exchanger components. To further enhance the heat transfer performance, aluminium tubes with increasingly complex inner surface patterns have developed with the possibility of nearly triplicating

heat transfer coefficients [1][2][3][4].
Inner surface enhanced tubes can be produced by extrusion processes if the inner patterns are helical. However, helical pattern does not provide high heat transfer capabilities. More complex surface pattern geometries such as herringbone pattern can further enhance the heat transfer properties. However, this requires unconventional manufacturing processes other than extrusion in order to introduce the complex pattern to the interior surface of the tube [5]. Therefore, these products are manufactured by aluminium strip embossing, for obtaining surface pattern enhancement, followed by stages of tube forming and high frequency welding to provide the final inner surface embossed heat exchanger tubes [5][6].
Traditionally, the technology of inner surface enhanced tubes was applied to Cu tubes, and the technology is now extended for aluminium tubes. The process for manufacturing of micro-fin Cu tubes using ball spin forming technique has been shown to induce anisotropies in the plastic flow of the metal, and defects such as folding defects [7][8]. The embossing process on the aluminium strip surfaces introduce considerable cold deformation, which result in local microstructural changes. Further it is well known that surface mechanical deformation of aluminium results in a near–surface deformed region also known as Beilby layer [9][10][11][12][13]. This layer is usually characterized by a very fine grain structure, with higher amounts of incorporated Al oxides and processing-related organic contamination along with finer intermetallic phases that are fractured and refined in their size [14][15][16][17][18].
It is known that the presence of near surface deformed layer negatively influences the corrosion resistance of Al alloys, and impedes the performance of conversion coatings and the applied top coatings [19][20][21][22]. The embossing process generate deformation at higher depth levels affecting the morphology and texture of the grains, which will also have an influence on the general corrosion behaviour [23], as well as environmentally induced cracking susceptibility [24][25].
Additional aspect is the tube forming after the embossing process using the high frequency welding process. The weld region microstructure will be affected by the modification of the microstructure during the welding process. The material used for the aluminium heat exchangers are cladded alloys (AA3xxx alloy with a thin clad layer of AA7xxx

for sacarificial protection). The clad layer can mix up with the core AA3xxx alloys during the welding process, therefore influencing the weld region microstructure and corrosion [26][27][28][29]. The whole heat exchanger is destroyed if there is a vertical penetrating pit growth in these damaged regions.
This paper presents the results from investigations on the effect of embossing on the corrosion behaviour of strips of AA3xxx series Al alloy sheet (cladded with a sacrificial AA7xxx aluminium alloy on the side corresponding to final outer surface of tubes) meant for HVAC&R applications [30]. The inner surface of the AA3xxx strip (side without AA7xxx cladding) was embossed with a herringbone structure [31]. Finite Element Modelling (FEM) was used to understand stress and strain development during the embossing process. Results from FEM modelling were compared with the experimental microstructural analysis of the embossed patterns using SEM, FIB, and X-ray tomography. The corrosion behaviour of the embossed sheets was investigated using potentiodynamic polarization tests in NaCl containing solution and in glycol-based coolant solutions simulating the inner operating conditions of the tube. The microstructure and corrosion morphology of the surface of the embossed and non-embossed materials were studied using differential interference contrast microscopy, scanning electron microscopy (SEM), Transmission Electron Microscopy (TEM), Energy Dispersive X-ray Spectroscopy (EDS), Focused Ion Beam (FIB), and 3D X-Ray tomography analysis.

7.2 Materials and methods

7.2.1 Materials

Table 7.1 shows the chemical composition of the strip core material (AA3xxx alloy) and the sacrificial outer clad (AA7xxx alloy). Total thickness of the strip was 0.7 mm with 10% of the thickness covered by clad material, and the as-received material was in O temper. For various investigations, as-received and embossed materials were used. The non-cladded inner surface of the strip was embossed with a herringbone pattern through a cold rolling process, and the process is thoroughly described in patent WO 2018/049585 A1 [6].

Table 7.1: Main alloying elements (in wt.%) of the core and clad aluminium alloys.

Alloy	Si	Fe	Cu	Mn	Mg	Zn	Ti	Al
AA3xxx	≤0.25	≤0.4	0.5-0.6	1.0-1.3	≤0.05	≤0.1	0.1-0.2	Balance
AA7xxx	≤0.7	≤0.7	0-0.1	0-0.1	≤0.1	0.8-1.3	-	Balance

7.2.2 Finite Elements analysis of strain and stress distribution in the embossed strip

Simulation of the stress distribution across the embossed surface has been carried out using non-linear explicit FEM code IMPETUS Area Solver. The geometry model and FE meshing of the rolling process are shown in Figure 7.1a and 7.1b.

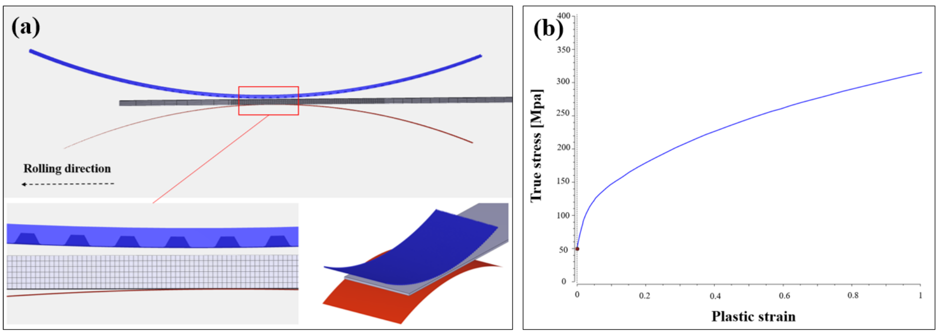

Figure 7.1: Geometry and meshing used for the Finite Elements model (a) and Elasto-plastic behaviour of strip material, represented by the true stress vs plastic strain curve (b).

Stress distribution was calculated corresponding to ambient temperature without considering the increase in temperature due to the thermal effect of deformation and friction. However, the aim of the simulation was to determine the relative difference in stress and strain distribution over the patterned surface. The AA3xxx strip alloy was chosen as the elasto-plastic material (see true stress vs. plastic strain curve of the material in fig. 7.1b), while no strain rate effects were taken into account in the material data. Table 7.2 shows the material parameters that were used for the modelling. The model did not consider presence of AA7xxx clad aluminium alloy on the back of the core material, which is very thin.

Table 7.2: Material parameters used for the FEM modelling.

Variable	**Value**
Density [kg/m3]	2700
Young modulus [MPa]	70000
Poisson's ratio	0.33
R00	0.65
R45	0.85
R90	0.40

The strip with initial dimensions of 0.7x25x225 mm (TxWxL) was meshed with third order brick elements. The element size was 0.1 mm in the deformation area and larger further away from the rolls. The number of nodes through thickness was 19, while the total number of elements in the strip was 342,000. No re-meshing was implemented in the simulation.
The work rolls were assumed to be rigid and they were meshed with shell elements of size 0.1-0.2 mm. The friction coefficient was set to 0.15, while the type of friction was assumed to be coulomb friction. The upper roll was first lowered to a gap of 0.4 mm followed by rotation of the rollers have started giving a speed of 500 mm/s of the sheet. Tension forces were applied to the front (100 N) and end of the sheet (300 N).

7.2.3 Optical microscopy

Differential interference contrast microscopy was carried out on the embossed strip samples that were hand cut in orthogonal to the rolling direction. Specimens were mounted in a Struers SpeciFix-20™ epoxy and cured at room temperature. The moulded samples were then subjected to mechanical grinding using silicon carbide polishing papers (from 220 grit to 4000 grit) with intermediate alcohol rinsing between each polishing step. Finer polishing of the surfaces was then performed using a 3 µm, 1 µm, and a $\frac{1}{4}$ µm diamond suspension with intermediate ethanol rinsing, and finally air dried. Afterwards, the back side of the moulded samples was perforated until the back surface of the specimen and the holes were filled with an aluminium foil to establish the electrical contact necessary for anodizing. This technique described by Hone and Pearson [32] enables to reveal the grain structure of aluminium by observing the anodized surface under polarized light. The differently oriented grains will appear with different levels of brightness and colour. Sample surfaces were anodized with a Struers LectroPol-5, an automatic, microprocessor controlled electrolytic polishing and etching device for metallographic specimens. The electrolyte and parameters used for the specimen preparation are given in Table 7.3. Optical micrographs were taken using differential interference contrast in a Zeiss Axio Vert A1 microscope equipped with Zeiss Lambda filter.

Table 7.3: Details of the parameters used for electropolishing for optical microscopy.

Electrolyte mix	40 ml HBF_4, 760 ml H_2O
Voltage	25 V
Time	70 s
Temperature	22 °C

7.2.4 Electron microscopy

Scanning Electron Microscopy (SEM) was carried out on the strip samples, both blank and embossed, that were cross-sectioned orthogonally in respect to the rolling direction. Samples were mounted in a Struers SpeciFix-20^{TM} epoxy resin and cured at room temperature. The moulded samples were then subjected to mechanical grinding and polishing following same procedure described for specimens prepared for differential interference contrast microscopy examination. SEM analysis of sample surfaces were carried out on strip samples cut to 3 cm in length with sites of interest in the middle of embossed surface.
SEM inspections were performed using a field emission gun scanning electron microscope. Energy dispersive X-ray spectroscopy was performed for obtaining the elemental analysis from the regions of interest. An environmental scanning electron microscope model FEI Quanta

200™ Field Emission Gun SEM (FEG-ESEM) equipped with an energy dispersive spectrometer (EDS) (Oxford Instruments 80mm^2 X-Max™ coupled with an Aztec™ SEM-EDS software) was used for the analysis. Scanning transmission electron microscopy was performed on the samples prepared from the regions of interest using a FEI Tecnai™ T20 G2 operating at 200 keV. EDS analysis and mapping were performed in the TEM using Scanning TEM (STEM) mode and data were collected using an Oxford Instruments 80mm^2 X-Max™ detector coupled to an Aztec™ TEM-EDS analysis software. Thin film lamella from the region of interest for the TEM analysis was prepared using site specific in-situ lift out technique using FIB milling, and the in-situ lift out of the thin film lamella was performed using an Omniprobe™ micromanipulator coupled to the FIB-SEM [33][34][35][36]. The thin film sample that was lift out, was further thinned down to approx. 120 nm thickness for electron transparency and was milled with a low energy Ga ion beam (1 keV) to remove any prior high-energy milling induced artefacts. Mounting of the thin film lamella was performed onto Cu TEM sample grids with the help of in-situ Pt deposition to weld the sample to the grid. In-situ sectioning and imaging of the regions of interest was performed using a FEI Helios Nanolab™ Dual beam FIB-SEM operating at 30 keV equipped with a Ga^+ liquid metal ion source (LMIS) coupled to a FEG-SEM. Regions of interest were protected from ion beam induced damage during ion beam imaging by in-situ deposition of Pt over the region of interest using a Pt Gas Injection System.

7.2.5 X-ray computational tomography

In order to acquire a three-dimensional representation of the sample, X-ray micro computed tomography was carried out using a "Zeiss XRadia 410 Versa" device. Strip samples of length 3 cm was used with sites of interest located in the middle of embossed surface. The instrument was operated at 60 kV and 10 W using the LE2 filter and 10X objective. 3201 projections with 20 s exposure time per projection were acquired resulting in a total acquisition time of 19:19 h:min and a pixel size of 1.35 µm was obtained using 2x2 binning. Image reconstruction was performed with an inbuilt acquisition and reconstruction software package provided by Zeiss, which is based on a Feldkamp, Davis and

Kress (FDK) algorithm using filtered back-projection [37]. For further analysis and visualization, the software "Avizo 9.7.0" (FEI) was used.

7.2.6 Potentiodynamic polarization experiments

Potentiodynamic polarization tests were performed on both blank and embossed samples, cut to 3 cm in length. The strip test coupons were investigated by potentiodynamic anodic polarization in both neutral pH 0.1M NaCl aqueous solution and a glycol-containing solution (Table 4) resembling operative life conditions (a standard commercial inhibitor-containing solution used for radiators and for radiator testing according to ASTM D1384 [38]) of non-automotive radiators. Additional 250 ppm NaCl was added to the glycol solution to resemble possible levels of field contamination [39]. Measurements were carried out using an ACM Instruments GillAC potentiostat.

Table 7.4: Glycol-containing aqueous solution chemical composition.

Element	**Quantity**
CorrShield OR4410 inhibitor	0.0105 %
AZ8104 inhibitor	0.0032 %
Spectrus NX1164 biocide	0.0090 %

Anodic polarization experiments were conducted in a flat corrosion cell (cell from Qvarfort [40]). The measurements were performed on an area of 1 cm^2, and a solution volume of 100 mL against a KCl saturated Silver Chloride (Ag/AgCl) reference electrode. Anodic polarization scans were performed after a cell settle time of 3600 s at a scan rate of 60 mV/s. Strip samples were all tested in potential range starting from OCP -100 mV to OCP +1000 mV.

7.3 Results

7.3.1 Finite Elements analysis of strain and stress distribution in the embossed strip

Figure 7.2 shows the results from FEM simulation of the deformation of the strip during the embossing process. Figure 7.2a shows the progressive deformation steps (from right to left) during the process. Simulation shows that there is a mismatch between the tool grooves geometry and the manner in which the material was plastically flowing and filling the upper tracks of the roll (negative of the desired final strip pattern). The grooves were not filled uniformly, and while undergoing cold deformation, the aluminium metal appeared to be predominantly forced against one side of the groove (indicated as side 1 in fig. 7.2a) and is observed to preferentially climb along its surface. In agreement with the above material deformation behaviour, the results presented in figure 7.2b show the distribution of plastic strain and mesh grid lines of the embossed aluminium, highlighting the asymmetry in the material deformation with respect to the fin nominal geometry. For example, the white circled area in figure 7.2b shows the bottom side of the fin (side 1) with mesh lines severely deformed (with respect to side 2) and higher effective plastic strain that is locally concentrated.

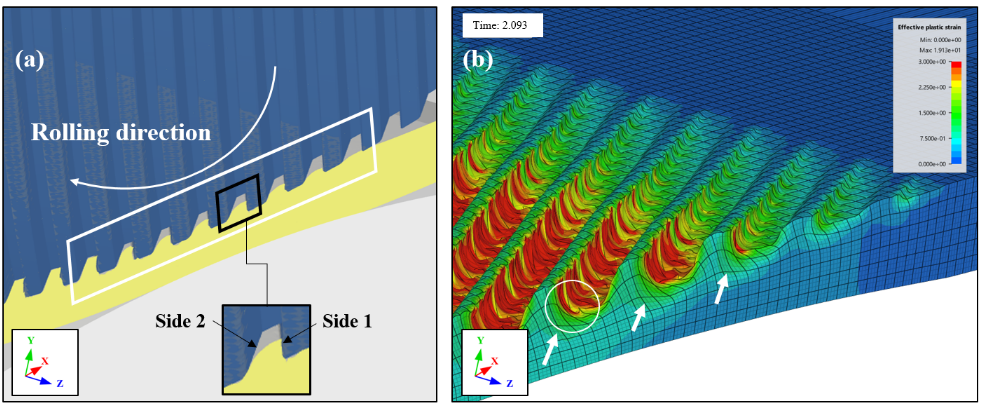

Figure 7.2: Finite Elements simulation results: (a) overview of strip material deformation during embossing with cross section displaying material displacement behaviour; (b) Effective plastic strain distribution.

Figure 7.3a and 7.3b show simulation results with the effective stress levels highlighted in colour scale. The two representations are captured from two different points of view, with a rotation of 90° in the xy plane with respect to each other. This allows qualitative and comparative assessment of the considerably higher amount of stress for those surfaces corresponding to side 1 (fig. 7.3a with fins side 1) against side 2 (figure 7.3b with fins side 2).

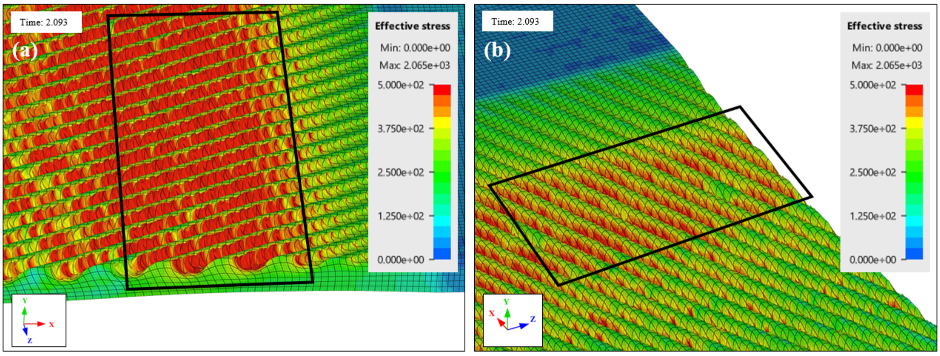

Figure 7.3: Finite Elements simulation results showing effective strain distribution on embossed strip surface: (a) 0° inclination view with respect to the rolling direction, and (b) 90° inclination view with respect to the rolling direction.

7.3.2 Microstructural characterization

Figure 7.4 shows details of the strip microstructure in BSE images. The micrograph in figure 7.4 shows intermetallic particles contained in the AA3xxx alloy. The EDS analysis presented in table 7.5 indicate that all particles can be described as Al_6(Fe,Mn,Cu) type, with varying Fe/Mn content ratios. Three groups of intermetallics can be distinguished based on Fe/Mn ratio: Group A - big (1.5–3.5 μm) and mostly equiaxed particles with a large Fe/Mn ratio (0.8), Group B - fine (0.1–1 μm) equiaxed particles having a smaller Fe/Mn ratio (0.2), and Group C - plate-like particles having lengths between 2 μm and 7 μm with a high aspect ratio and the smallest Fe/Mn ratio (0.1) (shown in fig. 7.4). Table 7.5 provides the chemical composition averaged over 16 particles in each group.

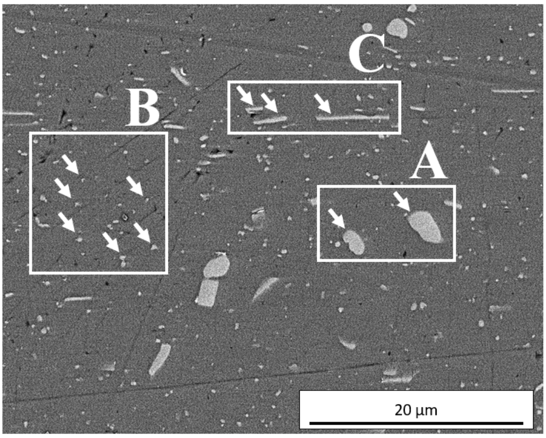

Figure 7.4: BSE image showing the different morphologies of intermetallic particles contained in the as-received AA3xxx alloy.

Table 7.5: Results of EDS analysis (in wt.%) of intermetallic particles sorted into groups A, B and C in the core (see fig. 7.4).

Element	**A**	**B**	**C**
O	1.8 ± 0.2	3.6 ± 0.3	2.3 ± 0.2
Al	84.9 ± 0.3	89.9 ± 0.2	92.3 ± 0.4
Mn	6.9 ± 0.2	4.8 ± 0.3	4.4 ± 0.2
Fe	5.5 ± 0.2	0.9 ± 0.1	0.4 ± 0.2
Cu	0.9 ± 0.1	0.8 ± 0.1	0.6 ± 0.3
Fe/Mn ratio	0.8	0.2	0.1

Figure 7.5 shows results from STEM EDS elemental mapping analysis, focused around the boundary of a grain from the AA3xxx alloy. Results indicate segregation of alloying elements such as Mn, Cu and Fe at the grain boundary. Mapping shows that the amount of iron is higher than Mn and Cu.

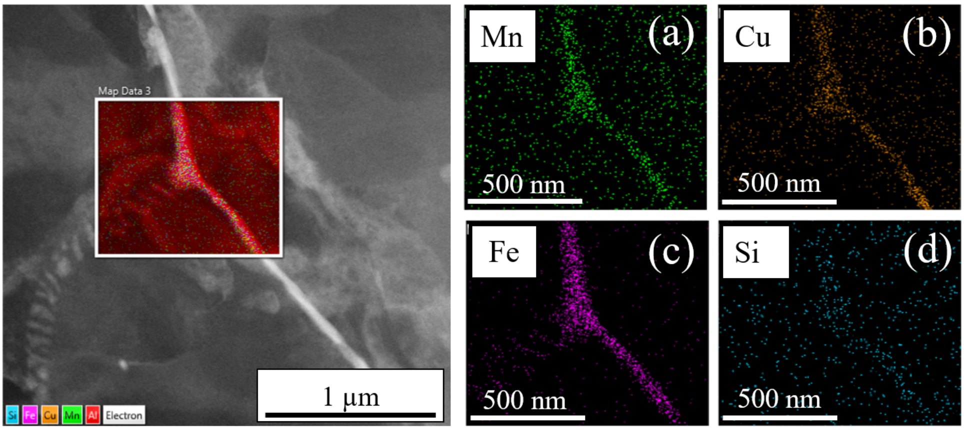

Figure 7.5: STEM High Angle Annular Dark Field (HAADF) micrograph of a grain boundary of the AA3xxx alloy, with EDS Al, Si, Fe, Cu and Mn elemental map overlay, and individual elemental maps for (a) Mn, (b) Cu, (c) Fe and (d) Si.

Table 7.6 shows chemical composition of the grain boundary, obtained by averaging measurements over 11 points along the grain boundary showed in figure 7.5. Measurements confirm grain boundary segregation of alloying elements.

Table 7.6: Results of EDS analysis (in wt.%) of grain boundary composition, in the AA3xxx alloy (see fig. 7.5).

Si	**Fe**	**Cu**	**Mn**	**Others**	**Al**
3.3 ± 0.1	9.7 ± 0.6	4.3 ± 0.4	2.9 ± 0.1	≤ 1.3	Balance

7.3.3 Differential Interference Contrast microscopy

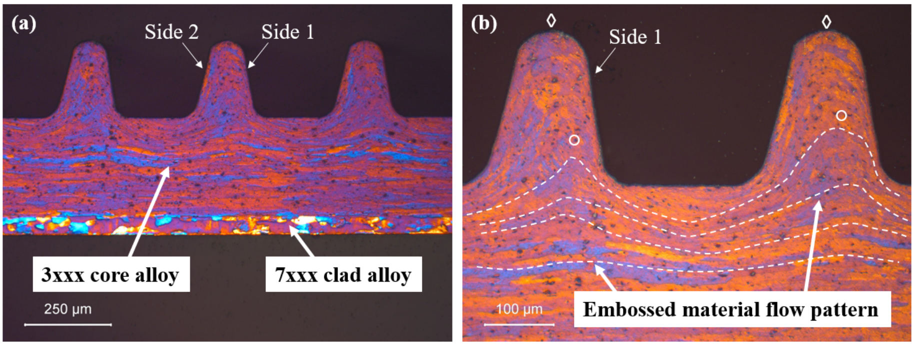

Figure 7.6: Low and high magnification differential interference contrast micrographs of the electro-polished embossed strip cross section, inspected with Lambda filter, highlighting the grain structure and embossed material deformation patterns.

Figure 7.6 shows the grain structure distribution over the embossed sample. Figure 7.6a shows an overview of the shape and distribution of grains in the clad, core, and embossed region (corresponding to the inner surface of the tube after complete forming), while figure 7.6b shows the magnified view highlighting the material flow pattern generated by the embossing process, as indicated using dotted white lines.
Similar to the results from the simulation, an asymmetry in the deformation and material flow with respect to the geometry of the fin is clearly evident in figure 7.6. The schematic of flow lines based on the grain flow distribution observed in the pictures in figure 7.6b clearly shows an offset with respect to the axes of symmetry of the embossed pattern (○) and material flow (◇). In particular, the material flow lines appeared to indicate a more severe deformation preferentially on one side of the fin (indicated as side 1). Like the simulation results, such unbalanced deformation level was consistent all along the strip length.

7.3.4 Potentiodynamic anodic polarization

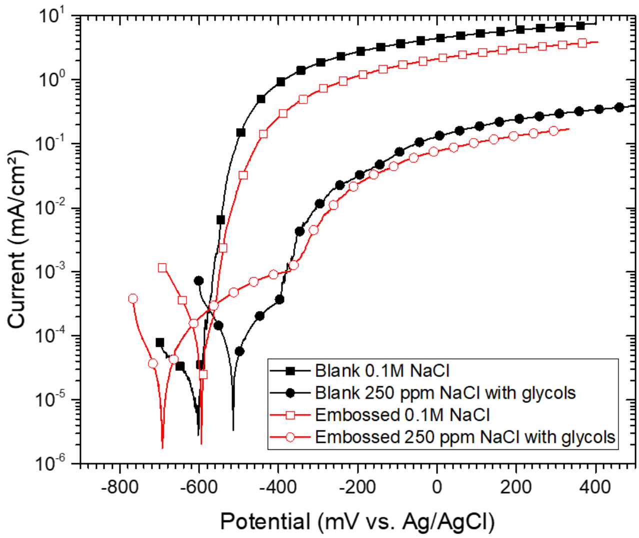

Figure 7.7: Potentiodynamic anodic polarization curves for blank strips and embossed strips obtained in 0.1M NaCl aqueous solution at neutral pH condition and in glycol-containing solution with addition of 250 ppm of NaCl.

Potentiodynamic anodic polarization curves for the blank and embossed material in 0.1M NaCl at neutral pH condition as well as in glycol-containing solution with 250 ppm NaCl addition are shown in figure 7.7. In the 0.1M NaCl solution, there is no appreciable effect of the embossing process on the corrosion potential of the surface. However, in glycol-containing solution, the corrosion potential of the embossed surface is more negative when compared to that observed for the embossed surfaces in the 0.1M NaCl containing solution. On the contrary, the corrosion potential of blank samples is less negative in glycol containing solution, when compared to that observed for the embossed surfaces in the 0.1M NaCl containing solution. The anodic current densities did not show major difference between the blank and embossed surfaces in 0.1M NaCl. However, polarization scans obtained in glycol showed passive behaviour both for the blank and embossed surfaces with higher passive current density for the embossed surface, while the breakdown potential (pitting potential) of both surfaces was similar.

7.3.5 Post polarization surface morphology

Figure 7.8a shows the SEM Secondary Electron (SE) micrographs of the blank (as-received) strip material (AA3xxx alloy surface) after the polarization experiment. Clearly the surface shows pitting distributed all over the surface with some alignment along the extrusion direction. Interior of the pitting showed crystallographic pitting morphology usually found for aluminium alloys.

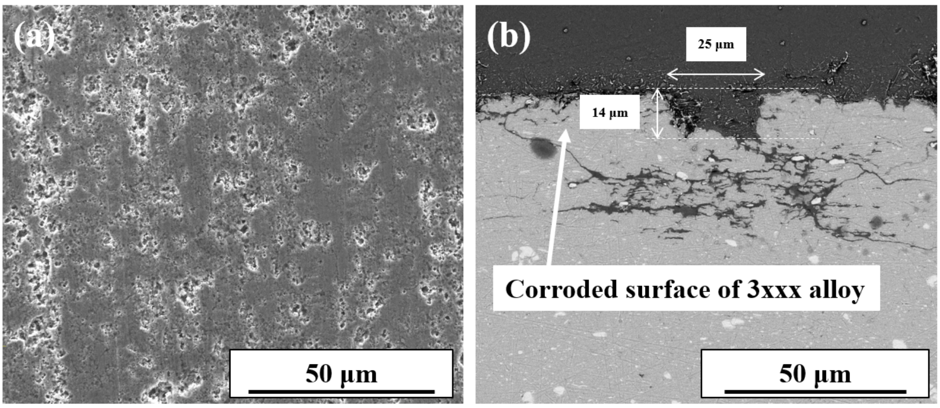

Figure 7.8: SEM micrographs of blank strip surface after subject to potentiodynamic anodic polzarization: (a) topographic view, in SE imaging mode, and (b) cross section view, in BSE imaging mode.

Figure 7.8b shows the BSE micrograph of the cross-section of the anodically polarized blank sample. Morphology reveals some inter granular corrosion (IGC) below the surface pits. Presence of intermetallic particles (brighter in contrast in back scattered imaging mode) of various size can be seen on the surface and along the inter granular (IG) dissolution development paths.
In figure 7.9, SEM SE micrographs show the surface topographic view of the embossed strip surface after being subjected to potentiodynamic anodic polarization. These surfaces showed a lower of degree of unifor-

mity in the developed pits on the surface compared to the blank strips after polarization.

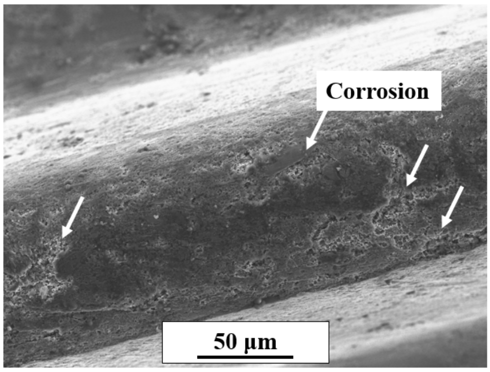

Figure 7.9: SEM SE image of embossed strip surface, topographic view of a single micro-fin, after potentiodynamic anodic polarization test showing dissolution of the surface due to pitting.

Figure 7.10 shows that cross-sectional view of the embossed surface after the polarization experiments. The dissolution of the surface of the embossed sample, especially the micro-fins displayed an anisotropy, and the depth and number density of the pits was far lower than that observed for the blank strips after polarization. The corrosion morphology resembled IGC and appeared to be mainly localized on one of the two sides of the fin (Figure 7.10a). This morphology was consistently present all over the surface area that was inspected in the SEM. Figure 7.10b and 7.10c highlight the two main sites where more corrosion was detected: at the top right side of the fin and bottom right corner of the same (orientation indications referring to picture showed in figure 7.10a).

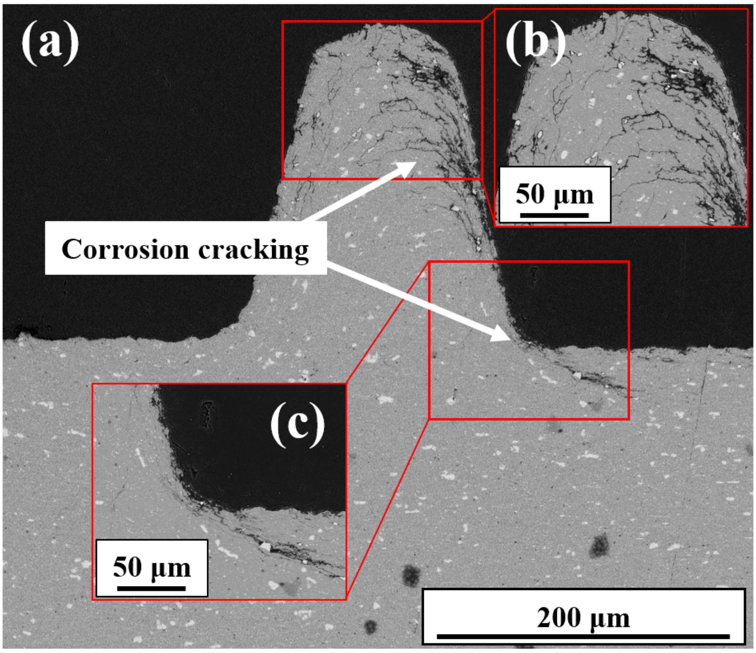

Figure 7.10: BSE images of corroded embossed strip, cross section after polarization test, single fin.

In order to investigate the state of corrosion on the sample over a larger area, X-ray computational tomography was employed. Figure 7.11 presents the results from the non-destructive inspection of embossed samples subjected to anodic polarization. Figure 7.11a presents a 3D overview of the strip, with corrosion features highlighted in dark blue, appearing at both the surface and within the fins. Corrosion features were found to be consistently present preferentially on one side in accordance with the previous observations.

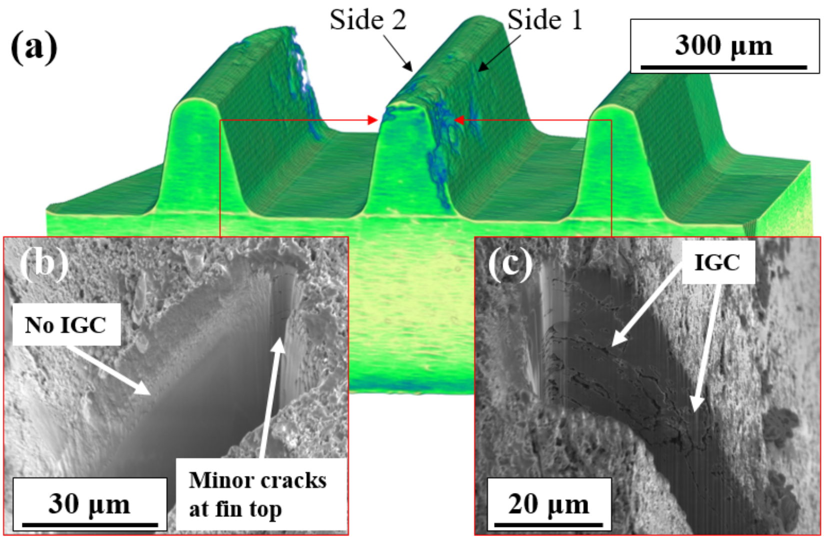

Figure 7.11: (a) X-ray micro computed tomography results for strip corroded in pH neutral, glycol-containing solution, with addition of 250 ppm NaCl contamination and SEM SE images of FIB cut on embossed fin of same sample: Detail of sub-surface IG corrosion development on "side 1" (c) and detail of non-attacked region, opposite to "side 1" (b).

Further, FIB cross-sectional analysis was carried out on both sides of the fins to confirm the observation as shown in figure 7.11b and 7.11c. In particular, the top corner of a fin was cut, as shown if figure 7.11b and 7.11c. The fin was cut on both the sides, at locations exactly opposite to each other, in respect to the fin plane of symmetry. Results confirmed the accuracy of previous analysis showing the IGC was preferentially present on one of the two sides of the fin (side 1, figure 7.11c). Opposite side (side 2, figure 7.11b) did not present any IGC, comparable in size and amount (only minor dissolution appearing at the fin top).

7.4 Discussion

Overall, the results presented in this paper indicate that the embossing process on the Al strip material has generated an anisotropic mi-

crostructure due to the difference in the material plastic flow leading to a difference in the electrochemical nature of the surface, which is observed from the analysis of the surfaces after potentiodynamic anodic polarization.
AA3xxx alloys are used along with an AA4xxx or an AA7xxx alloy cladding for heat exchanger applications. The AA4xxx and AA7xxx alloys provide the sacrificial anode protection to the underlying AA3xxx alloy, which provides the mechanical strength to the assembly. AA3xxx alloys are dispersoid strengthened, and the dispersoids present provide sites for galvanic corrosion to take place and act as sites for weakening the passive layer, promoting pitting corrosion initiation and IGC attack, by locally increasing cathodic activity of the material, thus increasing the corrosion rate [41][42][43][44]. SEM and STEM elemental analysis of the microstructure of the AA3xxx alloy used in present work showed presence of cathodic intermetallic particles and trace elements at grain boundaries, expected to locally alter the electrochemical nature of the alloy [45][46][47]. These justified the observed pitting followed by inter granular corrosion after potentiodynamic polarization of the blank samples.
The FEM simulations performed show that there is an anisotropy in the strain distribution in the AA3xxx core material during the embossing process, which has been clearly visualised in the differential interference contrast optical micrographs of the embossed surface cross-sections.
The differential interference contrast micrographs from the embossed fins also showed that the grains in the AA3xxx strip, especially in the fin regions are not equiaxed, but have a texture. The grains have a high aspect ratio with a length of $\sim$100 µm in the plane perpendicular to the forming direction. Material displacement flow lines exhibited a clear asymmetry with respect to the geometry of the fin, indicating anisotropic deformation of the embossed aluminium strip, in line with the results of FEM simulations. The effect of such grain size modification after the plastic deformation on the electrochemical nature has been investigated for high purity Al by Ralston et al [48]. It was reported that the corrosion rate tended to decrease with decreasing grain size and the corrosion potential increased with decreasing grain size, which was attributed to higher activity of the deformed surface which increases the passive film formation ability. However, in our case for

AA3xxx alloy, a slight decrease of the corrosion potential was observed, which could be attributed to it being a different alloy system as well as having a different grain size distribution on either side of the fins as well as on the bottom of the fins.
The optical micrographs, however, clearly show that the attack on the surface of the fins during anodic polarization is focused at the point where the metal has undergone the highest amount of deformation. Trdan et al. [49] have shown that during surface modification using laser shock peening, the residual compressive stresses are effective in hindering the propagation of IGC in AA6xxx alloys, but noted that pitting corrosion was present on untreated and treated surfaces. The state of residual stress is important in the resulting corrosion behaviour of the embossed surfaces due to the modification of the surface as well as the subsequent passivation capability of the surface [50][51]. Due to the anisotropic nature of the embossing process, it is expected that there is a difference in the residual stress state on either side of the fins on the surface of the AA3xxx strip material. However, the analysis of this is currently out of scope of this paper. What can be said is that in the regions of maximum plastic flow of the metal, the intermetallic particles tend to break up and create a higher number distribution on the surface thus providing more sites for corrosion and passive film breakdown [52]. Additionally, high levels of plastic surface strain on the AA3xxx alloy determined higher corrosion susceptibility of surface and sub-surface layer [10]. As a result, SEM inspection of potentiodynamic polarization tested embossed strips, showed that corrosion developed in the form of IGC on these sites.
Similar anisotropy in the material flow has been earlier shown for grooved Cu tubes manufactured using ball spin forming by Zhang et al. [53]. Through simulations and experimental investigations, results showed that the folding defects formed preferentially at rounded corners between the fins and at the bottom surface on one side, which is similar to our observations for the embossed AA3xxx surface. Further, microstructural observations showed that folding was formed by multi-track metal flow during the forming process. Li et al. conducted similar studies where it was shown that there is a skewness to the structure of the fins formed on the surface of Cu tubes and assigned this to the geometry of the mandrel [54].

The potentiodynamic anodic polarization revealed differences between the corrosion behaviour in NaCl and glycol-containing solution with 250 ppm NaCl contamination. Main difference was observed in the anodic reactivity in glycol-containing solution, which showed onset of passivation before breakdown. Such behaviour was attributed to the presence of the corrosion inhibitors AZ8104 and CorrShield OR4407 in the solution, both designed to provide protection to the metallic surface by establishment of passive inhibitor film. The reason why, in the case of a blank surface such anodic trend accompanied a corrosion potential increase, while reduced corrosion potential was showed by the embossed material, was addressed to the complex surface topology of the embossed sample disturbing the mentioned passive inhibitor film formation. The exact reason for this behaviour might require further investigation.
Tierce et al. [39][55] studied the effect of brazing cycle and the electrolyte composition along with temperature on the corrosion behaviour of AA3003 clad with AA4343 alloy, and results showed that the corrosion rate was highly depended on the glycol content. Corrosion rate decreased with increase in glycol content by lowering the corrosion current densities. However, presence of 350 ppm NaCl under neutral pH condition increased the corrosion. The corrosion behaviour of the material observed in this work from the anodic polarization is in agreement with the previous work.
The morphology of the corrosion surface of the of the embossed fins on the AA3xxx surface resembled typical intergranular corrosion for the specimens tested both in NaCl and glycol-containing, and the anisotropy was similar for both solutions.
Overall, the result from this investigation shows that the embossing process for obtaining the micro-fins on the inner surface of the AA3xxx heat exchanger tube material has led to increased susceptibility of IGC for this alloy, especially on one side of the micro-fins. This is attributed to the anisotropic plastic flow and higher deformation degree in the metal, which is inherent to the adopted embossing process. Microstructurally, segregation of alloying element along the grain boundary caused intergranular corrosion. Present work highlighted how the embossing process, designed to develop complex surface patterns on the surface of an aluminium strip produce deformation and microstructural changes,

which leads to corrosion problems.

7.5 Conclusion

The microstructure and corrosion behaviour of blank and embossed strips of a 3xxx aluminium alloy were investigated. Based on this investigation, the following conclusions are obtained.

1. Microstructure of the alloy showed segregation of alloying elements along the grain boundaries and presence of Fe/Mn intermetallic particles of various sizes and morphology.

2. The embossing process generated an anisotropic microstructure in the samples, characterized by unevenly distributed formation of near–surface deformed regions.

3. Such localized regions of higher plastic deformation were found to be generated by differences in the material plastic flow, during the cold forming of the aluminium strips.

4. Analysis of embossed strip samples, after artificially induced corrosion attack, revealed the presence of sites with increased IGC susceptibility, distributed as a function of the embossed pattern geometry and corresponding to those zones of higher plastic deformation observed on one side of the fins.

Acknowledgements

The authors would like to thank Norsk Hydro and Innovation Fund Denmark (grant 5189-00144B) for their technical and financial support of the project. We also thank Mr. A. Mangelsdorf, Dr. M. Pasqualon and Mr. T. Guillaume from Norsk Hydro for their support. The 3D Imaging Centre at the Technical University of Denmark is gratefully acknowledged. Dr. C. Gundlach is grateful for financial support from Innovation Fund Denmark via grant 5152-00005B.

Bibliography

[1] T. Ebisu,"Evaporation and Condensation Heat Transfer Enhancement for Alternative Refrigerants Used in Air-Conditioning Machines" in Heat Transfer Enhancement of Heat Exchangers, Kluwer Academic Publishers (1999) 579-600.

[2] R. Kaji et al.," The Effect of Inner Grooved Tubes on the Heat Transfer Performace of Air-Cooled Heat Exchangers for CO2 Heat Pump System" International Refrigeration and Air Conditioning Conference, paper 1268 (2012).

[3] S.S. Kale et al, Int. Journal of Engineering Research and Applications ISSN: 2248-9622, Vol. 4, Issue 9, Version 6, (September 2014) 154-158.

[4] M. Houfuku, Development trends in inner-grooved tubes in Japan, Hitachi Cable Review No.26 (August 2007) 1–3.

[5] R.K. Nichols, PE, H.N. Udall, High frequency welding of aluminum. A Thermatool Corp. Publication, T.P. n. 111, Rev. 2. March 1999.

[6] D. Zhou, X. Chengdong, J. Lv, L. Li, inventors; Yinbang Clad Material Co., LTD, assignee. Aluminum alloy composite strip for internal threaded heat exchange tube and manufacturing therefor. World Intellectual Property Organization Patent WO 2018049585 A1. Mar 22 2018.

[7] G.L. Zhang, S.H. Zhang, B. Li, H.Q. Zhang, Analysis on folding defects of inner grooved copper tubes during ball spin forming. J. Mater. Process. Technol. 184 (2007) 393–400.

[8] Y. Li, Z. Xu, Y. Tang, Z. Zeng, Forming characteristics analysis of the cross-section of axially inner grooved copper tube. Int. J. Adv. Manuf. Technol. 47 (2010) 1023–1031.

[9] X. Zhou, Y. Liu, G.E. Thompson, G.M. Scamans, P. Skeldon, J.A. Hunter, Near-Surface Deformed Layers on Rolled Aluminum Alloys, Metall. Mater. Trans. A. 42 (2011) 1373–1385.

[10] G.M. Scamans, M.F. Frolish, W.M. Rainforth, Z. Zhou, Y. Liu, X. Zhou, et al., The ubiquitous Beilby layer on aluminium surfaces, Surf. Interface Anal. 42 (2010) 175–179.

[11] S.G.T. Beilby, Aggregation and Flow of Solids: Being the Records of an Experimental Study of the Micro-structure and Physical Properties of Solids in Various States of Aggregation, Macmillan and Company, limited (1921) 1900-1921.

[12] O.A. Gali, M. Shafiei, J.A. Hunter, A.R. Riahi, The characterization of near-surface defects evolved on aluminum–manganese alloys during hot rolling, Surf. Interface Anal. 48 (2016) 877–888.

[13] G. Buytaert, H. Terryn, S. Van Gils, B. Kernig, B. Grzemba, M. Mertens, Investigation of the (sub) surface of commercially pure rolled aluminium alloys by means of total reflectance, r.f. GDOES, SEM/EDX and FIB/TEM analysis, Surf. Interface Anal. 38 (2006) 272–276.

[14] A. Afseth, J.H. Nordlien, G.M. Scamans, K. Nisancioglu, Effect of thermo-mechanical processing on filiform corrosion of aluminium alloy AA3005, Corros. Sci. 44 (2002) 2491–2506.

[15] R. Ambat, A.J. Davenport, A. Afseth, G. Scamans, Electrochemical Behavior of the Active Surface Layer on Rolled Aluminum Alloy Sheet, J. Electrochem. Soc. 151 (2004) B53–B58.

[16] G. Buytaert, Premendra, J.H.W. de Wit, L. Katgerman, B. Kernig, H.J. Brinkman, et al., Electrochemical investigation of rolled-in subsurface layers in commercially pure aluminium alloys with the microcapillary cell technique, Surf. Coatings Technol. 201 (2007) 4553–4560.

[17] Premendra, B.S. Tanem, J.M.C. Mol, H. Terryn, J.H.W. DeWit, L. Katgerman, A combined TEM and SKPFM investigation of the surface layers on rolled AA5050 aluminium alloy using ultra-microtomy, Surf. Interface Anal. 40 (2008) 1157–1163.

[18] S. Feliu, M.J. Bartolomé, Influence of alloying elements and etching treatment on the passivating films formed on aluminium alloys, Surf. Interface Anal. 39 (2007) 304–316.

[19] G.G.B. Zaffaroni, V.C. Gudla, R. Ud Din, R. Ambat, Characterization of blisters on powder coated aluminium AA5006 architectural profiles. Eng. Fail. Anal. 103 (2019) 347–360.

[20] X. Zhou, G.E. Thompson, G.M. Scamans, The influence of surface treatment on filiform corrosion resistance of painted aluminium alloy sheet. Corros. Sci. 45 (2003) 1767–1777.

[21] A. Afseth, J.H. Nordlien, G.M. Scamans, K. Nisancioglu, Effect of thermo-mechanical processing on filiform corrosion of aluminium alloy AA3005. Corros. Sci. 44 (2002) 2491–2506.

[22] J. Tan et al., On the microstructural and electrochemical nature of hydrothermally treated Al-Zr and Al-Ti surfaces. Corros. Sci. (2019)

[23] Y. Ma et al., Localised corrosion in AA 2099-T83 aluminium-lithium alloy: The role of grain orientation. Corros. Sci. 107 (2015) 41–48.

[24] V.C. Gudla et al., Initiation and short crack growth behaviour of environmentally induced cracks in AA5083 H131 investigated across time and length scales. Corros. Rev. 37 (2019) 469–481.

[25] W. Gao, D. Wang, M. Seifi, J.J. Lewandowski, Anisotropy of corrosion and environmental cracking in AA5083-H128 Al-Mg alloy. Mater. Sci. Eng. A 730 (2018) 367–379.

[26] K. Bordo, V.C. Gudla, L. Peguet, A. Afseth, R. Ambat, Electrochemical profiling of multi-clad aluminium sheets used in automotive heat exchangers. Corros. Sci. 131 (2018) 28–37.

[27] H. Zhao, R. Woods, 10 - Controlled atmosphere brazing of aluminum A2 - D.P. Sekulić, in Advances in Brazing, ed. Sekulić, D. P. B. T.-A. in B., Woodhead Publishing (2013) 280-323e.

[28] F.N. Afshar, J.H.W. De Wit, H. Terryn, J.M.C. Mol, The effect of brazing process on microstructure evolution and corrosion performance of a modified AA4XXX/AA3XXX brazing sheet. Corros. Sci. 58 (2012) 242–250.

[29] F.N. Afshar, J.H.W. De Wit, H. Terryn, J.M.C. Mol, Scanning Kelvin probe force microscopy as a means of predicting the electrochemical characteristics of the surface of a modified AA4xxx/AA3xxx (Al alloys) brazing sheet. Electrochim. Acta 88 (2013) 330–339.

[30] B. Ren, inventor; Arconic Inc., assignee. Multi-layer aluminum alloy sheet product for tubes for heat exchangers. United States Patent US 9964364 B2. Mar 08 2018.

[31] J.A. Olivier, L. Liebenberg, J.R. Thome, Heat transfer, pressure drop, and flow pattern recognition during condensation inside smooth, helical micro-fin, and herringbone tubes, Int. J. Refrig. 30 (2007) 609–623.

[32] A. Hone, E.C. Pearson, Metal Progr. 53 (1948) 363–366.

[33] V.C. Gudla, K. Rechendorff, Z.I. Balogh, T. Kasama, R. Ambat, In-situ TEM investigation of microstructural evolution in magnetron sputtered Al-Zr and Al-Zr-Si coatings during heat treatment, Mater. Des. 89 (2016) 1071–1078.

[34] K. Bordo, V.C. Gudla, L. Peguet, A. Afseth, R. Ambat, Electrochemical profiling of multi-clad aluminium sheets used in automotive heat exchangers, Corros. Sci. 131 (2018) 28–37.

[35] S.T. Abrahami, J.M.M. de Kok, V.C. Gudla, R. Ambat, H. Terryn, J.M.C. Mol, Interface strength and degradation of adhesively bonded porous aluminum oxides, Npj Mater. Degrad. 1, 8 (2017) 1-8

[36] S.T. Abrahami, J.M.M.M. de Kok, V.C. Gudla, K. Marcoen, T. Hauffman, R. Ambat, J.M.C. Mol, H. Terryn, , Fluoride-induced interfacial adhesion loss of nanoporous anodic aluminium oxide templates in aerospace structures, ACS Appl. Nano Mater. 1 (2018) 6139–6149.

[37] L.A. Feldkamp, L.C. Davis, J.W. Kress, Practical cone beam algorithm, J. Opt. Soc. Am. A 1 (1984) 612-619.

[38] ASTM International, D1384-01 Standard Test Method for Corrosion Test for Engine Coolants in Glassware. West Conshohocken, PA; ASTM International (2001).

[39] S. Tierce et al., Corrosion behaviour of brazed multilayer material AA4343/AA3003/AA4343: Influence of coolant parameters. Corros. Sci. 49 (2007) 4581–4593.

[40] R. Qvarfort, New electrochemical cell for pitting corrosion testing, Corros. Sci., 28 (1988).

[41] R. Ambat, A.J. Davenport, G.M. Scamans, A. Afseth, Effect of iron-containing intermetallic particles on the corrosion behaviour of aluminium, Corros. Sci. 48 (2006) 3455–3471.

[42] N. Birbilis, R.G. Buchheit, Electrochemical Characteristics of Intermetallic Phases in Aluminum Alloys: An Experimental Survey and Discussion, J. Electrochem. Soc. 152 (2005) B140–B151.

[43] A.J. Davenport, Y. Yuan, R. Ambat, B.J. Connolly, M. Strangwood, A. Afseth, et al., Intergranular Corrosion and Stress Corrosion Cracking of Sensitised AA5182, Mater. Sci. Forum. 519–521 (2006) 641–646.

[44] R.U. Din, S. Valgarsson, M.S. Jellesen, H.J. Eriksen, U. Praastrup, P. Møller, et al., Corrosion issues of powder coated AA6060 aluminium profiles, Eng. Fail. Anal. 47 (2015) 16–24.

[45] K. Shimizu, K. Nisancioglu, High Resolution SEM Investigation of Intercrystalline Corrosion on 6000-Series Aluminum Alloy with Low Copper Content, ECS Electrochemistry Letters, 3 (9), (2014) C29-C31.

[46] M.H. Larsen, J.C. Walmsley, O. Lunder, R.H. Mathiesen, K. Nisancioglu, Intergranular corrosion of copper-containing AA6xxx AlMgSi aluminum alloys, Journal of the Electrochemical Society, Volume 155, Issue 11 (2008) C550-C556.

[47] M.H. Larsen, J.C. Walmsley, O. Lunder, R.H. Mathiesen, K. Nisancioglu, Effect of excess silicon and small copper content on intergranular corrosion of 6000-series aluminum alloys, Journal of the Electrochemical Society, Volume 157, Issue 2 (2010) C61-C68.

[48] K.D. Ralston, D. Fabijanic, N. Birbilis, Effect of grain size on corrosion of high purity aluminium, in Electrochimica Acta vol. 56 (2011) 1729–1736.

[49] U. Trdan, J. Grum, SEM/EDS characterization of laser shock peening effect on localized corrosion of Al alloy in a near natural chloride environment. Corros. Sci. 82 (2014) 328–338.

[50] M. Abdulstaar, M. Mhaede, L. Wagner, M. Wollmann, Corrosion behaviour of Al 1050 severely deformed by rotary swaging. Mater. Des. 57 (2014) 325–329.

[51] U. Trdan, J. Grum, J.A. Porro, J.L. Ocaña, Analysis of residual stress and corrosion resistance of laser shock-processed 6012 and 6082 aluminium alloys. in XVII International Symposium on Gas Flow, Chemical Lasers, and High-Power Lasers vol. 7131 713124 (SPIE, 2008).

[52] G. Wang, H.S. Jiao, Microstructural effects in corrosion of aluminium tube alloys. Trans. Nonferrous Met. Soc. China, English Ed. 21 (2011) 1193–1198.

[53] G.L. Zhang, S.H. Zhang, B. Li, H.Q. Zhang, Analysis on folding defects of inner grooved copper tubes during ball spin forming. J. Mater. Process. Technol. 184 (2007) 393–400.

[54] Y. Li, Z. Xu, Y. Tang, Z. Zeng, Forming characteristics analysis of the cross-section of axially inner grooved copper tube. Int. J. Adv. Manuf. Technol. 47 (2010) 1023–1031.

[55] S. Tierce et al., Corrosion behaviour of brazing material AA4343. Electrochim. Acta 52 (2006) 1092–1100.

8 Tubes Corrosion

Full title:

Corrosion Behaviour of High Frequency Welded Aluminium Micro-fin Tubes for Heat Exchangers

Authors:

G.G.B. Zaffaroni[1], V. C. Gudla[2], R. Rizzo[1], J.H. Nordlien[3], R. Ambat[1]

[1] Department of Mechanical Engineering, Technical University of Denmark, DK 2800 Kgs. Lyngby, Denmark;
[2] Henry Moseley X-ray Imaging Facility, Department of Materials, University of Manchester, M13 9PL Manchester, United Kingdom;
[3] Innovation & Technology - Precision Tubing, Hydro Aluminium, Extruded Solutions, Hydrovegen 160 4265, Håvik, Norway

Abstract

Corrosion behaviour of high frequency welded aluminium micro-fin tubes for heat exchanger applications has been investigated in this work. A bi-layered strip with an AA3xxx aluminium alloy as core material and additional 10% cladding of AA7xxx aluminium alloy on one side was the material used for investigation. Relation between the microstructure and corrosion behaviour is investigated in acidic, neutral, and highly alkaline conditions. Corrosion investigations were carried out using potentiodynamic anodic polarization tests, Zero Resistance Ammetry (ZRA) measurements, Acidified Synthetic Sea Water Testing (SWAAT), and full immersion in highly alkaline solutions. Microstructure and morphological characterization were carried out using scanning electron microscopy and energy dispersive X-ray spectroscopy (SEM-EDS), focused ion beam microscopy (FIB-SEM), and scanning transmission electron microscopy (STEM-EDS). The AA7xxx alloy surface protects the AA3xxx alloy sacrificially in acidic and neutral environment while catastrophic corrosion of AA3xxx core alloy is observed in highly alkaline solutions due to passivation of the sacrificial AA7xxx alloy.

8.1 Introduction

Aluminium alloys are increasingly being used in the Heat Ventilation Air Conditioning and Refrigeration (HVAC&R) market owing to their ease of formability, good thermal conductivity, passivating nature, and ease of recycling [1][2][3][4]. In particular, aluminium is nowadays extensively used in the manufacturing of heat exchangers and other internal electrical wiring for automobiles and is gradually substituting the traditionally employed Copper [5][6]. Today, the HVAC&R industry growth is driven by the need for energy-efficient devices [7] and hence Aluminium micro-fin tubes characterized by different inner tube surface patterns are finding increased interest [8].
Micro-fin tubes have shown outstanding performance in enhancing heat transfer, for both evaporation and condensation processes, without compromising on other aspects of the products. For this reason, they are widely used, especially in the air conditioning and refrigeration industries. For these applications, the improved performance overcomes the

drawback of higher manufacturing related costs arising from increased complexity of the processing of such tubes [9][10].
In recent years, increasingly complex patterns such as non-axial symmetric patterns (i.e. Herringbone and Helical cross-grooved patterns) have been developed, which are manufactured using techniques different from the conventional processes that were developed and tested in the 1970s for helical patterned tubes obtained through extrusion. Manufacturing of the patterned tubes involves use of a grooved mandrel, inserted inside the tube and connected by a tie rod to a floating plug. This is then fixed by a drawing die, reducing the diameter of the tube, whose inner surface is then grooved by the rotating mandrel [8]. However, the manufacturing process of the most recent generations of heat exchanger tubes with non-symmetric inner surface patterns comprises of: (i) Embossing of the inner surface of an aluminium alloy sheet, followed by (ii) tube forming and subsequent high frequency welding. The primary stage of embossing consists of a thread cold rolling of a flat aluminium strip surface that corresponds to the inner surface of the finished tube [11]. The second main stage consists of high frequency (HF) welding of the as-embossed aluminium strips after they are longitudinally cold formed into a nearly closed tube geometry [12][13][14] (see figure 8.1). This is usually followed by a scarfing process with a knife along the outer high frequency weld line to remove the flash formed due to the welding process. However, as the scarfing process locally removes the outer sacrificial clad layer along the HF weld line, it risks the exposure of the core AA3xxx material to the external service environment. This region of exposed core alloy along the weld line surface is termed as "devoid of clad area", which has been observed at the outer surface of finished HF welded tubes by means of SEM analysis [15] and is also schematically represented in figure 8.2a and 8.2b. Consequently, the corrosion behaviour of these welded tubes is altered as the outer AA7xxx clad layer that is expected to provide sacrificial protection to inner high strength AA3xxx alloy has been locally destroyed. In view of this, it is necessary to understand the modifications in the electrochemical and corrosion behaviour of such HF welded tubes where the scarfing process exposes the AA3xxx core alloy.

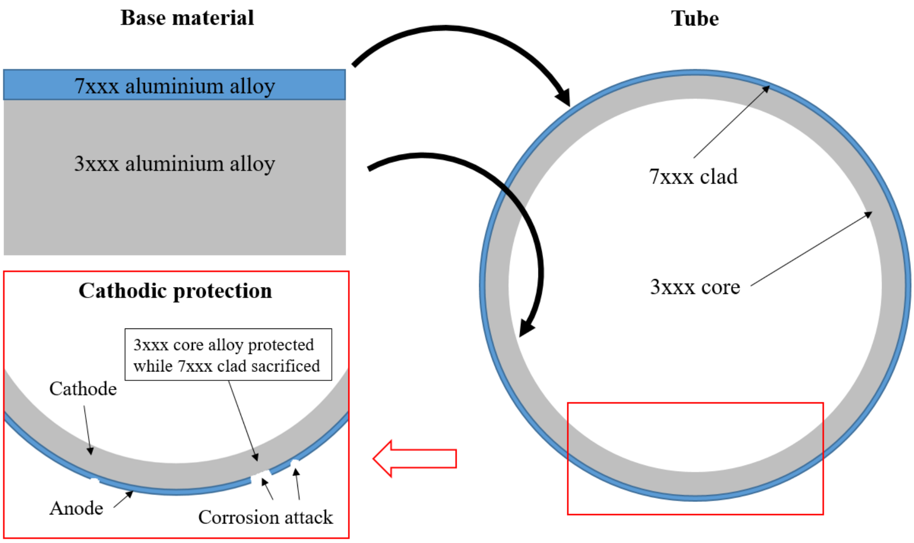

Figure 8.1: Schematic representation of material combination in both strip and tube forms, with sacrificial protection function of the clad schematically presented.

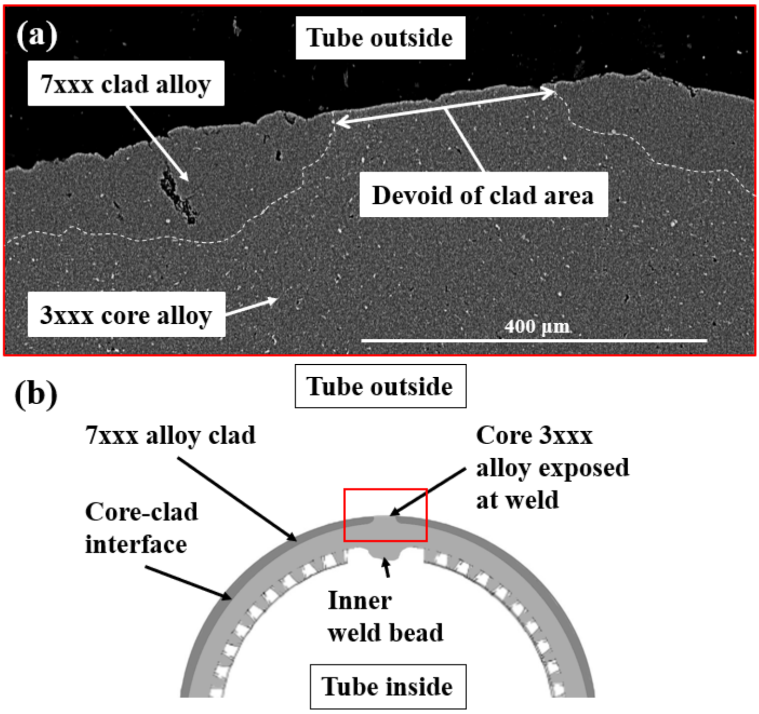

Figure 8.2: (a) Back scatter electron image of the weld line cross section, highlighting AA3xxx core alloy, AA7xxx clad alloy, and devoid of clad area; (b) schematic representation of devoid of clad area location, with respect to the tube geometry, with detail showed in (a) highlighted with red square.

Aluminium alloys used in the automotive industry as well as the HVAC&R industry are designed to perform under both acidic and alkaline corrosive atmospheres generally arising from the environmental Cl^- contaminations as well high pH alkaline detergents [16][17]. However, the kinetics of aluminium dissolution vary considerably between exposure to acidic or alkaline aqueous media and if Cl^- ions are present. Exposure to alkaline solution causes increased dissolution of Al, while dissolution in an acidic solution, depends on the nature and concentration of anions, pH of the media, and temperature [18][19][20]. For Aluminium based heat exchangers, the assembly is prone to atmospheric corrosion in the presence of Cl^-, and occasional alkaline corrosion due

to exposure to reagents in typical washing detergents. Protection strategies involve use of Zn diffusion layers on the Mn and Cu alloyed Al tube materials, along with a sacrificial Zn alloyed Al micro-fin material that would protect the corrosion of the tube [21][22][23][24]. Melander et al. have studied field retrieved brazed Aluminium radiators from car and found that the Zn containing micro-fins corroded preferentially and protected the tube materials [25]. Alternative approaches involve the use of intermediate sandwich layers containing low Cu between the core alloy and the top sacrificial layer which increases the corrosion potential with depth after brazing due to inter-diffusion of the species [26]. Shi et al. used an AA7072 alloy layer that was sandwiched between an AA3xxx core and an AA4xxx brazing filler layer. The electrochemical studies performed according to ASTM G69-97 showed that the Zn-containing sandwich layer provided sacrificial protection for the core and the brazing filler before and after brazing treatment [24]. The AA7072 layer displayed a lower corrosion potential when compared to the other material used in the brazing sheet and displayed an increase of 40 mV in the open circuit potential after being subject to brazing, which was still lower compared to other materials in the brazing sheet.
In this work, we present an investigation on the alkaline corrosion behaviour of the outer surfaces of such HF welded aluminium tubes with AA7xxx cladding, having the surface morphology described above (figure 8.2). The heat exchanger tubes with the outer clad and the inner core were manufactured by High Frequency (HF) welding process [12][13], details of which have been reported elsewhere [14] in addition to the effect of HF welding on the microstructure [15]. The relationship between the localized structural changes occurring along the HF weld area was investigated with a focus on the geometrical changes during welding, microstructure modifications, and their effect on the corrosion behaviour. Acidic, neutral, and alkaline environmental conditions that constitute the typical environment for corrosion of aluminium alloys in HVAC&R and automotive industry have been investigated [27]. Special focus was on the corrosion behaviour of the outer surface of the HF welded tubes having a devoid of clad area along the weld line. Techniques such as potentiodynamic anodic polarization, Zero Resistance Ammetry (ZRA), and immersion testing were employed, the results were benchmarked with Acidified Synthetic Sea Water Testing

(SWAAT), and the observations were correlated to the microstructural changes for the tube during manufacturing.

8.2 Materials and methods

8.2.1 Materials

Aluminium strips used in present investigation consist of AA3xxx series core with an AA7xxx sacrificial cladding on one side (10% of thickness) in "O" temper (as shown in figure 8.1). Chemical composition of the materials used is shown in table 8.1. The strips were obtained with micro-fins embossed on the AA3xxx side which is corresponding to the inner side of the tube once formed and welded. Manufacturing of the clad strips involved the core and clad alloy being joined through a hot rolling process, such that the two sheets are metallurgically bonded together, prior to the strips being cut to the desired dimensions [28].

Table 8.1: Main alloying elements (in wt.%) of the core and clad aluminium alloys.

Alloy	**Si**	**Fe**	**Cu**	**Mn**	**Mg**	**Zn**	**Ti**	Al
AA3xxx	≤0.25	≤0.4	0.5-0.6	1.0-1.3	≤0.05	≤0.1	0.1-0.2	Balance
AA7xxx	≤0.7	≤0.7	0-0.1	0-0.1	≤0.1	0.8-1.3	-	Balance

8.2.2 Samples preparation

For the electrochemical measurements on the different aluminium alloys, strip samples were manually cut, washed with a neutral soap solution, rinsed in deionized water and finally dried after ethanol rinsing.
Scanning electron microscopy was carried out on the cross sections of the samples that were hand cut. Metallographic preparation was performed by moulding in a Struers SpeciFix-20^{TM} epoxy and room temperature cured. The moulded samples were then subjected to mechanical grinding using silicon carbide polishing papers, subsequently from 220 grit to 4000 grit, with intermediate ethanol rinsing between each step. Fine polishing of the surfaces was performed subsequently using a 3 µm, 1 µm, and a $\frac{1}{4}$ µm diamond suspension with intermediate ethanol rinsing, and finally dried using warm air. The entire mechanical polishing

was carried out using ethanol (99.99% purity) as a lubricant in order to prevent any dissolution and loss of corrosion products by water-based preparation methods.
Samples for Acidified Synthetic Sea Water Testing (SWAAT) and the full immersion tests in alkaline electrolyte were the finished HF welded tube samples, cut to similar lengths (respectively 30 cm and 6 cm), washed with neutral soap, rinsed and finally dried after ethanol rinsing. The open ends of the tubes were shielded with masking tape to avoid undesired edge effects that would disturb the corrosion process, and to avoid access for the electrolyte to the inner surface of the tube.
On the surface of the samples used for the SWAAT tests, the formed corrosion products from the testing were removed prior to characterization. This was performed by immersing the tested samples in 70% HNO_3 and using ultrasonic bath for 6 min. Following this, the samples were rinsed with deionized water before ethanol rinsing and drying.

8.2.3 Electrochemical measurements

The strip test coupons from the clad Aluminium alloy sheet were investigated by potentiodynamic anodic polarization in a 3.5 wt.% aqueous NaCl solution under neutral pH and alkaline pH 12.5 (pH adjusted by the addition of NaOH). All electrochemical experiments were carried out using ACM GillAC potentiostat using a flat cell setup with a KCl saturated Silver/Silver Chloride (Ag/AgCl) as a reference electrode, and a platinum wire as the counter electrode. The measurements were performed on an area of 1 cm^2 exposed to 400 mL of the electrolyte. Anodic polarization scans were performed after a cell settle time of 1800 s, with a scan rate of 30 mV/s.
Zero resistance ammetry measurements were performed on AA3xxx surfaces coupled to AA7xxx flat strip test coupons. For tests, a flat cell (Gamry Paracell (V0.5 L)) with provision of exposing two specimens facing each other on both side of the cell was used. The two aluminium coupons connected as working electrodes (exposed area for each coupon: 2.6 cm^2) with a solution volume of 400 mL. The reference electrode was connected using a salt bridge and positioned close to the exposed surface of the AA3xxx alloy. The electrolyte used was a pH 12.5, 3.5 wt.% aqueous NaCl solution. The measurements were conducted at

room temperature for 4 h with the aim of determining the evolution of the galvanic current density between the two alloys. Distance between working electrodes was 14 cm. All experiments were repeated 3 times for consistency.

8.2.4 Acidified Synthetic Sea Water Testing

Acidified Synthetic Sea Water Testing (SWAAT) is the most common way in industry to measure the corrosion resistance of materials intended for heat exchanger applications [29][30]. This accelerated corrosion testing was selected in order to establish a benchmarking for comparing high pH corrosion vs. standard acidic environment corrosion behaviour.

The test was carried out according to ASTM standard G85 annex A3 "Acidified Synthetic Sea Water Testing (SWAAT Test)" [31] using an Ascott 7 (CC200iP) chamber. Solution pH range was between 2.82-2.92, chamber temperature of 49 °C, humidifier temperature of 57 °C, air pressure of 1.4 bar, and electrolyte density 1.024-1.026 g/cm^3. Samples were place in horizontal orientation with weld line pointing upwards. Tube samples were tested for possible leaks at the end of the test after rinsing with tap water using a pressure of 2 bar.

8.2.5 Customized immersion tests

In order to properly test and investigate the corrosion behaviour of the above-described finished tube samples in alkaline to strongly alkaline conditions, a customized immersion testing experimental setup was designed and built. It was, in particular decided to build an immersion bath, where tube samples could be completely immersed in the corrosive environment caused by stagnant solutions of pH 12.5, containing chlorides, in order to accelerate the process and simulate common salt contaminations, which is typical of outdoor and industrial environments. Plexiglas containers were used for this and each of them was filled with 2 L of 3.5 wt.% aqueous NaCl solution and pH levels regulated to target pH 12.5 through NaOH addition.

In each bath, tube samples were immersed in horizontal position and constantly kept more than 1 mm below solution surface and 2 cm above the bottom of the bath. All tubes presented same exact amount of exposed outer surface and were positioned at minimum 2 cm of horizontal distance between each other and the bath walls. All tubes were oriented in same direction with weld line on top. Temperature was maintained constant 22 °C. Tested samples were removed in pairs after different immersion times (schematic of the setup is provided in figure 8.3).

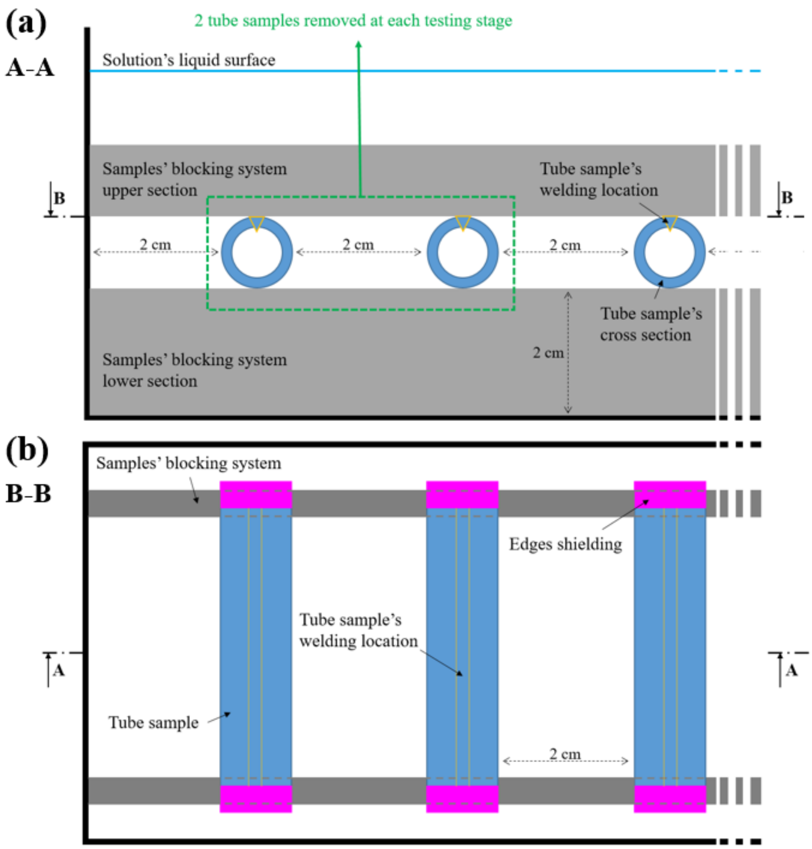

Figure 8.3: Schematic representation of immersion test setup from: (a) side view, section A-A and (b) topographic view, section B-B.

8.2.6 Microstructural characterization

Scanning electron microscopy was employed for the characterization of the material before and after the corrosion testing. Energy dispersive

X-ray spectroscopy was performed for obtaining the elemental analysis from the regions of interest. A scanning electron microscope model FEI Quanta 200^{TM} ESEM FEG equipped with an energy dispersive spectrometer (EDS) (Oxford Instruments 80mm^2 X-Max^{TM} coupled with an Aztec^{TM} SEM-EDS software) was used for the analysis. In-situ sectioning and imaging of the regions of interest was performed using a FEI Helios Nanolab^{TM} Dual beam FIB-SEM. Scanning transmission electron microscopy was performed on the samples prepared from the regions of interest using a FEI Tecnai^{TM} T20 G2 operating at 200 keV. EDS analysis and mapping were performed in the TEM using scanning TEM mode and data were collected using an Oxford Instruments 80mm^2 X-Max^{TM} detector coupled to an Aztec^{TM} TEM-EDS analysis software. Thin film lamella from the region of interest for the TEM analysis was prepared using site specific in-situ lift out technique using FIB milling, and the in-situ lift out of the thin film lamella was performed using an Omniprobe^{TM} micromanipulator coupled to the FIB-SEM [32][33][34][35]. The thin film sample that was lift out, was further thinned down to approx. 120 nm thickness for electron transparency and was milled with a low energy Ga ion beam (1 keV) to remove any prior high-energy milling induced artefacts. Mounting of the thin film lamella was performed onto Cu TEM sample grids with the help of in-situ Pt deposition to weld the sample to the grid.

8.3 Results

8.3.1 Electrochemical measurements

8.3.1.1 Potentiodynamic polarization

Figure 8.4 shows results of the open circuit potential (OCP) evolution as a function of time and potentiodynamic anodic polarization curves for the AA3xxx core, and AA7xxx clad materials in 3.5 wt.% aqueous NaCl solution at neutral pH value. The OCP evolution curve shows that the potential difference between the core and clad was ∼90 mV with the clad showing more active potential. Concerning potentiodynamic anodic polarization, both materials showed no major differences in the evolution of the anodic current density with the applied polarization potential. Both materials showed a steep increase in the anodic current density when polarized just above the Ecorr value (which was lower for the AA7xxx clad) and showed a saturation in the anodic current density value at higher potential values of > -200 mV vs Ag/AgCl.

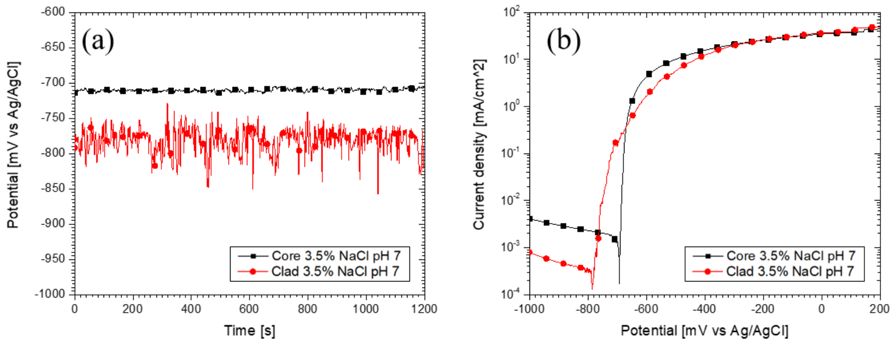

Figure 8.4: Electrochemical behaviour in pH neutral, 3.5 wt.% aqueous NaCl solution for core and clad material: (a) open circuit potential vs time and (b) anodic polarization curves for both materials.

Figure 8.5 shows results of open circuit potential (OCP) and potentiodynamic anodic polarization for the core and clad materials in 3.5% NaCl at pH 12.5. Throughout the OCP measurements, clad material showed more active potential (anodic) with a difference of ~100 mV. However, for both the materials, the initial OCP value was lower than that observed at the end of the test. Potentiodynamic anodic polarization curves for both the materials showed a passivation region followed by a breakdown. The AA7xxx clad surface showed a passive region between potential values of -1200 mV and -800 mV vs. Ag/AgCl, while the AA3xxx core material passivated in potential range of -1200 mV to -600 mV. This observed passive regions for both the materials were followed by a steep increase in the observed anodic current density signalling the breakdown of the passive layer. The breakdown potential for the clad alloy is ~200 mV lower than that of the core material. Further, the clad material showed slightly lower passive current density when compared to the core material. In addition, a steep decrease in the anodic current density prior to the onset of the passivation was observed between a potential range of -1350 mV to -1250 mV vs. Ag/AgCl for the AA7xxx clad material.

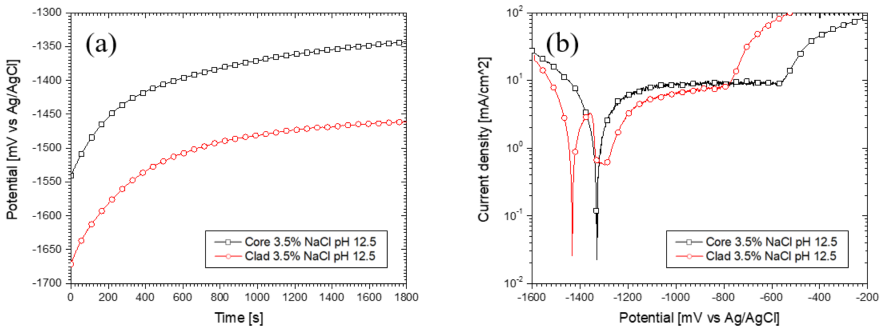

Figure 8.5: Electrochemical behaviour in 3.5 wt.% NaCl, pH 12.5 for core and clad material: (a) open circuit potential vs time and (b) anodic polarization curves for both materials.

8.3.1.2 Zero Resistance Ammetry

Figure 8.6 shows the results from Zero Resistance Ammetry measurements conducted by coupling the AA3xxx core and AA7xxx clad in 3.5 wt.% NaCl at pH 12.5. The two curves (figure 8.6 a and b) show evolution of current density and cell potential as a function of the test time. After an initial settle time of approximately 1 h, both potential and current values were stabilized with negligible variation. The current observed was positive with AA3xxx alloy as WE1 suggesting that under alkaline condition, core AA3xxx (WE1) is anodic to the clad AA7xxx (WE2).

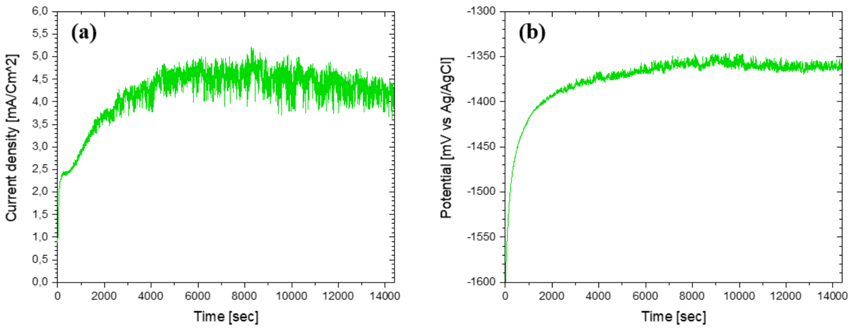

Figure 8.6: Results of ZRA measurement coupling core and clad in 3.5 wt.% NaCl, pH 12.5: (a) galvanic current density vs time and (b) galvanic potential vs. time. Positive current density is measured between WE1 and WE2 (AA3xxx core to AA7xxx clad), suggesting WE1 is anodic to WE2.

8.3.2 Acidified Synthetic Sea Water Testing

Figure 8.7 shows top view secondary electron SEM images of the weld area on the outside surface of the HF welded tube. Samples shown in figure 8.7 were SWAAT tested respectively for 15 days (a) and 25 days (b). Both pictures show the weld region devoid of the cladding, and adjacent area of the tube with clad material, and the corrosion interface between the two. Size of the devoid of clad area was measured to vary between 220 µm and 350 µm. After 15 days of testing, corrosion was observed to have just initiated, and a considerable amount of clad surface was still appearing un-attacked (marked as "Clad" in figure 8.7a). Corrosion initiation was observed to be preferentially present in regions close to the weld line-clad interface. However, after 25 days of testing, corrosion appeared to be uniformly spread all over the clad surface of the tube, while the weld area showed almost no corrosion.

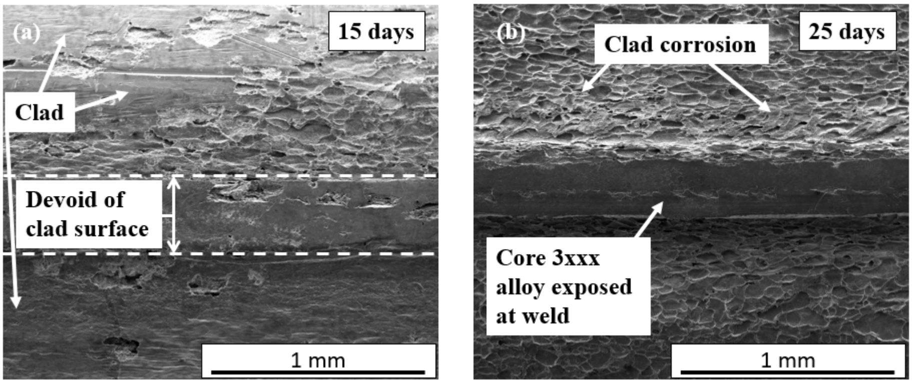

Figure 8.7: SEM SE images of the top surface of the tube after SWAAT testing: (a) after 15 days (b) after 25 days.

The cross sections of the SWAAT tested samples exposed for 15 and 25 days is shown in figure 8.8. Cross-sections show propagation of corrosion attack across the thickness of the tube during the SWAAT test. Corrosion is spread over the clad layer, protecting the core alloy weld regions completely. After 25 days of testing, the corrosion was uniformly spread all over the clad surface showing that almost all the available thickness of the clad layer is consumed, thus exposing the core material.

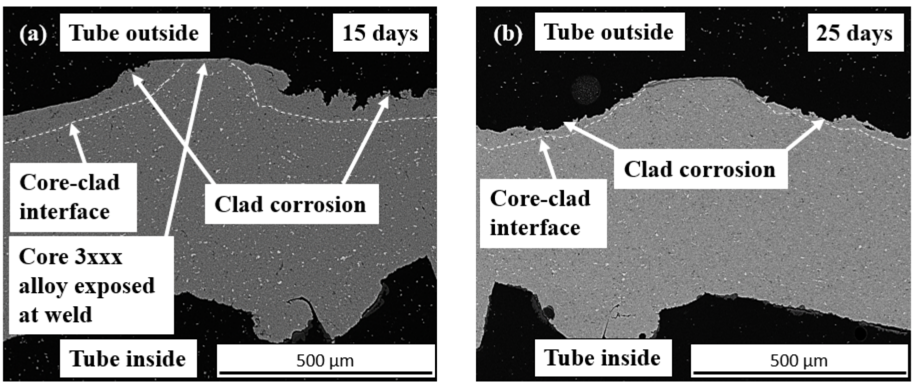

Figure 8.8: Back scattered electron SEM images of the cross-section showing weld region and nearby area: (a) after 15 days, and (b) after 25 days of SWAAT testing.

Figure 8.9 shows a digital image of a sample extracted from the SWAAT chamber after 25 days of testing. The sample was cleaned from the corrosion products (Ultrasonic cleaning in 70% HNO_3 bath) and cut into two small sections, presenting both the weld-containing half of the tube surface and opposite side as well. A shiny appearing, and un-attacked weld line exposing the core AA3xxx alloy can be easily identified (highlighted in picture), while rest of the tube surface (clad) presents uniformly spread corrosion attack, resembling the morphology showed in figure 8.7b (highlighted "clad corrosion").

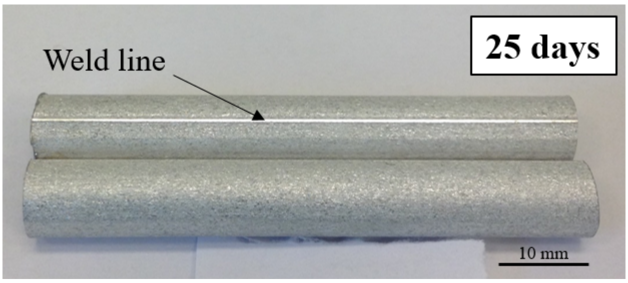

Figure 8.9: Digital photographs of the tube sample after 25 days of SWAAT test and after removal of the corrosion products.

8.3.3 Customized immersion tests

Figure 8.10 shows the surface view of the tubes tested in 3.5 wt.% NaCl solution at pH 12.5 by full immersion. Pictures shows progressive evolution of the state of samples after different intervals of time ((a) 2 h, (b) 24 h, and (c) 48 h). The entire surface appeared dark after 2 h of immersion, however the weld line shows a higher degree of attack. The overall corrosion attack across the weld line and all the clad surface increased with increase in time of exposure in the immersion testing.

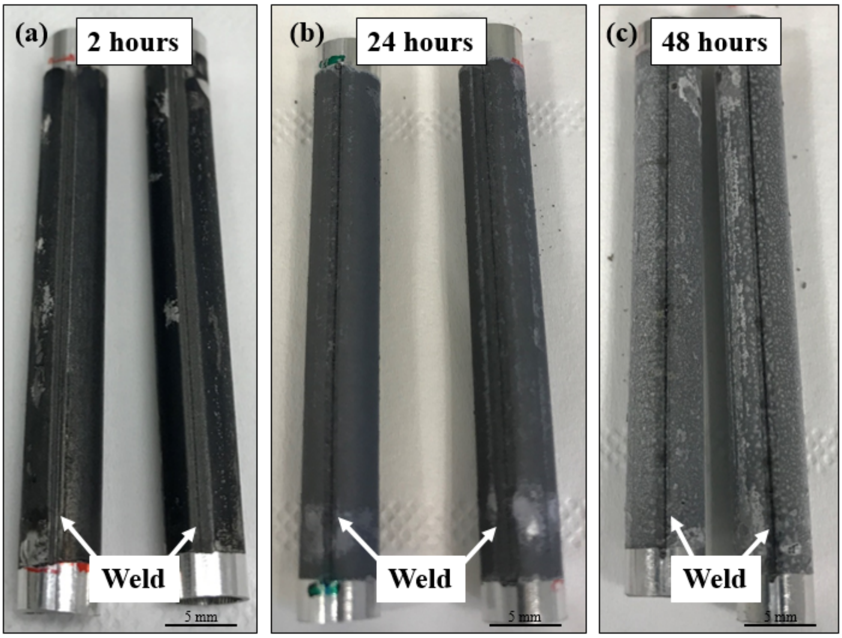

Figure 8.10: Digital photographs showing immersion tested tube samples: (a) 2 h, (b) 24 h and (c) 48 h of immersion, in pH 12.5, 3.5 wt.% aqueous NaCl solution.

Figure 8.11 shows the SEM SE image of the weld region of the tube after the immersion testing (after just 5 minutes of immersion). Micrograph shows initiation of many pits in areas without clad, where the core material is exposed. However, the clad area did not show significant attack. Nature of the attack in the core region is hemispherical pits typical of alkaline corrosion. At the bottom of both figure 8.11a and 8.11b, surface scratches were present on the side of the devoid of clad area, as a manufacturing artefact yielded by the scarfing process.

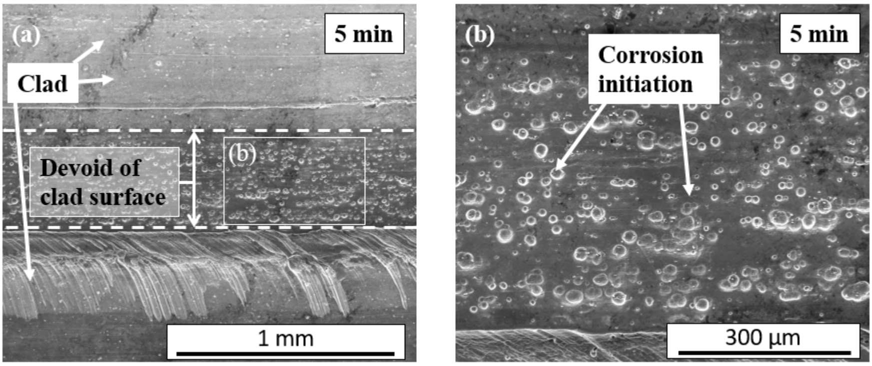

Figure 8.11: SEM SE images of the weld area after 5 minutes from immersion test in 3.5 wt.% NaCl at pH 12.5: (a) overview of welding and neighbouring surface, (b) magnified view of the devoid of clad surface.

In figure 8.12, two different stages of corrosion, centred in the devoid of clad area, are shown. Pictures show how a crater initially formed in the middle of the outer surface of the weld after 2 h of test (figure 8.12a). The crater gradually grows over a period of 24 h of test, and completely covers the devoid of clad area. At 48 h, tube failure by leakage was detected, which was caused by localized corrosion of the core AA3xxx alloy. This attack was focused at the weld, originating from the surface, where core material was exposed at outer environment. The corrosion attack was propagated across the depth of the tube finally corroding the entire wall thickness (see figure 8.12b).

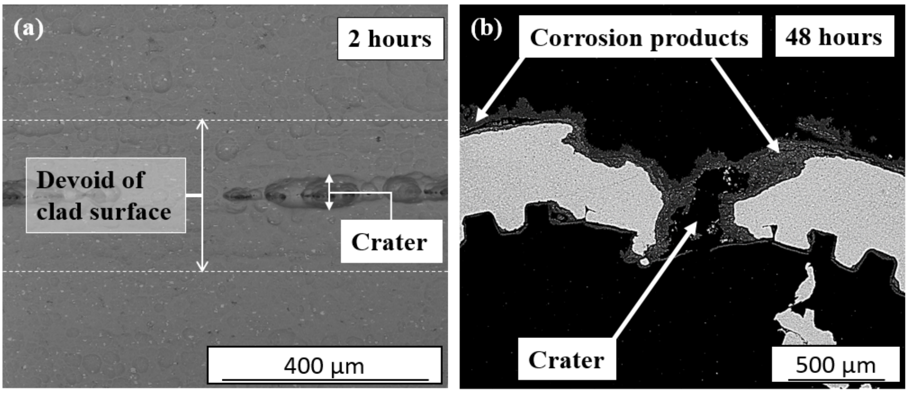

Figure 8.12: BSE SEM images of the weld area of tube samples: (a) topographic view, observed from the outside of the tube, at tube's surface level, after 2 h from immersion test start; (b) cross-section view after 48 h of immersion testing.

Corrosion products on the failed tube specimens were found to accumulate both at the welding (in the crater) and on the clad alloy's surface. These were analysed by EDS and the results are reported in wt.% in table 8.2, respectively indicated as site 1 and 2. Oxygen and aluminium were mainly detected, with minor traces of Na, Si and Cl, inferred to be related to the solution used for testing. Other elements lightly detected were Zn as for site 1, and Mn, Cu for site 2.

Table 8.2: EDS elemental composition (in wt.%) of corrosion products present on clad alloy surface (site 1) and in the crater (site 2).

	Site 1	**Site 2**
C	2.8 ± 1.5	1.6 ± 0.3
O	49.7 ± 1.4	48.4 ± 0.3
Na	0.2 ± 0.1	0.2 ± 0.1
Al	46.9 ± 3.2	49.2 ± 0.7
Si	0.1 ± 0.1	
Cl	0.1 ± 0.1	0.1 ± 0.1
Zn	0.2 ± 0.1	
Mn		0.3 ± 0.1
Cu		0.2 ± 0.1

8.3.4 Microstructural characterization of passive film

Figure 8.13 presents high angle annular dark field (HAADF) image, obtained by transmission electron microscopy, of the thin passive film that was observed to develop on top of the AA7xxx clad material, when electrochemically coupled with the core AA3xxx alloy in 3.5 wt.% NaCl at pH 12.5 for a period of 4 h.
As can be observed from figure 8.13, the AA7xxx clad developed a thin (200-280 nm thick) passive film under alkaline conditions which displayed a highly irregular/porous nature and was not lost to the electrolyte, but rather uniformly covered the entire surface of the AA7xxx clad material. As highlighted in the pictures, Pt deposited during the TEM thin lamella sample preparation, not only covered the mentioned surface oxide film, but also permeated and mixed with it.

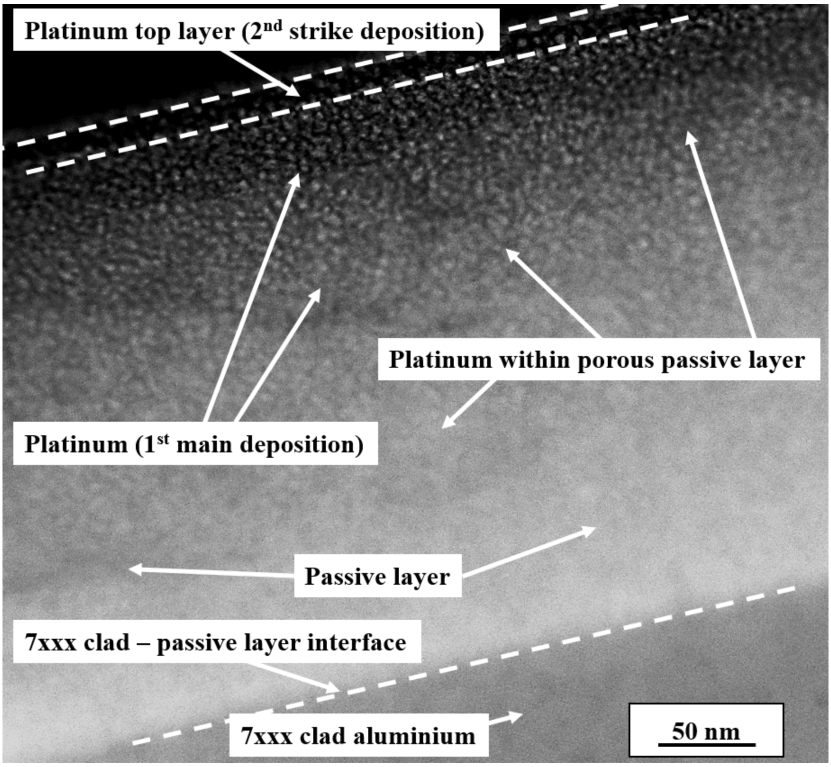

Figure 8.13: HAADF STEM micrograph from the in-situ focused ion beam milled cross-section of the AA7xxx clad alloy surface, presenting the morphology of the oxide layer when galvanically coupled with AA3xxx in pH 12.5 solution for 4 h.

The EDS elemental maps obtained in scanning transmission electron microscopy mode, presented in figure 8.14, suggest the presence of Al oxide (aluminium and oxygen traces), zinc oxide (zinc and oxygen traces), general presence of Cu (Pt is from the surface layer used for FIB cutting). Additionally, a particle of considerable dimensions, if compared to the overall thickness of the layer, was highlighted and observed to be a Si-rich compound, with traces of Zn and Cu. High amount of Pt within the oxide layer show the layer is porous. Cu signal is due to the Cu grid used for sample mounting.

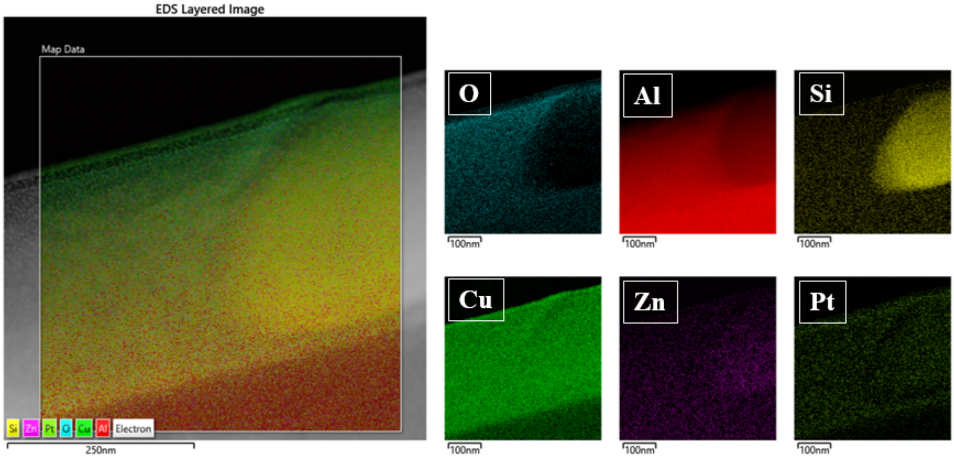

Figure 8.14: STEM HAADF micrograph with EDS O, Al, Si, Cu, Zn and Pt elemental map overlay, and individual elemental maps for O, Al, Si, Cu, Zn and Pt.

8.4 Discussion

In this study, high frequency welded clad Al tubes, were tested with the scope of addressing their performance in terms of corrosion resistance in high pH environments. In order to have a benchmark for their behaviour in acidic conditions, SWAAT testing was employed, while high alkaline environment testing was performed by immersion in customised immersion test setups. The results from exposure tests are supported with potentiodynamic anodic polarization, zero resistance ammetry, and investigation of microstructural and compositional characterization.
The results from the OCP evolution of the individual AA3xxx core and A7xxx clad materials showed that the AA7xxx alloy was characterized by a more negative potential than the AA3xxx core alloy, in both pH neutral and pH 12.5 environment. This is as expected due to the compositional nature of the AA7xxx alloy which contains Zn making it electrochemically active. Pech-Canul et al [36]. studied similar material combinations in a SWAAT cell where the AA3xxx fin was coupled with the AA1xxx tube material having a Zn diffusion layer, and observed that the Zn containing surface of the AA1xxx alloy corroded preferen-

tially thus protecting the fin material. After prolonged exposure there was enough Zn remaining on the tube material to prevent corrosion of the underlying AA1xxx tube. Ma et al. studied [37] the electrochemical behaviour of a Zn containing Al alloy in solutions of various pH levels from highly acidic to highly alkaline, and noted that there is a difference of ~200 mV in the OCP value when compared between pH 7 and pH 11. The OCP values decreased considerably with increasing pH levels of the solution for the Zn containing Al alloy. Further, it was also shown that there is clearly observable passive region while anodic polarization in an alkaline pH 11 solution when compared to a neutral pH 7 solution. In our studies, potentiodynamic anodic polarization data and the SWAAT tests in acidic media show similar results, but anodic polarization tests in pH 12.5 environment show that the alkaline environment causes a passivation of these materials while there is no discernible passive region when polarized in pH neutral Cl^{-} containing solutions (showed in figure 8.4b). However, generally, the OCP and anodic polarization test results show that the intended purpose of the AA7xxx clad is satisfied in both conditions as it would provide a sacrificial protection to the AA3xxx core alloy when used as a cladding material.

Finished HF welded tubes, with their devoid of clad area where the underlying AA3xxx core alloy was exposed, were tested using ZRA, and immersion in alkaline pH 12.5 environment. The results showed deviation from the expected sacrificial behaviour of the AA7xxx alloy. The differences manifested as a reversal of role for the AA7xxx where corrosion of the coupled AA3xxx was observed in the zero resistance ammetry measurements in pH 12.5 alkaline environment, which was in line with the observations from the customised immersion testing in pH 12.5 alkaline environment. In both the cases it was observed that the AA3xxx underwent corrosion while the AA7xxx did not suffer severe corrosion. This is in contrary to the observations from the OCP and anodic polarization experiments. The ZRA measurements performed by coupling AA7xxx alloy an AA3xxx alloy in neutral solution was reported by Shi et al. [38] where it was observed that the AA7xxx alloy behaved as an anode to the AA3xxx, and provided sacrificial protection.

The SEM observations clearly show corrosion propagation through the

AA3xxx core alloy that was exposed after HF welding of the tube when immersed in alkaline pH 12.5 environment, while the AA7xxx clad alloy underwent corrosion in the acidic environment of the SWAAT testing. A highly irregular and porous passive layer/oxide layer was observed on the AA7xxx sample that was extracted after being coupled to the AA3xxx alloy in pH 12.5 alkaline solution for 4 h. This confirms the observations from the customised pH 12.5 immersion tests where the AA7xxx alloy did not undergo corrosion, which can be linked to the protection offered by this oxide layer formed on the AA7xxxx alloy formed in alkaline environment (as seen from the STEM EDS analysis). Looking closely at the anodic potentiodynamic polarization curve for the AA7xxx alloy in pH 12.5 environment, in the potential range corresponding to cell potential for the ZRA measurements an interesting observation can be made. The steep decrease in the anodic current density prior to increase again followed by onset of passivation for AA7xxxx polarized in pH 12.5 is in the same potential range (-1375 mV to -1350 mV vs. Ag/AgCl) as the cell potential observed for the performed ZRA experiments. The decrease in anodic current density of Al-Zn in alkaline solutions in these potential ranges has been reported earlier by Park et al. [39], where a passivation was observed and attributed to a protective 'Type 2' ZnO film formed on the surface of the alloy due to oxidation of the Zn in the alloy surface.
Considering the Pourbaix diagrams of Zn, at 22 °C, in aqueous solution, with Zn ions molality 0.001 mol/kg and Cl molality 0.6 mol/kg (simulating the previously described alkaline test conditions), showed in figure 8.15, a relatively wide area for thermodynamic stability of ZnO is found to extend from pH 7.5 up to 13. Therefore, from a thermodynamic point of view, the formation of an oxide film that is stable in the environment is supported. Further, Park et al. [39] presented similar findings of Al-Zn alloys immersed in 4M NaOH solution, where Zn oxidation compounds were detected on the alloy surfaces. This was attributed to the dissolution of Zn as $Zn(OH)_4^{2-}$ from the Al-Zn alloy surface and later re-precipitation onto the surface as $Zn(OH)_2$ or defective ZnO. This defective film was termed as 'Type 1 film' and described to be loose and flocculent (different from the dense and protective 'Type 2' film of ZnO formed during potentiodynamic anodic polarization), similar to the observations from the STEM imaging per-

formed in the present work [40]. The formation of this 'Type 1 film' on the AA7xxx surface, when coupled with the AA3xxx alloy, was triggered by galvanic coupling and initiation of corrosion on the AA7xxx. This led to reduced capability of the AA7xxx alloy for sacrificial protection, thorough the hindering of further corrosion propagation and hence resulting in preferential corrosion of the AA3xxx alloy surface in the highly alkaline pH 12.5 environment.

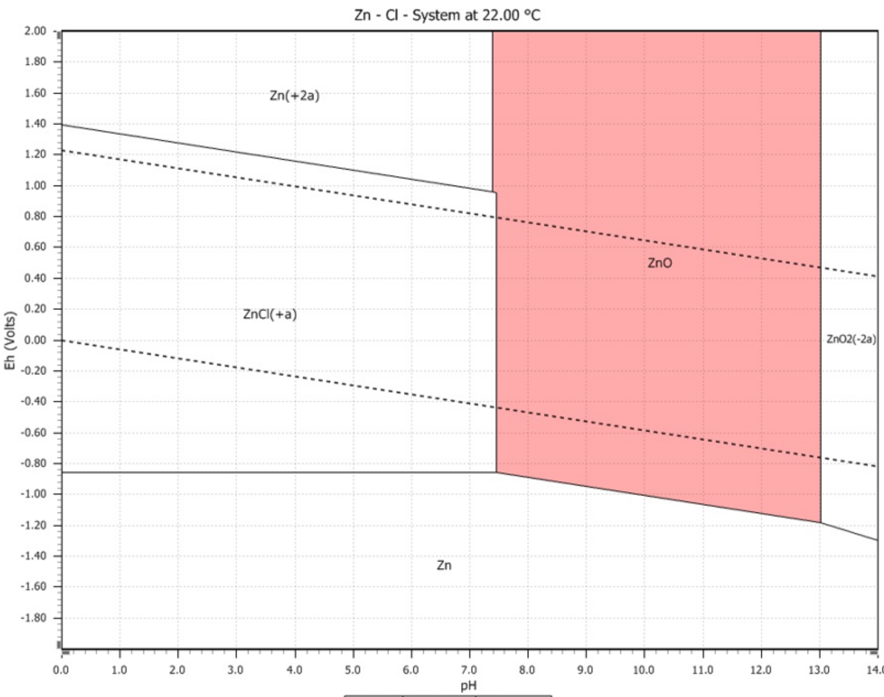

Element	Molality	Pressure
Zn	1.00E-003	1.00E+000
Cl	6.00E-001	1.00E+000

Figure 8.15: Pourbaix diagram of Zn, at 22 °C, in aqueous solution, with Zn ions molality 0.001 mol/kg and Cl molality 0.6 mol/kg (ZnO thermodynamic stability zone highlighted in red).

8.5 Conclusion

The present study investigated the acidic, neutral, and alkaline corrosion behaviour of high frequency welded aluminium tubes with focus on the sacrificial protection ability of the AA7xxx alloy clad to the high strength AA3xxx core material. It was observed that:

1. AA7xxx alloy surface had a lower OCP when compared to AA3xxx alloy in both pH neutral and pH 12.5 alkaline Cl^- containing solutions.

2. Potentiodynamic anodic polarization of the alloys surfaces in pH neutral showed no discernible passivation of the alloys, while both the alloys showed a clear passivation range when polarized anodically in pH 12.5 alkaline solution.

3. ZRA measurements in alkaline solution showed a reversal of roles of the alloy material, and corrosion of the AA3xxx alloy was observed when coupled with AA7xxx.

4. SWAAT testing of the welded tubes with an exposed AA3xxx surface along the weld line showed preferential dissolution of the AA7xxx alloy, thus providing sacrificial protection to the exposed AA3xxx surface.

5. In highly alkaline environment, localized attack and dissolution of the exposed AA3xxx alloy along the weld line took place, while the outer AA7xxx alloy showed very little corrosion.

6. Passivation of the AA7xxx alloy in highly alkaline solutions due to formation of Type 1 film consisting of ZnO or/and $Zn(OH)_4^{2-}$ caused the AA3xxx to corrode preferentially along the weld line.

Acknowledgements

The authors would like to thank Norsk Hydro and Innovation Fund Denmark (grant 5189-00144B) for their technical and financial support of the project. We also thank Mr. A. Mangelsdorf, Dr. M. Pasqualon and Mr. T. Guillaume from Norsk Hydro for their support.

Bibliography

[1] T. Dursun, C. Soutis, Recent developments in advanced aircraft aluminum alloys, Mater. Des. 56 (2014) 862–871.

[2] W.S. Miller, L. Zhuang, J. Bottema, A.J. Wittebrood, P. De Smet, A. Haszler, A. Vieregge, Recent development in aluminum alloys for the automotive industry, Mater. Sci. Eng. A 280 (2000) 37–49.

[3] M. Leary, Materials selection and substitution using aluminum alloys. In: Roger Lumley (Ed.). Fundamentals of Aluminum Metallurgy: Production, Processing and Applications, Cambridge UK: Woodhead Publishing Limited (2011) 784–827.

[4] C. Vargel, M. Jacques, M.P. Schmidt, Chapter A.1 - the advantages of aluminum. In: C.V.J.P.B.T.-C. of A. Schmidt. Elsevier. Amsterdam (2004) 9–16.

[5] G. Djukanovic, Copper vs. Aluminium – substitution slows but continues, Aluminium insider (2016).

[6] C. Rochet, M. Veron, E.F. Rauch, T.C. Lowe, B. Arfaei, A. Laurino, J.P. Harouard, C. Blanc, Influence of equal-channel angular pressing on the microstructure and corrosion behaviour of a 6xxx aluminium alloy for automotive conductors, Corros. Sci. 166 (2020) 108453.

[7] HVAC System Market by Heating Equipment (Heat Pumps, Furnaces), Ventilation Equipment (Humidifiers, Dehumidifiers), Cooling Type (VRF Systems, Unitary Air Conditioners), Implementation Type, Application, and Geography - Global Forecast to 2023, Markets and Markets, Report Code: SE 4420, published Apr 2018.

[8] M. Hofuku, Development trends in inner-grooved tubes in Japan, Hitachi Cable Review. 26 (2007) 1–3.

[9] L.P.M. Colombo, A. Lucchini, A. Muzzio, Flow patterns, heat transfer and pressure drop for evaporation and condensation of R134A in microfin tubes, Int. J. Refrig. 35 (2012) 2150–2165.

[10] R. Kaji, S. Yoshioka, H. Fujino, The effect of inner grooved tubes on the heat transfer performance of air-cooled heat exchangers for CO2 heat pump system. International Refrigeration and Air Conditioning Conference; Purdue, July 16-19 2012.

[11] D. Zhou, X. Chengdong, J. Lv, L. Li, inventors; Yinbang Clad Material Co., LTD, assignee. Aluminum alloy composite strip for internal threaded heat exchange tube and manufacturing therefor. World Intellectual Property Organization Patent WO 2018049585 A1. Mar 22 2018.

[12] R.K. Nichols, PE, H.N. Udall, High frequency welding of aluminum. A Thermatool Corp. Publication, T.P. n. 111, Rev. 2. March 1999.

[13] J. Wright, Optimizing efficiency in HF tube welding processes. in: Tube & Pipe Technol. November/December 1999.

[14] K. Hyun-Jung, Y. Sung-Kie, Three dimensional analysis of high frequency induction welding phenomena, Trans Korean Soch Mech Eng A, 30 (2006) 865–972.

[15] G.G.B. Zaffaroni, O.V. Mishin, U.M. Ciucani, C. Gundlach, J.H. Nordlien, R. Ambat, Characterization of High Frequency Welded Aluminium Microfin Tube for Heat Exchangers. **to be submitted**

[16] I. Schoukens, F. Cavezza, J. Cerezo, V. Vandenberghe, V.C. Gudla, R. Ambat, Influence of de-icing salt chemistry on the corrosion behavior of AA6016, Mater. Corros. 69 (2018) 881–887.

[17] M. Aggerbeck, A. Herbreteau, M. Rombouts, J. Verwimp, R. Ambat, Alkaline corrosion properties of laser-clad aluminum/titanium coatings, Anti-Corrosion Methods Mater. 62 (2015) 37–47.

[18] I. Boukerche, S. Djerad, L. Benmansour, L. Tifouti, K. Saleh, Degradability of aluminum in acidic and alkaline solutions, Corros. Sci. 78 (2014) 343–352.

[19] S.I. Pyun, S.M. Moon, Corrosion mechanism of pure aluminium in aqueous alkaline solution, J. Solid State Electrochem. 4 (2000) 267–272.

[20] S. Tierce, C. Casenave, H. Robidou, N. Pébère, C. Blanc, G. Mankowski, Electrochemical behavior of brazed aluminum alloys used in automotive heater cores, in: SAE Tech. Pap., SAE International, 2006.

[21] R.D. Tait, C.J. Rogers, A.J. Cottone, J.P. Henkes, Z.P. Saperstein, Corrosion resistance of the as brazed PF® heat exchanger as achieved by alloy selection, SAE Tech. Pap. 100 (1991) 606–612.

[22] S.D. Meijers, C.E. Caicedo Martinez, S. Desikan, Tube-fin interaction - A closer look at the corrosion mechanism, SAE Tech. Pap. 114 (2005) 876–883.

[23] K. Ishikawa, H. Kawase, H. Koyama, Y. Hasegawa, K. Negura, M. Nonogaki, Development of pitting corrosion resistant condenser with zinc-arc-spray extruded multi-cavity tubing, SAE Tech. Pap. 100 (1991) 594–605.

[24] Q. Shi, F. Liang, B. Cheadle, Electrochemical behaviors of quad-layer aluminum brazing sheet composite for automotive applications, Corrosion. 60 (2004) 492–500.

[25] M. Melander, R. Woods, Corrosion study of brazed aluminum radiators retrieved from cars after field service, in: Corrosion (2010) 0150051–01500514.

[26] K. Bordo, V.C. Gudla, L. Peguet, A. Afseth, R. Ambat, Electrochemical profiling of multi-clad aluminium sheets used in automotive heat exchangers, Corros. Sci. 131 (2018) 28–37.

[27] M. Edo, S. Kuroda, A. Watanabe, K. Tohma, Localized corrosion of aluminum clad sheets in alkaline solution, 53 (2003) 55–60.

[28] B. Ren, inventor; Arconic Inc., assignee. Multi-layer aluminium alloy sheet product for tubes for heat exchangers. United States Patent US 9964364 B2. Mar 08 2018.

[29] M. Yoshino, M. Edo, S. Kuroda, M. Asano, K. Tohma, Effect of additional Si and Cu on strength and corrosion resistance of sacrificial anode fin stock for automotive heat exchangers, Journal of Japan Institute of Light Metals, 59 (2009) 229-235.

[30] S. Iwao, M. Asano, Influence of heat treatment on corrosion resistance of aluminum alloy brazing sheet, Journal of Japan Institute of Light Metals, 57 (2007) 589-594.

[31] ASTM Standard, Designation G85, Standard practice for modified salt spray (fog) testing, 2006.

[32] V.C. Gudla, K. Rechendorff, Z.I. Balogh, T. Kasama, R. Ambat, In-situ TEM investigation of microstructural evolution in magnetron sputtered Al-Zr and Al-Zr-Si coatings during heat treatment, Mater. Des. 89 (2016) 1071–1078.

[33] K. Bordo, V.C. Gudla, L. Peguet, A. Afseth, R. Ambat, Electrochemical profiling of multi-clad aluminium sheets used in automotive heat exchangers, Corros. Sci. 131 (2018) 28–37.

[34] S.T. Abrahami, J.M.M. de Kok, V.C. Gudla, R. Ambat, H. Terryn, J.M.C. Mol, Interface strength and degradation of adhesively bonded porous aluminum oxides, Npj Mater. Degrad. 1, 8 (2017) 1-8.

[35] S.T. Abrahami, J.M.M.M. de Kok, V.C. Gudla, K. Marcoen, T. Hauffman, R. Ambat, J.M.C. Mol, H. Terryn, V.C. Gudla, K. Marcoen, R. Ambat, H. Terryn, S.T. Abrahami, Fluoride-induced interfacial adhesion loss of nanoporous anodic aluminium oxide templates in aerospace structures, ACS Appl. Nano Mater. 1 (2018) 6139—6149.

[36] M.A. Pech-Canul, J.C. Guía-Tello, M.I. Pech-Canul, J.C. Aguilar, J.A. Gorocica-Díaz, R. Arana-Guillén, J. Puch-Bleis, Electrochemi-

cal behavior of tube-fin assembly for an aluminum automotive condenser with improved corrosion resistance, Results Phys. 7 (2017) 1760–1777.

[37] J. Ma, J. Wen, Q. Li, Q. Zhang, Electrochemical polarization and corrosion behavior of Al-Zn-In based alloy in acidity and alkalinity solutions, Int. J. Hydrogen Energy. 38 (2013) 14896–14902.

[38] R. Shi, F. Liang, E. Lazo, M. Kozdras, Effect of Brazing Temperature on Electrochemical Performance and Zinc Diffusion of AA7072 Clad in Tri-layer Aluminum Brazing Sheet AA7072/3003/4343, SAE Trans. 114 (2005) 859–867.

[39] I.J. Park, S.R. Choi, J.G. Kim, Aluminum anode for aluminum-air battery – Part II: Influence of In addition on the electrochemical characteristics of Al-Zn alloy in alkaline solution, J. Power Sources. 357 (2017) 47–55.

[40] R.W. Power, M.W. Breiter, Anodic Dissolution and Passivation of Zinc in Concentrated Potassium Hydroxide Solutions, Electrochem Soc-J. 116 (1969) 719–729.

9 General Discussion

Major contribution from the present project is that it laid the foundation for producing inner grooved HF welded aluminium tube for heat exchangers with optimized properties for Hydro Aluminium, suitable for commercial production. The outcome was the design and construction of a process line able to deliver coiled aluminium inner grooved welded tubes, meeting inner pattern geometry requirements, free of inner weld bead and/or inner solid contamination. Detailed investigation of the microstructure and mechanical properties of the weld region showed significant effect by the welding process. In the material with core 3xxx aluminium alloy with a 10% 7xxx clad for corrosion protection purposes (sacrificial function of the outer surface of tubes), the clad layer was affected by the welding process. The analysis highlighted an elongated grain structure of the core alloy in the as-received strip material, typical of rolled products. However, the the clad alloy, in as-received condition, due to its inferred higher thermal susceptibility (heat treatable alloy) showed remarkable grain growth during the hot rolling process employed in the joining of core and clad strip layers. Upon HF welding, the materials showed remarkable microstructural transformations in the neighbourhoods of the joint. These transformations consisted in the formation of a very fine and heavily distorted grain structure along and near the weld line. This structure resulted from a significant compression strain at the forging interface and was characterized by a high frequency of LABs. Adjacent HAZ regions on both sides corresponded to the material affected by the local heating generated by induction. As a direct consequence of these microstructural changes, significant gradients in hardness were measured across the weld zone. The HF welded aluminium tubes showed highest levels of hardness for the embossed not-thermally affected areas and at the joining line, while lower hardness values were measured in the HAZs adjacent to the weld. The gradients in mechanical properties showed the need for the introduction of a thermal treatment into the process line of tubes for homogenizing the microstructure. This ensures avoiding potential presence of spots for localized stress increase upon the raising of the internal pressure of the tubes (i.e. upon burst pressure testing). The research results provided a benchmarking base for the evaluation of the in-line annealing process effectiveness and its process parameter optimization.

The characterization work of the welded tubes (chapter 6) highlighted another critical aspect in relation to the linear welding that is the so called "devoid-of-clad" area. The HF welding process produce squeezing of the molten aluminium at the weld due to the forging during welding. Therefore, a scarfing process is done right after the welding stage for the removal of the material flash remaining on the outer surface of tubes. Analysis of the welded tube showed that the scarfing process remove the clad layer on the tube along the weld line. From the corrosion point of view, exposure of core 3xxx alloy at this region cause galvanic coupling with Zn-rich clad alloy.

Additionally, EBSD and differential interference optical microscopy analysis showed the presence of well-defined material flow patterns, in correspondence of the embossed surface of the core 3xxx alloy.

Overall, the results from the investigations presented in Chapter 6 allowed modification of processing tools design and steps in the manufacturing process based on the implications of varying strip edge geometry/surface finish on the induced heat distribution, welding process stability and final metallic joint quality/morphology. Based on this, several modifications to the process have been carried out including testing and in-line installation of the novel engineering solutions mentioned in chapter 5. Some of the modifications are not detailed in this thesis due to confidentiality requirements as part of this Industrial PhD programme.

The work presented in Chapter 7 focussing on inner corrosion of the embossed tube was based on the morphological and microstructural changes found from the embossing process (Chapater 6). The FEM sim-

ulation results clearly showed the asymmetry in deformation behaviour during the embossing process. The microstructural analysis supported this, showing the grain flow toward one direction of the fins during the embossing process. It was found an existing correlation between the use of an anisotropic deformation process, such as the roll forming used to emboss the aluminium strips, and the corrosion susceptibility of the obtained patterned surfaces. It was found that the process results in the development of localized (non-symmetrically distributed with respect to the embossed fin geometry) sites characterized by higher inter granular corrosion susceptibility.
The results of the investigation in Chapter 7 showed how product lifetime may potentially affected by the tubes orientation with respect to the refrigerant flow speed direction. In other words, if these tubes would be installed with the fins weaker side directly facing the refrigerant fluid flow (flow lines encountering weak side of the fin first, with the second side being partially shielded), product life for erosion corrosion attack initiation would be reduced. Based on this research, additional development work was carried out improving the design of the embossing tooling, reducing the amount of plastic surface strains generated during the manufacturing.
Chapter 8 described the corrosion analysis carried out on finished products in order to assess their resistance in different aggressive environments. Results from SWAAT tests justified the materials choice for neutral to acidic environments, highlighting an optimal efficiency of the clad sacrificial function, able to provide full protection to the underlying core alloy up to 30 days of testing and with a tube survival (no leakage upon take out from corrosion chamber) up to 60 days. However, the simulation of critical alkaline conditions generated by improper dilution of commonly used washing detergents in an outdoor operative life environment (stagnant solution, high humidity and presence of chlorides) showed potential for dramatic products failure. In fact, it was found that the clad in such conditions was not able to provide its sacrificial cathodic protection to the core alloy anymore. On the contrary, it was found that the exposed surface coupling of the core and clad at the devoid-of-clad tube surface, in highly alkaline conditions (pH 12.5), results in an equilibrium potential of the two alloys, at which the Zn-rich 7xxx clad was able to passivate, while the 3xxx core undergone

aggressive alkaline dissolution. In just 48 hours, such condition caused the premature failure of the tubes, characterized by a localized attack of the weld and generating a crater through the wall thickness of the tube. These findings initiated further process optimisation work aimed at the development of an improved process, excluding the formation of devoid-of-clad sites at the surface of the tubes due to the scarfing process.

10 Conclusion

Present PhD project studied the process and materials involved in the manufacturing of inner grooved high frequency welded aluminium tubes for mechanically expanded tube-fin plate heat exchangers.
In this work, attention was payed to the microstructural and corrosion issues connected to choice of material and manufacturing methodology. Based on this investigation, the following conclusions were obtained:

1. During the HF welding of aluminium tubes, complete and pore-free joint is created by compression of induction-heated edges with no evidence of oxide presence found along the weld. The manufacturing process involves scarfing of the outer surface of the weld, which results in a small "devoid-of-clad" area along the longitudinal direction of the tube.

2. Within the 50–250 µm along the weld, the compressed microstructure contains fine subgrains separated by mostly LABs. Adjacent to this weld region, there are two 250–300 µm wide HAZs. The HAZs are partially recrystallized with an average recrystallized grain size of 15 µm. The as-embossed microstructure characterized by high frequency of LABs preserved at a distance greater than 0.4 mm from the joint, and a characteristic flow pattern is observed near the embossed fins.

3. The microhardness in the welded tube varies in response to the microstructural variations. The Vickers hardness ranges from ∼55 HV in the partially recrystallized HAZ region to ∼68 HV in the weld region which presents the compressed microstructure. The

average microhardness was also high, 66±3 HV, in the embossed core alloy beyond the HAZs.

4. The embossing process generated an anisotropic microstructure in the samples, characterized by unevenly distributed formation of near–surface deformed regions. Such localized regions of higher plastic deformation were found to be generated by differences in the material plastic flow, during the cold forming of the aluminium strips.

5. Analysis of embossed strip samples, after artificially induced corrosion attack, revealed the presence of sites with increased IGC susceptibility, distributed as a function of the embossed pattern geometry and corresponding to those zones of higher plastic deformation observed on one side of the fins.

6. AA7xxx alloy surface had a lower OCP when compared to AA3xxx alloy in both pH neutral and pH 12.5 alkaline Cl^- containing solutions. However, ZRA measurements in alkaline solution showed a reversal of roles of the core alloy and clad with corrosion for the AA3xxx alloy when coupled with AA7xxx.

7. Potentiodynamic anodic polarization of the alloys surfaces in pH neutral showed no discernible passivation of the alloys, while both the alloys showed a clear passivation when polarized anodically in pH 12.5 alkaline solution. Passivation of the AA7xxx alloy in highly alkaline solutions due to formation of Type 1 film consisting of ZnO or/and $Zn(OH)_4^{2-}$ caused the AA3xxx to corrode preferentially along the weld line.

8. SWAAT testing of the welded tubes with an exposed AA3xxx surface along the weld line showed preferential dissolution of the AA7xxx alloy, thus providing sacrificial protection for the exposed AA3xxx surface. However, in highly alkaline environment, localized attack and dissolution of the exposed AA3xxx alloy along the weld line took place while the outer AA7xxx alloy showed very little corrosion.

The research work built a knowledge base able to guide and support the optimization of the embossing and welding process to produce the tubes, while the results from developed process during the PhD programme, and product modification were able to achieve the company's commercial goal.
Synergistic efforts of research and development activities of this project contributed to the solution to most of the manufacturing challenges historically stopping this technology from full commercialization, giving Norsk Hydro the opportunity to gain and consolidate a dominant position in the expanding HVAC&R market in the years to come.

11 Future work

- Analysis of microstructure and corrosion issues of embossed aluminium surfaces demonstrated a pattern geometry-dependent distribution of higher IGC susceptibility spots. Future work will study the effects of erosion corrosion in glycol-based solutions for the embossed Al tubes. The work will focus on determining possible correlations between pattern geometry/tube orientation and corrosion resistance, with respect to refrigerant fluid flow speed.

- Studies on corrosion performances of tubes showed that, in highly alkaline environment, localized attack and dissolution of the exposed AA3xxx alloy along the weld line took place, while the outer AA7xxx alloy showed very little corrosion. Investigations will be carried out in order to find a suitable process modification, able to eliminate the so-called "devoid of clad" area, which is at the origin of the observed issue.

- Potentiodynamic anodic polarization tests revealed differences between the corrosion behaviour in NaCl and glycol-containing solution with 250 ppm NaCl contamination of the embossed aluminium surfaces. Such behaviour was attributed to the function of corrosion inhibitors in the solution, designed to provide protection to the metallic surface by establishment of passive inhibitor film, being influenced by the embossed surface patterning. The exact reason for this behaviour will be further investigated.

- The materials used in the manufacturing of tubes of present project have been extensively characterized in their mechanical and corrosion properties. Future work will look into different material solutions, possibly providing more suitable properties, thus better processing and higher finished products' performances/quality. These may include multiple-clad strip material and/or a novel single alloy solution.

- The development work aimed at the process improvement for the manufacturing of inner grooved high frequency welded aluminium tubes will continue, extending the scope to different inner surface pattern geometries and tube sizes.

Bibliography

[1] M. H. Jacobs, Introduction to Aluminium as an Engineering Material, Interdisciplinary Research Center in Materials, The University of Birmingham, UK, available in TALAT - a training programme for aluminium application technologies in Europe, Feb. 2016.

[2] R. Cobden, Aluminium: Physical Properties, Characteristics and Alloys, Alcan, Banbury, available in TALAT - a training programme for aluminium application technologies in Europe, Feb. 2016.

[3] T. Cock, Aluminium - A Light Metal, Skanaluminium, Oslo, available in TALAT - a training programme for aluminium application technologies in Europe, Feb. 2016.

[4] https://www.aluminiumleader.com/

[5] M. Leary, Materials selection and substitution using aluminium alloys, Fundamentals of Aluminium Metallurgy: Production, Processing and Applications, Woodhead Publishing Limited, Cambridge UK (2011) 784–827.

[6] C. Vargel, M. Jacques, M.P. Schmidt, Chapter A.1 - the advantages of aluminium, C.V.J.P.B.T.-C. of A. Schmidt, Elsevier, Amsterdam (2004) 9–16.

[7] T. Dursun, C. Soutis, Recent developments in advanced aircraft aluminium alloys, Mater. Des. 56 (2014) 862–871.

[8] W.S. Miller, L. Zhuang, J. Bottema, A.J. Wittebrood, P. De Smet, A. Haszler, A. Vieregge, Recent development in aluminium alloys for the automotive industry, Mater. Sci. Eng. A 280 (2000) 37–49.

[9] HVAC System Market by Heating Equipment (Heat Pumps, Furnaces), Ventilation Equipment (Humidifiers, Dehumidifiers), Cooling Type (VRF Systems, Unitary Air Conditioners), Implementation Type, Application, and Geography - Global Forecast to 2023, Markets and Markets, Report Code: SE 4420, published Apr 2018.

[10] T. Ebisu, Evaporation and Condensation Heat Transfer Enhancement for Alternative Refrigerants Used in Air-Conditioning Machines, Heat Transfer Enhancement of Heat Exchangers, Kluwer Academic Publishers (1999) 579-600.

[11] M. Houfuku, Development trends in inner-grooved tubes in Japan, Hitachi Cable Review No.26 (August 2007) 1–3.

[12] R. Kaji, S. Yoshioka, H. Fujino, The Effect of Inner Grooved Tubes on the Heat Transfer Performace of Air-Cooled Heat Exchangers for CO2 Heat Pump System, International Refrigeration and Air Conditioning Conference at Purdue, July 16-19 2012.

[13] R. K. Nichols, H.N. Udall, High frequency welding of aluminum, A Thermatool Corp. Publication, T.P. n. 111, Rev. 2. March 1999.

[14] D. Zhou, X. Chengdong, J. Lv, L. Li, inventors; Yinbang Clad Material Co., LTD, assignee. Aluminum alloy composite strip for internal threaded heat exchange tube and manufacturing therefor. World Intellectual Property Organization Patent WO 2018049585 A1. Mar 22 2018.

[15] G. Djukanovic, Copper vs. Aluminium – substitution slows but continues, Aluminium insider (2016).

[16] J. Wright. Optimizing Efficiency in HF Tube Welding Processes. Tube & Pipe Technology - November/December 1999.

[17] K. Hyun-Jung, Y. Sung-Kie, Three Dimensional Analysis of High Frequency Induction Welding Phenomena, Transactions of the Korean Society of Mechanical Engineers A, Volume 30. Issue 7. (2006) 865-972.

[18] L.P.M. Colombo, A. Lucchini, A. Muzzio, Flow patterns, heat transfer and pressure drop for evaporation and condensation of R134A in microfin tubes, international journal of refrigeration, 35 (2012) 2150 – 2165.

[19] R.L. Webb, N.H. Kim, Principles of Enhanced Heat Transfer, second ed., Taylor & Francis Group, New York (2005).

[20] J.R. Thome, Engineering Data Book III, Wolverine Tube Inc (2004).

[21] Z. Wu, B. Sundén, V.V. Wadekar, W. Li, Heat transfer correlations for single-phase flow, condensation and boiling in microfin tubes, Heat Transfer Eng. 36 (2015) 582–595.

[22] T. Ebisu, H. Fujino, K. Torikoshi, Heat transfer characteristics and heat exchanger performances for R407C using herringbone heat transfer tube, Int. Refrig. Air Conditioning Conf. (1998) 343–348.

[23] M. Goto, N. Inoue, N. Ishiwatari, Condensation and evaporation heat transfer of R410A inside internally grooved horizontal tubes, Int. J. Refrig. 24 (2001) 628– 638.

[24] A. Miyara, K. Nonaka, M. Taniguchi, Condensation heat transfer and flow pattern inside a herringbone-type micro-fin tube, Int. J. Refrig. 23 (2000) 141– 152.

[25] A. Miyara, Y. Otsubo, S. Ohtsuka, Effects of fin shape on condensation in herringbone microfin tubes, Int. J. Refrig. 26 (2003) 417–424.

[26] S. Wellsandt, L. Vamling, Evaporation of R407C and R410A in a horizontal herringbone microfin tube: heat transfer and pressure drop, Int. J. Refrig. 28 (2005) 901–911.

[27] E.P. Bandarra Filho, J.M. Saiz Jabardo, Convective boiling performance of refrigerant R-134a in herringbone and microfin copper tubes, Int. J. Refrig. 29 (2006) 81–91.

[28] J.A. Olivier, L. Liebenberg, J.R. Thome, Heat transfer, pressure drop, and flow pattern recognition during condensation inside smooth, helical micro-fin, and herringbone tubes, Int. J. Refrig. 30 (2007) 609–623.

[29] S. Wellsandt, L. Vamling, Prediction method for flow boiling heat transfer in a herringbone microfin tube, Int. J. Refrig. 28 (2005) 912–920.

[30] S. Guo, Z. Wu, W. Li, D. Kukulka, B. Sundén, X. Zhou, J. Wei, T. Simon, Condensation and evaporation heat transfer characteristics in horizontal smooth, herringbone and enhanced surface EHT tubes, International Journal of Heat and Mass Transfer 85 (2015) 281–291.

[31] B. Ren, inventor; Arconic Inc., assignee. Multi-layer aluminum alloy sheet product for tubes for heat exchangers. United States Patent US 9964364 B2. Mar 08 2018.

[32] E. Bardal, Corrosion and protection, Springer-Verlag London Limited, UK, (2004) 282-291.

[33] T. Morin et al., Modern Methods of High Frequency Welding Used to Produce Consistent Quality, Thermatool Corp., East Haven, CT, USA (2010).

[34] T. Okabe, Y. Iizuka, S. Igi, High Reliability Technology of the Weld Zone of High-Frequency Electric Resistance Welding Linepipes, JFE technical report No. 20 Mar 2015.

[35] J.I. Asperheim, B. Grande, L. Markegård, J.E. Buser, P. Lombard, Temperature distribution in the cross-section of the weld Vee, Tube International, Nov. 1998.

[36] H. Haga, K. Aoki, T. Sato, Welding Phenomena and Welding Mechanisms in High Frequency Electric Resistance Welding—1st Report, Welding journal (July 1980) 211-s.

[37] W. L. Hosch, Encyclopaedia Britannica, 8th ed., s.v. “Lorentz Force” (2020).

[38] W. R. Phillips I. S. Grant. Electromagnetism, 2nd Edition. Wileyc (1990).

[39] V.V. Mitin, D.I. Sementsov, An introduction to applied electromagnetics and optics, Taylor Francis, a CRC title, part of the Taylor Francis imprint, a member of the Taylor & Francis Group, the academic division of T & F Informa, plc (2017).

DTU Mechanical Engineering
Section of Materials and Surface Engineering
Technical University of Denmark

Produktionstorvet, Bld. 425
DK-2800 Kgs. Lyngby
Denmark
Phone (+45) 4525 2205
Fax (+45) 4525 1961

www.mek.dtu.dk

April 2020

ISBN: 978-87-7475-595-1